Dissertation

submitted to the

Combined Faculties of the Natural Science and Mathematics

of the Ruperto-Carola-University of Heidelberg. Germany

for the degree of

Doctor of Natural Sciences

Put forward by

Boyke Rochau

born in: Bremen

Oral examination: May 10th, 2011

Young massive star clusters as probes for stellar evolution, cluster dynamics and long term survival

Referees:

Prof. Dr. Thomas Henning

Prof. Dr. Ralf Klessen

Abstract

In this dissertation I present an astrometric and photometric study of three young and massive star clusters in the Milky Way to describe their structure, dynamics and kinematics. I conduct the first astrometric study of a Galactic starburst cluster with *HST*-WFPC2. I derived an age of 1 Myr of NGC 3603 Young Cluster and a distance of 6.75 kpc. The velocity dispersion is found to be 4.75 ± 0.8 km/s with similar velocities at different masses hint at a non-virialized cluster. Comparison of the dynamical and photometric mass suggests a high star formation efficiency and dynamical timescales show that the cluster dissolves into the Galactic field in a few Gyr. VLT-MAD observations of Trumpler14 reveal a homogeneous AO corrected PSF over the $2'$ field-of-view. The photometric analysis proves the recency of the major star forming event in the cluster about 1 Myr ago. Its mass function turns over at $\sim 0.5\,M_\odot$, consistent with a Kroupa-IMF and shows a not segregated among the intermediate mass stars. Near-infrared observations of RSGC 1 display an elongated cluster with an age of 10 ± 1 Myr located at the tip of the Galactic bar at a distance of 6 kpc. A core radius of 1.3 ± 0.4 pc is found and a blue to red supergiant ratio of 2.6 ± 0.4 is derived, providing key information for massive post-main sequence evolution. In each cluster a flat mass functions are found, displaying an overabundance of more massive stars in the cores of such massive star clusters.

Zusammenfassung

In dieser Arbeit präsentiere ich eine astrometrische und photometrische Studie von drei jungen und massereichen Sternhaufen in der Milchstrasse um ihre Struktur, Dynamik und Kinematik beschreiben. Ich führe die erste astrometrische Studie eines Galaktischen Starbursthaufens mit Hilfe von *HST* WFPC2 durch. Ich leite ein Alter von 1 Myr für NGC 3603 Young Cluster und eine Entfernung von 6.75 kpc ab. Die Geschwindigkeitsdispersion liegt bei 4.75 ± 0.8 km/s und vergleichbare Geschwindigkeiten bei unterschiedlichen Massen weisen auf einen nicht virialisierten Sternhaufen hin. Der Vergleich von dynamischer und photometrischer Masse deutet auf eine hohe Sternentstehungseffizienz hin und auf dynamische Zeitskalen zeigen, daßsich der Sternhaufen nach wenigen Gyr in das Galaktische Feld auflöst. VLT-MAD Beobachtungen von trumpler 14 zeigen eine homogene AO korrigierte PSF über das $2'$ Gesichtsfeld. Die photometrische Analyse von Trumpler 14 belegt, dass das grösste Sternentstehungereignis des Sternhaufens vor 1 Myr stattfand. Die Massenfunktion fällt bei $\sim 0.5\,M_\odot$ ab, konsistent mit der Kroupa-IMF und zeigt einen nicht massensegregierten Sternhaufen bei Sternen von bis zu $3\,M_\odot$. Nahinfrarotbeobachtungen von RSGC 1 zeigen

einen elongierten Sternhaufen mit einem Alter von 10 ± 1 Myr der an der Spitze des Galaktischen Balken bei einer Distanz von 6 kpc liegt. Ich messe einen Kernradius von 1.3 ± 0.4 pc und ein Verhältnis von blauen zu roten Überriesen von 2.6 ± 0.4, welches Schlüsselinformationen für die Nach-Hauptreihenentwicklung von massereichen Sternen bietet. In jedem der drei Sternhaufen wurde eine flache Massenfunktion abgeleitet die eine erhöhte Anzahle von massereicheren Sternen in den Kerngebieten der Sternhaufen darstellt.

Contents

List of Figures

Chapter 1

Introduction

Stellar clusters are hosts of numerous stars in different evolutionary stages. Variable in size, mass age and underlying stellar population, they offer ideal environments to study stellar and dynamical evolution. Observations of giant HII regions in extragalactic systems with intense star formation activity suggest further that clustered star formation is the dominant mode of star formation in the Universe. In the present Milky Way most stars form in dense stellar clusters since 90% of all stars that are formed can be found in stellar agglomerations (Lada & Lada, 2003).

The mass distribution of newly formed clusters in spiral galaxies – the initial cluster mass function – can be approximated by a Schechter function (Larsen, 2009). In consequence, high mass or starburst clusters (M$>10^4$M$_\odot$) are exceptional cases. Starburst clusters, representing one of the most extreme star formation environments, constitute unique astrophysical laboratories. They host stars from the upper mass cut-off in the mass function down to the hydrogen burning limit (and possibly beyond), and are present in a homogeneous environment with the same metallicity and age. In the Milky Way only about a dozen young (<30 Myr) and massive clusters ($\sim 10^4$ M$_\odot - 10^5$M$_\odot$) are known today (Figure 1.1). They are located at distances of several kpc, in contrast to smaller young open clusters, of which the census beyond 1 kpc is highly incomplete (Larsen, 2009). Milky Way starburst clusters can be found in different environments. The $\sim$2 Myr old Arches cluster and the 3-6 Myr old Quintuplet cluster (Figer et al., 1999) are located near the Galactic Center. The 1 Myr old NGC 3603 Young Cluster (e.g., Stolte et al., 2004; Rochau et al., 2010) and the 3-5 Myr clusters Westerlund 1 (Brandner et al., 2008) and 2 (Ascenso et al., 2007a) are located in spiral arms at a distance of 4 to 8 kpc from the Galactic Center (Figure 1.1). The recently detected cluster of red supergiants are located at the tip of the Galactic bar (e.g., Figer et al., 2006; Davies et al., 2007)

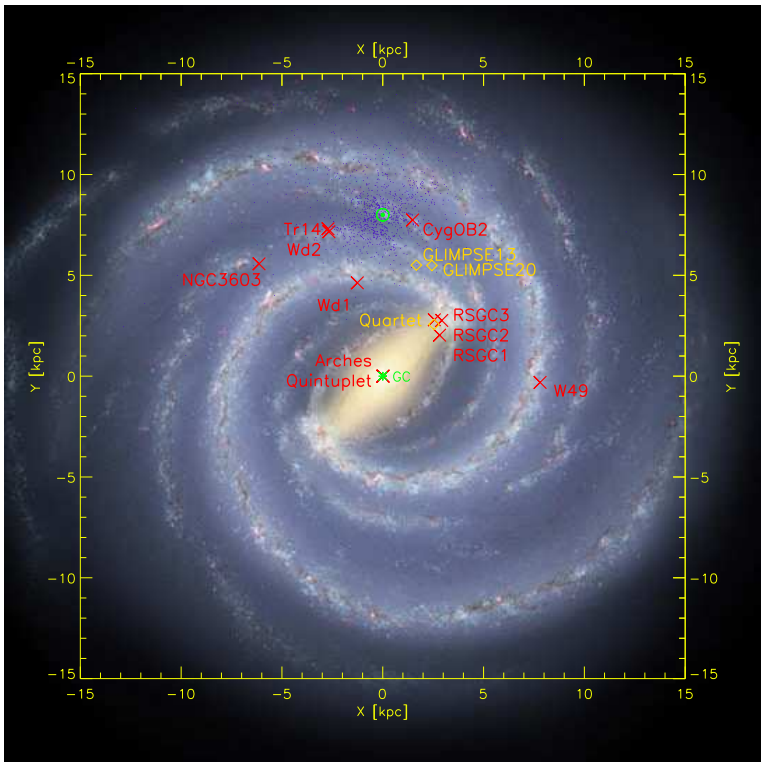

Figure 1.1: A map of the Milky Way as it would appear seen face-on (image credit: NASA/JPL-Caltech/R. Hurt (SSC)). The Galactic Center is at (0/0) surrounded by the Galactic bar. The Sun is located at (0/8) and shown as the green solar sign. Optically detected clusters from Dias et al. (2002) are shown as purple dots around the sun. Red crosses and orange diamonds are showing the Galactic population of young and massive star clusters (positions taken from Messineo et al., 2009).

While the Miky Way only houses few starburst clusters, there are considerable advantages on studying these local, and hence spatially resolved massive young clusters:

i) Starburst clusters in distant galaxies are barely resolved, restricting us to study the integrated properties of up to several 100,000 of stars. Galactic starburst clusters can be spatially resolved into 1,000s to 10,000s of stars, and the properties of each star can be derived individually. The large number of stars is crucial for a statistically sound determination of the mass function and dynamical properties of the clusters.

ii) Compared to less extreme star formation environments, starburst clusters initially house the most massive and luminous O-type main sequence stars. UV photons from these massive stars lead to rapid photo-evaporation of any remnant circumstellar material around the low-mass members of the cluster. This in turn has two advantages. First, there is very little differential extinction and IR excess, which results in a well constrained color-magnitude sequence for the cluster members. Secondly, the absence of circumstellar material means that non-accreting pre-main sequence tracks can be

used to compare theory with observations. As, e.g., shown by Siess et al. (1997) or Zinnecker & Yorke (2007) the presence of on-going accretion alters pre-main sequence evolutionary tracks quite drastically.

Details of the formation of stars, and the formation and evolution of clusters as well as their contribution to the field population, or the prospects for long-term survival as globular clusters remain uncertain. It is further undecided if low-mass stars form at the same rate in a starburst environment (and hence follow a Kroupa-type initial mass function - see Kroupa, 2002) as in more moderate star forming regions such as the well studied Orion complex. Theory suggests that gravitational collapse (Krumholz et al., 2005) or the competitive accretion of molecular material (Bonnell & Bate, 2006) shapes the initial mass function (IMF) at the high-mass end. The preferred accretion onto massive stars in dense clusters and their intense UV radiation after ignition of the O-type stars may quench or truncate the formation of low-mass objects in a starburst environment.

Simulations also indicate that in general a star formation efficiency (SFE) of at least 30% is required for a stellar cluster to remain bound after the gas expulsion phase (e.g., Hills, 1980; Lada et al., 1984; Geyer & Burkert, 2001). Under special circumstances even a SFE as low as 30% might suffice for clusters to survive for 100 Myr (Adams, 2000; Baumgardt & Kroupa, 2007). Because of the rapid expulsion of any remaining gas, as well as high mass loss rates of the most massive cluster members, young clusters are not in virial equilibirium. Furthermore, the loss of graviational potential due to gas expulsion and stellar evolution is answered by an expansion of the cluster. Figure 1.2 depicts a NIR gallery of Milky Way starburst and red supergiant clusters arranged by age and plotted to the same physical scale. The age sequence corresponds also to a sequence of increasing half-mass radius (0.5 pc for NGC 3603 YC and Arches, 1 pc for Westerlund 1, and $\sim$2 pc for RSGC 1). While the increasing half-mass radius with increasing cluster age is suggestive of dynamical evolution, a quantitative analysis of the cluster masses and internal dynamics is required.

The luminosity function (LF) of a stellar system indicates the number of stars in different magnitude intervals occupying a certain volume or surface. The LF provides information about the efficiency of star formation and is altered by stellar as well as dynamical evolution (Binney & Merrifield, 1998). More massive stars are evolving faster and early O-type stars show first signatures of stellar evolution after only a few Myr. Therefore, the bright end of the LF is mostly affected by stellar evolution. Dynamical evolution alters the appearance of the LF due to dynamical interaction via two-body encounters. Energy is exchanged redistributed among the stellar population until equipartition of the kinetic energies is achieved. Stars populating the high velocity tail of the Maxwellian velocity distribution might exceed the escape velocity of

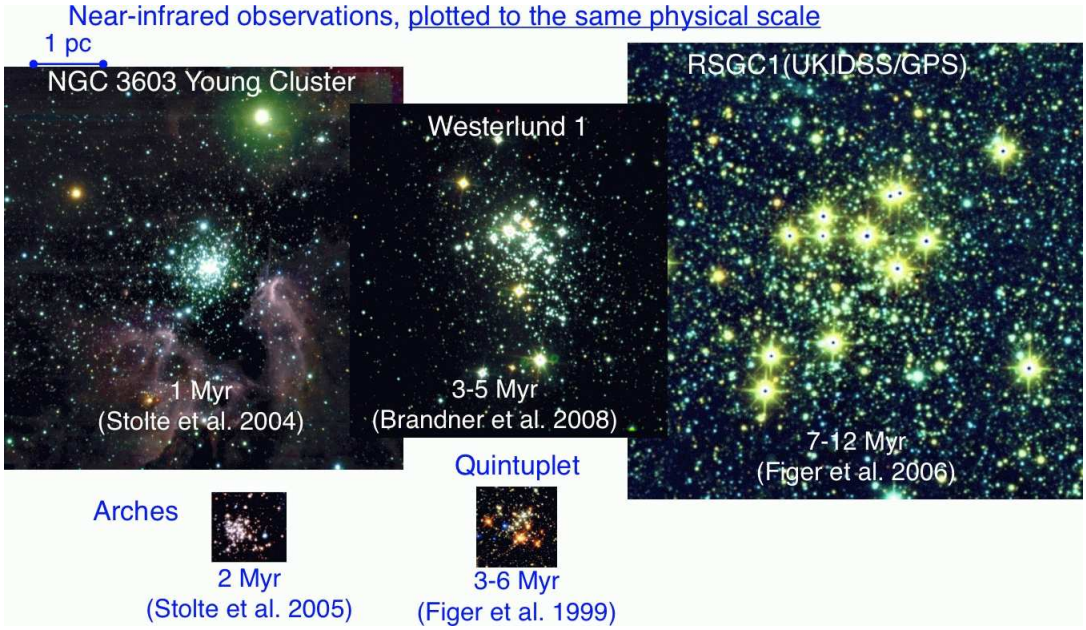

Figure 1.2: Known Galactic starbursts plotted to the same physical scale. From left to right with increasing age. The upper images show the spiral arm starburst cluster NGC 3603 YC, Westerlund 1 and RSGC 1. The two lower clusters, Arches and Quintuplet, are located close to the Galactic center. Images are near-infrared composites taken from Brandner et al. (2008); Figer et al. (1999, 2006); Stolte et al. (2004, 2005).

the cluster and are lost to the Galactic field. Such evaporation strips out stars and subsequently flattens the LF.

In general LF is a tool to test stellar evolutionary models (e.g. Cassisi & Salaris (1997)). Studies with it HST offer the opportunity for accurate measurements of the LF and mass function (MF) of a stellar population down to the hydrogen burning limit (e.g. King et al. (2005)). Zinnecker & McCaughrean (1991) have shown that K-band LFs can be used as age estimators for young stellar clusters.They derived theoretical LFs from a Miller-Scalo IMF. They identified a peak in the LF which evolves with time. They related this peak to Deuterium burning which occurs on very short timescales. Thus, it can only be applied to very young stellar populations.

The mass luminosity relation (MLR) connects the mass of a star with its the absolute luminosity. The MLR is required to transform an observed LF into a MF. If dN is the number of stars that are formed in the mass interval m to $m+dm$ and the corresponding magnitude interval M_X to $M_X + dM_X$, they can be related by

$$dN = -\psi dM_X = \xi dm, \tag{1.1}$$

where $\xi(m)$ is the present-day mass function (PDMF) and $\psi(M_X)$ if the present-day

luminosity function (Kroupa, 2001). They are related through

$$\psi(M_X) = -\xi(m)\frac{dm}{dM_X} \tag{1.2}$$

and dm/dM_X is the MLR, It provides an important tool for the estimation of stellar masses. We will use the MLRs that are provided by the stellar evlutionary models.

Extensive studies have been conducted concerning the stellar mass function (MF, e.g., Salpeter, 1955; Scalo, 1986; Kroupa, 2001). The MF gives the distribution of stars in a certain mass range. Consequently it reflects the efficiency of the formation of stars with different masses. The initial mass function (IMF) represents the distribution of stellar masses for a given stellar system at the time of its formation. The form of the MF changes with time due to stellar, as well as dynamical evolution. As a result of such effects, the MF is altered in entire stellar star clusters (Baumgardt & Makino, 2003) and, thus, the 'actual' MF is not reflecting the initial state and should better be called present-day mass function (PDMF). In general, the IMF can be described as a power law (Scalo, 1986):

$$\xi(\log \mathrm{m}) \propto m^{\Gamma} \tag{1.3}$$

The index Γ is the power-law slope:

$$\Gamma = \frac{d\log \xi(\log \mathrm{m})}{d\log \mathrm{m}}. \tag{1.4}$$

Salpeter (1955) found a value for the slope of the IMF in the solar neighborhood, often taken as a reference, of $\Gamma = -1.35$, since it is still valid for the supersolar MF. In the same manner with the IMF we describe the slope of the PDMF as

$$\gamma = \frac{d\log N(\log \mathrm{m})}{d\log \mathrm{m}}\ , \tag{1.5}$$

where $N(\log \mathrm{m})$ is the PDMF. This slope is given by the linear relation between the logarithmic mass intervals and the corresponding number of stars (in logarithmic scale).

In 1955 Edwin Salpeter published the first estimate of the IMF (Salpeter, 1955) for stars in the solar neighborhood with masses between $0.4M_{\odot}$ and $10M_{\odot}$ and found that it can be described with a single power-law (Salpeter, 1955). Since then, origin and shape of the IMF was the topic of several investigations (e.g., Scalo, 1986; Kroupa, 2001). The proposed power-law distribution implies that the IMF has to flatten approaching lower masses or to show a cut-off to avoid a diverging mass density at $m \to 0$. For a known IMF of a stellar system the PDMF can be derived considering its stellar and dynamical evolution. The PDMF includes a mixture of the stellar and dynamical evolution of the system, as well as, of the initial conditions at the epoch of its formation. The

high mass end of the PDMF is affected by mass loss due to stellar evolution, while evaporation of stars flattens the low mass end. However, such evolution happen on different timescales, hence. The PDMF of a cluster can be used to reveal dynamical effects such as mass segregation. Mass segregation refers to a situation in which the high mass stars are centrally concentrated and the MF steepens outwards (de Grijs et al., 2002). Therefore, the examination of the radial dependence of the MF may exhibit a potential mass segregation.

Kroupa (2002) notes that theoretical dynamical examination of massive and long-lived globular clusters ($N \gtrsim 10^5$ stars) reveals that the global PDMF is similar to the PDMF at distances near the half-mass radius. The PDMF inward and outward the half-mass radius becomes flatter and steeper respectively due to dynamical mass segregation. Dynamical evolution of a cluster also flattens the global PDMF since evaporation is stronger for stars with lower masses than for high-mass ones (Vesperini & Heggie, 1997).

Chapter 2

NGC 3603 Young Cluster

2.1 Introduction

Massive young stellar clusters are outstanding objects containing copious numbers of stars over the entire stellar mass range. With masses between $10^4\,M_\odot$ and $10^7\,M_\odot$ (Zhang & Fall, 1999; de Grijs et al., 2003; Mengel et al., 2008), they cover the upper end of the cluster mass function and may constitute progenitors of globular clusters (GCs; Zhang & Fall, 1999; McCrady & Graham, 2007). While extragalactic starburst clusters, such as those in the Antennae Galaxies, are often barely resolved (Whitmore & Schweizer, 1995), in Milky Way starburst clusters thousands of individual stars can be observed.

In addition to three clusters in the Galactic Center region (Arches, Quintuplet, Young Nuclear Cluster), only a handful of Milky Way starburst clusters located in spiral arms have so far been identified (e.g., Brandner et al., 2008). Among the spiral arm clusters, the NGC 3603 Young Cluster (NYC), located in its namesake giant HII region NGC 3603 (Kennicutt, 1984), is the most compact and youngest cluster with an age of $\approx$ 1Myr (Brandl et al., 1999; Stolte et al., 2004; Sung & Bessell, 2004) and a central mass density $\rho_0 \geq 6 \cdot 10^4 M_\odot \mathrm{pc}^{-3}$ (Harayama et al., 2008). It hosts three Wolf–Rayet stars, at least 6 O2/O3, and 30 late O-type stars (Moffat et al., 2004), and is extensively referenced as a template for extragalactic starburst environments (e.g., Lamers et al., 2006).

Previously, dynamical studies of Galactic starburst clusters were largely restricted to one-dimensional velocity dispersions derived from radial velocity measurements of a few of the most luminous cluster members (e.g., Mengel & Tacconi-Garman, 2007). Using multi-epoch observations of GCs, King & Anderson (2001, 2002) and Anderson & King (2003a) pioneered high precision proper motion studies with the *Hubble Space*

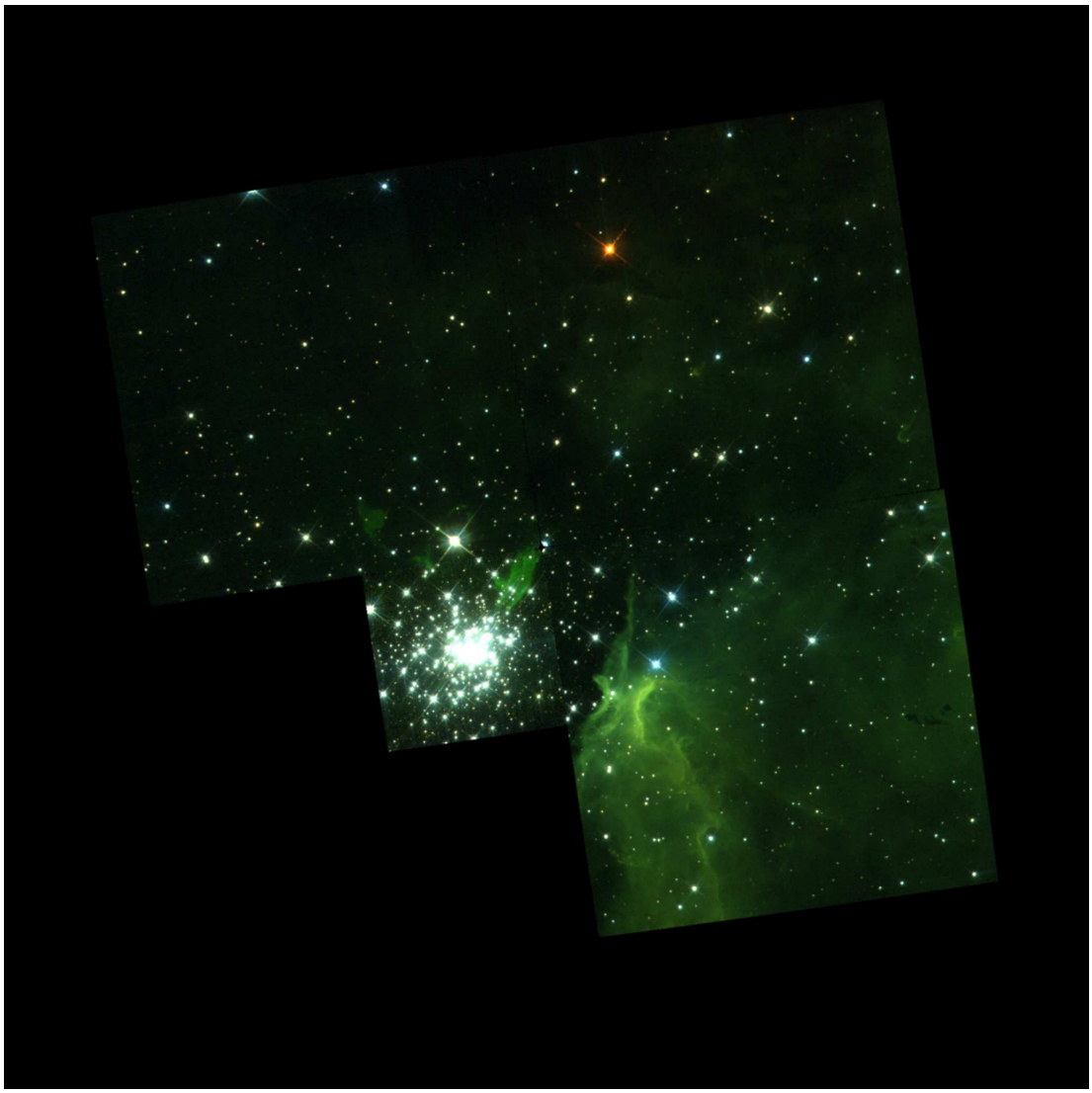

Figure 2.1: VRI color composite of the young cluster in NGC 3603. North is up and east is to the left. The stairstep image is due to the different pixel scales of PC1 and the three WFCs. The core of NYC is located on the PC1 chip in the southeast right below the blue supergiant Sher 25 with its associated bipolar outflow and polar ring.

Telescope (HST), which enabled the distinction of GC members from field stars, and the study of GC dynamics and kinematics.

In 2006, we initiated an extensive observational program to obtain multi-epoch high-angular resolution imaging observations of Galactic starburst clusters with the aim to study their internal dynamics and global motions. In the following, we present the results of our analysis of two epochs of *HST* observations of NYC separated by 10.15 yr. Accurate proper motions enable us to get a 'clean' census of the cluster population by rejecting field stars and to study the internal cluster dynamics.

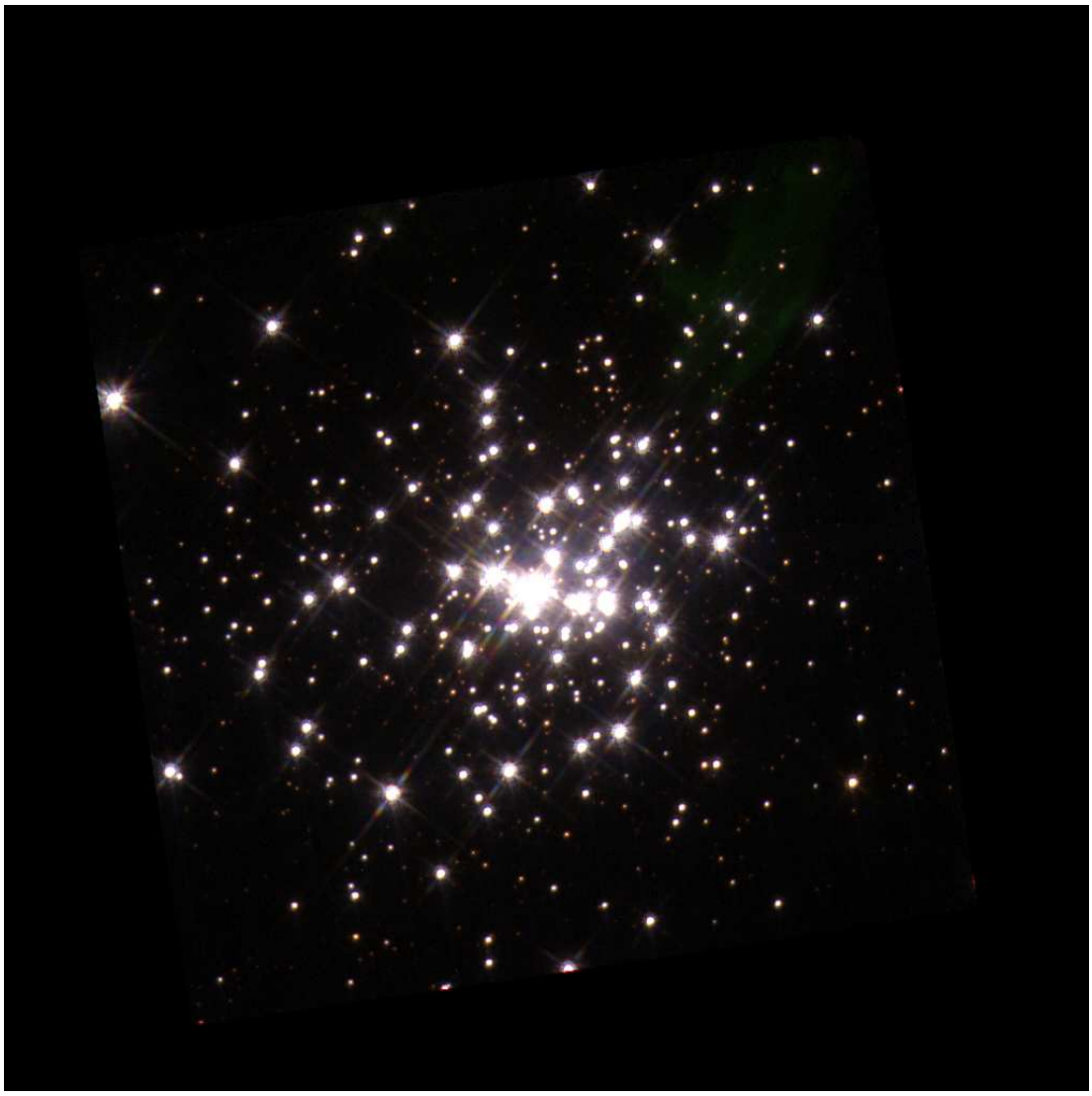

Figure 2.2: VI composite of the core of the young cluster in NGC 3603. The image is composed of the PC1 observations on which the following analysis is based. In the center we observe the concentration of the bright O- and WR stars.

Table 2.1: Details of the observations

Date	Filter	$t_{\rm exp}$(s)	$t_{\rm tot}$(s)	Stars
30/07/97	F547M	3×1,12×10,8×30	363	772
31/07/97	F814W	3×0.4,12×5,8×20	221	1163
26/09/07	F555W	4×0.4,4×26,4×100	506	1048
26/09/07	F814W	4×18,4×160	712	2014

2.2 Observations and data analysis

Two epochs of observations of NYC with the *HST*/Wide-Field Planetary Camera 2 (WFPC2) separated by 10.15 yr are analyzed in this chapter. A VRI color composite from the first epoch data is presented in Figure 2.1. WFPC2 was installed in December 1993 onboard *HST* as a successor to the similar WF/PC. The reduction from eight to four cameras inhibits to switch between Wide Field (f/13; WFC) and Planetary Camera (f/28; PC1). The four cameras, each with 800×800 pixels, provide three WF channels with an angular resolution of $0.996''$/pixel and the PC1 as the high resolution channel with a pixel scale of $0.045''$/pixel. The different pixel scales of the four channels lead to the unique geometry of the complete WFPC2 images (Figure 2.1).

We compare PC1 observations in F547M and F814W from epoch 1 (GO 6763, archival data) with our second epoch observations in F555W and F814W (GO 11193). The central region of NYC is shown as a VI color composite of the PC1 observations of the first epoch. With an image scale of 45.5 mas pixel^{-1}, PC1 provides the best point-spread function (PSF) sampling of the WFPC2 cameras. While the first epoch observations were carried out in stare mode, for the second epoch we selected a four-point sub-pixel dither pattern to facilitate bad pixel recovery and to provide an improved PSF sampling. Table 2.1 summarizes the observations, including individual and total exposure times.

Data reduction has been performed with IRAF/Pyraf. We combined the individual bias subtracted, flat-fielded images with identical exposure times using `multidrizzle` (Koekemoer et al., 2002). This corrects for velocity aberration and geometrical distortion including the 34th column anomaly based on the latest distortion correction[1][2] (see Section 2.2.2). Furthermore, for the second epoch we applied a 2×2 oversampling during the drizzling process improving the sampling of the PSF. Combining images of identical exposure times assure that the correction for the charge transfer efficiency (CTE) problem can be adressed accordingly. Since this connection depends on the

[1] http://www.stsci.edu/hst/wfpc2/analysis/calfiles
[2] http://ftp.stsci.edu/cdbs/uref/sad1946fu_idc.fits

position on the detector as well as on the exposure times, a combination of images with different exposure times would, therefore, hamper a proper correction.

Astrometry and photometry were derived from the drizzled images for each filter and exposure time setting using DAOPHOT (Stetson, 1990) with a Penny2 PSF varying linearly across the field. Simulations based on TinyTim PSFs (Krist, 1995) indicate that the positional PSF fitting uncertainty results in a centroiding error of $\sigma_{\mathrm{PSF}} = 0.013 \pm 0.001$ pixel.

Near the faint end of our photometry, where the photometric errors begin to dominate, the star list was filled in by the results derived from the next longer exposure, and uncertainties assessed accordingly. The final number of detections in each band and epoch for a 5σ threshold above the background noise is listed in Table 2.1.

2.2.1 CTE correction

Charge Transfer Efficiency

The WFPC2 CCDs have been shown to suffer from loss of charge during the readout; this CTE problem arises when the collected charges are transferred across the chip resulting in a loss of signal (e.g., Holtzman et al., 1995). This effect increases with decreasing source flux, meaning that the fractional loss of charge is larger for faint sources. In the case of high signal-to-noise sources it is significantly reduced. In addition, higher background levels reduce the observed effect as the CTE loss depends on the number of charges (Whitmore et al., 1999).

The detector is read out in the y-direction meaning charges being located at the top of the detector have to 'travel' larger distances during the readout and are, therefore, more strongly affected by the CTE problem. Hence, the effect is position-dependent. An example for the effect of the CTE problem is displayed in Figure 2.3, showing a cutout of the short (0.4s) F555W-image from our data set. The image shows the upper right corner of the PC1 chip, which is most affected and displays obvious trails in the y-direction as a sign of lost charge during the readout process.

As described, the CTE induces a loss of signal along a specific direction of the detector. Assuming an initially symmetric PSF of a star on the detector, the loss of charges along the y-axis will break the symmetry of the PSF and shift the centroid. Since we measure stellar positions from the PSF after reading out the detector, the CTE effect is not only changing the measured stellar magnitude but, furthermore affects the astrometry that is obtained from the image. In order to account for the CTE problem a photometric and astrometric solution has to be derived.

Figure 2.3: Cutout from of the 0.4s F555W-band image to display the effect of the CTE problem. Stripes along the y-axis demonstrate the loss of charge during the readout.The displayed area is selected from a region on the detector with large y-coordinates to highlight the effect.

Photometric correction

A consequence of the CTE problem is a reduced number of detected charges compared to the number of charges that is related to the infalling number of photons. The measured brightness is, therefore, underestimated if the CTE loss is not considered. Several studies concerning this problem have been carried out (e.g., Whitmore et al., 1999; Holtzman et al., 1995; Dolphin, 2000) and provide solutions for applying corrections to the photometry.

During our analysis we follow the most recent recipe that is provided by A. Dolphin[3] to estimate the photometric corrections that have to be applied. The correction in x-direction is as follows:

$$XCTE(mag) = 0.0077 \times exp(-0.5bg) \times (1 + 0.1yr) \times x/800, \qquad (2.1)$$

where bg is an estimate of the local background and yr describes the time of the observations, since the CTE loss worsens with detector age. Finally, x is the x-coordinate on the detector. The correction in x-direction depends only on the background and the time of observation, but not on the source brightness which is the reason for the lower

[3]http://purcell.as.arizona.edu/wfpc2_calib/

effect. The correction for the y-direction is more complex and estimated via

$$YCTE(mag) = 2.41 \times ln(exp(0.02239 \times c1 \times y/800) \times (1 + c2) - c2). \quad (2.2)$$

where the parameter *c1* depends on the observed local background, on the signal related to the source and $XCTE(mag)$ of the corresponding source. Parameter *c2* accounts for the aging effect of the detector and the counts detected from the source. Finally, y is the y-coordinate of the star.

Astrometric correction

In contrast to the photometry, correcting the astrometry is not straightforward. As mentioned, the effect of the CTE is a loss of charges predominantly in the y-direction. This creates assymetries in the PSF and, subsequently, a shift of the centroid. Kozhurina-Platais et al. (2007) presented an analysis of *HST* observations obtained with the Advanced Camera for Surveys (ACS) to assess the astrometric uncertainty induced by CTE centroid shifts. They utilized the decreasing fractional loss of charges with increasing brightness and compared long and short observations of the same field obtained with ACS. Astrometry from the short exposures, detecting fewer photons and, thus, suffering from a larger centroid shift, are compared to the astrometry that is obtained from the long exposures. This allows one to reduce the induced centroid shifts down to the level of the long exposures.

We apply the same approach here, using the long exposures as a reference for the astrometry. The y-offsets of the positions of both short and long exposure time are plotted in Figure 2.4 as a function of magnitude and y-coordinate (we considered only the y-coordinate since the effect of the CTE in significantly larger due to the readout direction). To quantify the shift in the y-coordinate, we followed Equation 7 of Kozhurina-Platais et al. (2007):

$$DeltaY = b_1 + b_2 \times mag + b_3 \times Y \quad (2.3)$$

with b_1, b_2 and b_3 as free parameters.

Red crosses in Figure 2.4 are displaying the measured offsets between the long and short F814W exposures in epoch 2. The scatter of the bright stars is due to non-linearity and saturation in the long exposures. Astrometric uncertainties at the faint end arise from low signal-to-noise ratios in the short exposures. These stars have been excluded during the fitting procedure. We fitted a plane to the remaining offset distribution. The best fitting plane for the F814W-band is overplotted to the offsets and shown as a green grid in Figure 2.4. The different parameter values for b_1, b_2 and b_3 are summarized in

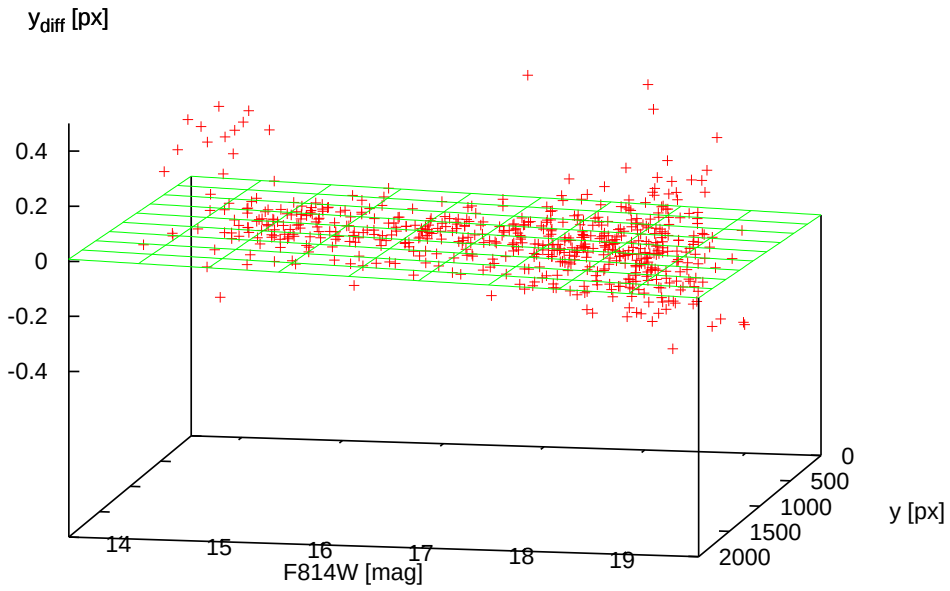

Figure 2.4: 3D plot of the dependence of the y-offset as a function of magnitude and y-coordinate. The measured offsets between the long and short F814W exposures in epoch 2 are shown as red crosses. The observed large scatter is due to saturation (bright end) in the long exposures and photometric uncertainties in the short exposures (faint end). Both groups of stars have been excluded during the fitting procedure. The resulting best fit to the observed surface is overplotted as the green grid.

Table 2.2 (note the different pixel scale due to 2×2 oversampling for the second epoch). The resulting parameters have been used to derive the y-offset which was subsequently used to correct the y-coordinate.

2.2.2 Geometric distortion, 34th row anomaly and velocity aberration

The combined contribution of the different measurement uncertainties, the PSF fitting accuracy $\sigma_{\rm PSF}$, the geometric distortion $\sigma_{\rm geo}$, the pixel phase error $\sigma_{\rm pxph}$ and *HST*-breathing $\sigma_{\rm breath}$ amounts to total uncertainty of

$$\sigma_{\rm err} = \sqrt{\sigma^2_{\rm geo} + \sigma^2_{\rm pxph} + \sigma^2_{\rm PSF} + \sigma^2_{\rm breath}} = 1.21 \pm 0.18\,{\rm mas}. \qquad (2.4)$$

Table 2.2: Parameters of the astrometric correction

Epoch	b_1(px)	b_2(px mag^{-1})	b_3
1997.58	0.094	-0.0056	6.17×10^{-5}
2007.73	0.122	-0.011	3.31×10^{-5}

The observed proper motion dispersion has to be corrected for $\sigma_{\rm err}$ to derive the intrinsic proper motion dispersion of the cluster members and, subsequently, the velocity dispersion of the cluster stars. In the following text we describe each contribution to the error budget in detail.

Geometric distortion

Observations carried out with WFPC2 suffer from geometrical distortions caused by the design of the instrument and distortions are enhanced by the spherical aberration, i.e. the pyramid that is responsible for splitting the FoV into four areas is placed in the aberrated beam; the position of an object can be shifted up to 5 pixels at the edges of each of the four chips (Anderson & King, 2003b). To address the induced distortion a 'distortion solution' must be obtained by observing the same field in numerous orientations and offsets (Anderson & King, 2003b). The huge amount of data that is available leads to the derivation of a solution showing that the geometric distortions of WFPC2 are currently reduceble down to a level of ± 0.02 pixel for the PC1 frame and to ± 0.01 pixel in case of the WFC frames (Anderson & King, 2003b). The most recent corrections[4][5] have been used together with `multidrizzle` to account for the geometric distortions.

The combined image of the PC1 frame has distortions reduced to a level of 0.02 pixel (see Anderson & King, 2003b). Due to the different orientation angle of 51° between the two epochs, we have to consider the uncertainty of the position induced by the residual geometric distortion, $\sigma_{\rm geo} = 0.017 \pm 0.001$ pixel.

34th row anomaly

The four chips (PC1, 3×WFC) of WFPC2 suffered an error during manufacturing. In each chip, each 34th row (each 1024/30=34.1333 rows, Shaklan et al., 1995; Anderson & King, 1999) was built $\sim 3\%$ narrower compared to the other rows. The newest distortion file, in combination with `multidrizzle`, includes, besides the correction for geometric distortions and velocity aberration, also a correction for the 34th row anomaly.

[4] http://www.stsci.edu/*HST*/wfpc2/analysis/calfiles
[5] http://ftp.stsci.edu/cdbs/uref/sad1946fu_idc.fits

Velocity aberration

HST as a space observatory has an orbital speed of $\sim 7\,\mathrm{km/s}$ around the Earth which itself orbits the Sun with a velocity of $\sim 30\,\mathrm{km/s}$. Such velocities together with the change of the angles between the telescope motion relative to the Sun and the direction of the star in barycentric coordinates and its instantaneous apparent direction can cause plate scale changes (Cox & Gilliland, 2002). Such velocity aberration is of the order of 10^{-4} and is measured during the observations and corrected by the most recent version of `multidrizzle`.

2.2.3 Pixel phase error

According to Anderson & King (2000), the pixel phase describes the position of a star in a pixel compared to the boundaries of the pixel ($\phi_x \equiv -\mathrm{int}(\mathrm{x} + 0.5)$ Anderson & King, 2000). Figure 2.5 (taken from Anderson & King, 2000) displays the result of their measurements of 15 dithered images and plots the residuals of measured x positions as a function of the pixel phase. The detector was divided into nine regions with each of the regions showing comparable behaviour. Differences in the position measurement of one star as a function of the pixel phase exhibit a sinusoidal variation of the amplitude and similar rms dispersions. For such sinusoidal pixel phase errors (Figure 2.5), the second epoch dithering pattern with 0.5 pixel shifts largely cancels out the pixel phase error. The first epoch observations, in contrast, were observed in stare mode, thus, the pixel phase error has to be considered. With a typical amplitude of the sinusoidal pixel phase error of ± 0.02 pixel, the uncertainty to be included in our analysis amounts to an average residual uncertainty of $\sigma_{\mathrm{pxph}} = 0.013 \pm 0.003\,\mathrm{pixel}$

2.2.4 Breathing

During one orbit of *HST* the telescope is subject to temperature variations. It warms up and cools down during its orbital 'day' and orbital 'night' respectively. Changing temperatures cause small focus variations known as '*HST* breathing'. The subsequent variation of the pixel scale smears out the PSF when combining images of (slightly) different pixel scales and introduces an additional uncertainty in the position measurement.

To quantify the effect of breathing, we selected a handful of wide pairs of bright stars. These pairs share either similar x-position and a large distance concerning the y-coordinate or similar y-coordinates associated with large x offsets. Larger pair offsets facilitates the analysis of this effect. Position measurements of the selected stars have

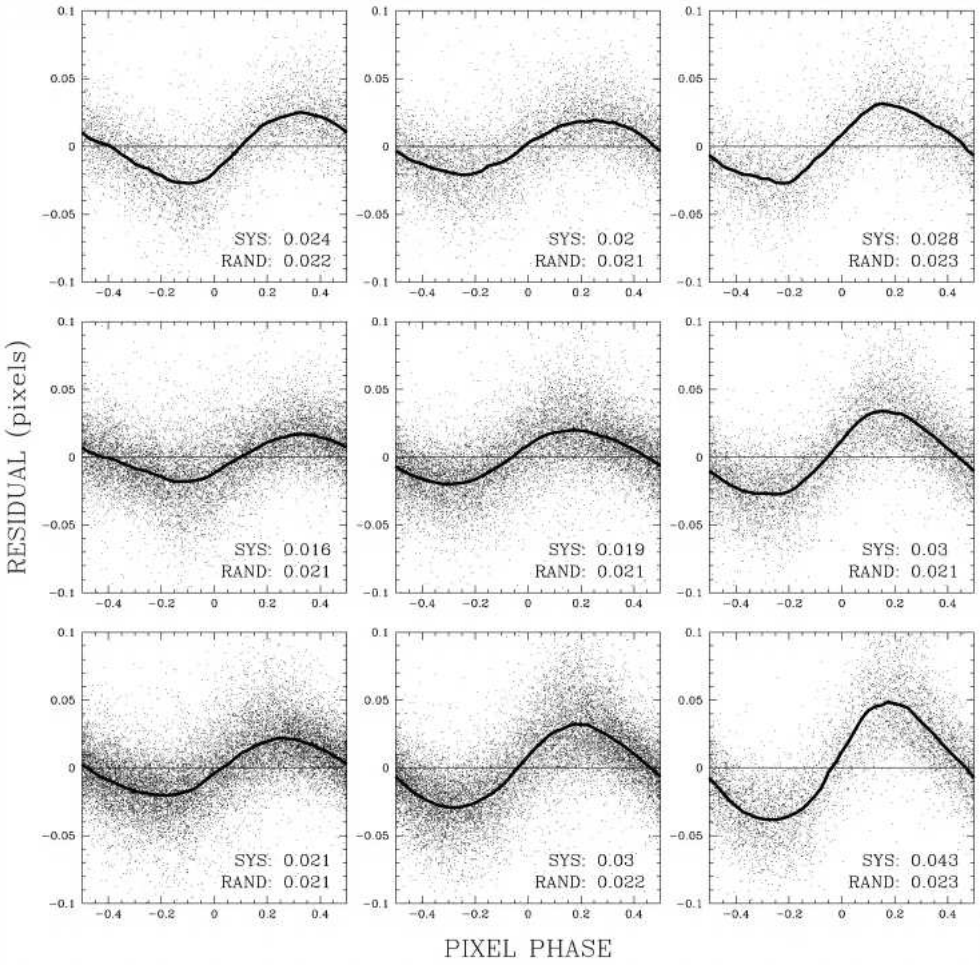

Figure 2.5: Pixel phase error in position measurements of 15 dithered images in chip WF2. The SYS and RAND values give the amplitude and rms dispersion of the offset distribution (from Anderson & King, 2000).

been obtained from unprocessed images taken during different phases of *HST*'s orbit. They cover the maximum possible fraction of an orbit within our observations and, hence, the largest temperature differences. Measured distance variations normalized to their total separation allow us to quantify the scale changes. Relating this to the mean distance of our stellar sample to the center of the detector, which is least affected by scale changes, results in a general uncertainty in our measurements of $\sigma_{\mathrm{breath}} = 0.009 \pm 0.002$.

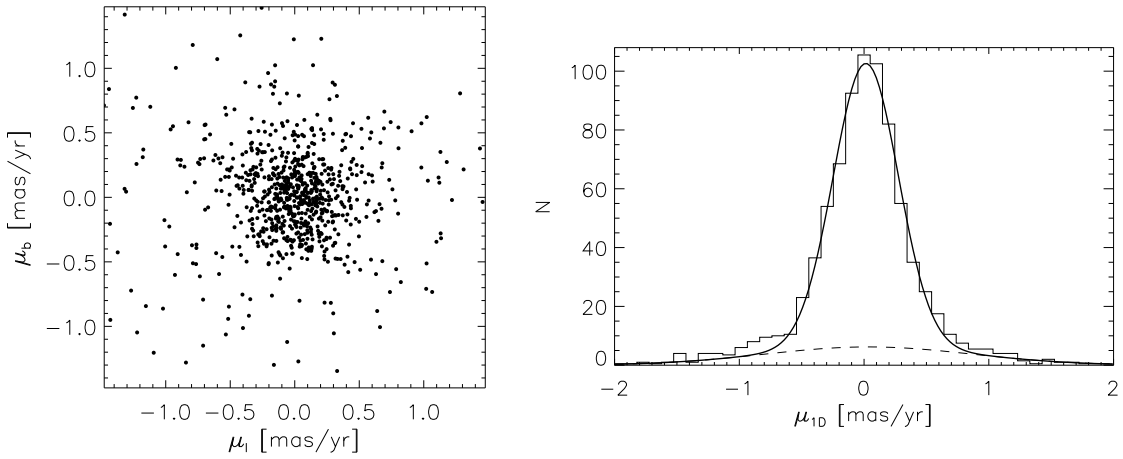

Figure 2.6: *Left panel:* Proper motions of stars in the NYC reference frame in Galactic coordinates. *Right panel:* Histogram of the averaged one-dimensional proper motions of all stars, fitted by a two-component Gaussian (thick line), while the dashed line represents the distribution of the field stars.

2.3 Proper motions and membership

As the orientation angles of the two epochs differ ($\Delta\Theta = 51°$), the common field available to our analysis is a circle with a diameter of $30''$. A geometric transformation based on a preliminary list of bright cluster members is derived using IRAF/GEOMAP with a second-order polynomial. Stars detected in F814W band with photometric PSF fitting uncertainties $\sigma_{\rm phot} < 0.1$ mag are matched after applying this transformation, and individual proper motions are calculated for each star. The final proper motion table contains 829 matched stars.

In Figure 2.6 we show the measured proper motions for all stars with respect to the cluster reference frame in Galactic coordinates. In this reference frame, cluster members center around (0,0) in the proper motion diagram. The symmetrical distribution of all proper motions around (0,0) indicates the absence of any large relative motion of the cluster with respect to the field, i.e., the cluster follows the Galactic rotation curve. As NYC's Galactic longitude of l=291.6° implies an almost tangential view into the Carina spiral arm, the distributions of cluster member and field star proper motions are superimposed (see Figures 1.1 and 2.7). Figure 2.7 displays the difficulty in the discrimination of cluster from field stars introduced by the locations of NYC and the Sun. The right panel shows the proper motion of the field population in Galactic longitude over the timebaseline of 10.1 yrs, the separation of our two epochs of WFPC2 obseravation. The cluster is located close to a minimum of the proper motions of the Galactic field and, thus, field stars located in the proximity of NYC are exhibiting similar proper motions.

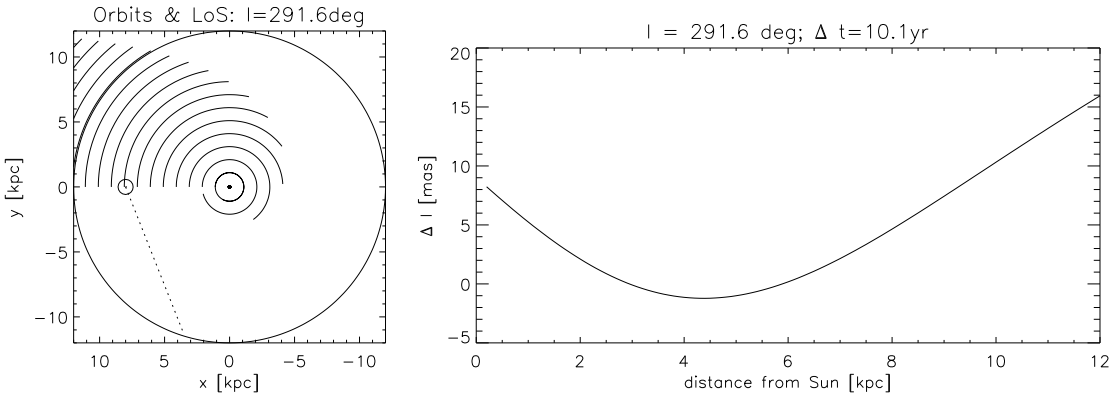

Figure 2.7: *Left panel:* A view onto the Galactic disc, the x- and y-axis display the distance to the Galactic center which is centered at (0/0). Fraction of concentric circles corresponding to an epoch span of 50 Myr. The location of the Sun can be found at (8/0) and NYC is located at a distance of 6.75 kpc along the dotted line. *Right panel:* Change of Galactic longitude l over 10.1 years as a function of distance from the sun. The estimated distance of NYC at 6 kpc is close to the bottom point and, thus, stars of the Galactic field exhibit similar proper motions.

The proper motion distribution in Figure 2.6 is fitted by a two-component Gaussian with the wide function describing predominantly foreground stars, and hence non-cluster members (dashed line in the right panel of Figure 2.6), and the narrow component is interpreted as cluster member candidates. The fit delivers the proper motion dispersion σ_μ for the cluster and Σ_μ for the field (following the nomenclature of Jones & Walker, 1988).

To calculate cluster membership probabilities $P_{\rm mem}$ we followed the procedure described in Jones & Walker (1988). We derive the normalized distribution of proper motions of the cluster stars and of the field stars which follows

$$\Phi_c = \frac{1}{(2\pi\sigma_\mu^2)} \times exp\left(-\frac{1}{2}\left((\frac{\mu_l-\mu_{l,c}}{\sigma_\mu})^2+(\frac{\mu_b-\mu_{b,c}}{\sigma_\mu})^2\right)\right) \tag{2.5}$$

for the cluster stars and

$$\Phi_f = \frac{1}{(2\pi\Sigma_\mu^2)} \times exp\left(-\frac{1}{2}\left((\frac{\mu_l-\mu_{l,f}}{\Sigma_\mu})^2+(\frac{\mu_b-\mu_{b,f}}{\Sigma_\mu})^2\right)\right) \tag{2.6}$$

for the field population. Hereby, μ_l and μ_b are the measured proper motion of each star in Galactic coordinates and $\mu_{b,c}$ and $\mu_{b,f}$ are the mean cluster and field proper motion, respectively. The probability for a star to belong to the cluster population is finally calculated via

$$P_{\rm mem} = \frac{\frac{\rho}{f}\Phi_c}{\Phi_f + \frac{\rho}{f}\Phi_c} \tag{2.7}$$

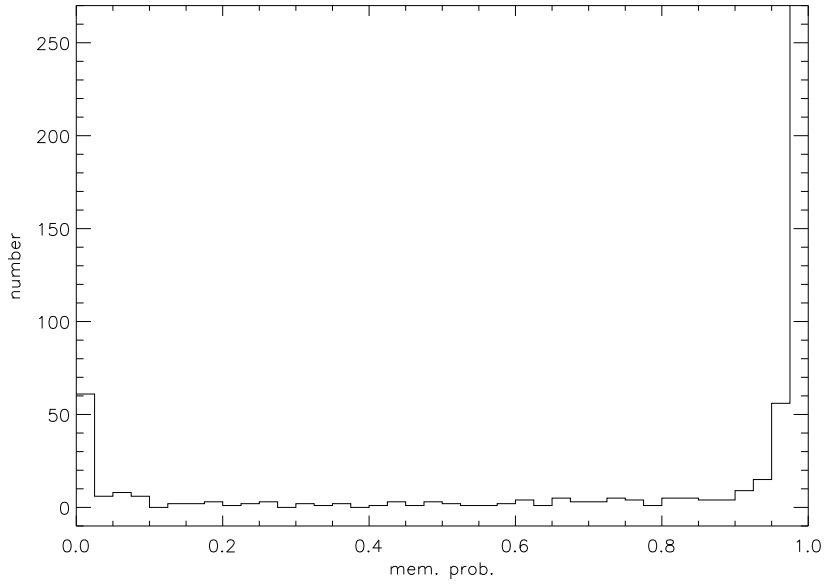

Figure 2.8: Membership probability distribution for the several hundreds of stars. We observe a division of the distribution into stars with very high and very low membership probabilities. Stars with a with a probability of $> 90\%$ are considered cluster members.

where ρ and f describe the density of stars of the cluster and of the field (estimated assuming that field star proper motion deviates by more than 2σ from the mean of the proper motion distribution in the right panel of Figure 2.6). The calculated propabilities are ascribed to each star and the resulting membership propability distribution is shown in Figure 2.8. It is divided into two groups of stars with either very low probabilities ($P_{\rm mem} < 0.1$) and a larger group of stars with $P_{\rm mem} > 0.9$. We consider stars as cluster members if $P_{\rm mem} > 0.9$. This significantly reduces the number of contaminating field stars, but due to the similar proper motions of cluster and field, some field stars might remain in the cluster sample. Based on Besançon models (Robin et al., 2003), we estimate the number of field stars in our FoV to be 46 stars between $16\,{\rm mag} < {\rm m}_{555} < 25\,{\rm mag}$. Including stars with a membership probability above 0.9 in our cluster sample, we subtracted a total of 58 stars as field stars with the same magnitude constraints. For the variable stars *HST* 12, 474, 481, and 574, studied by Moffat et al. (2004), we found membership probabilities $P_{\rm mem}$ of 0.75, 0.98, 0.90, and 0.98, respectively, indicating that the latter three are likely cluster members.

2.3.1 Besançon models

The Besançon modelling of the Galactic stellar population (Robin et al., 2003) allows us to compare our results with population synthesis models. The Besançon model

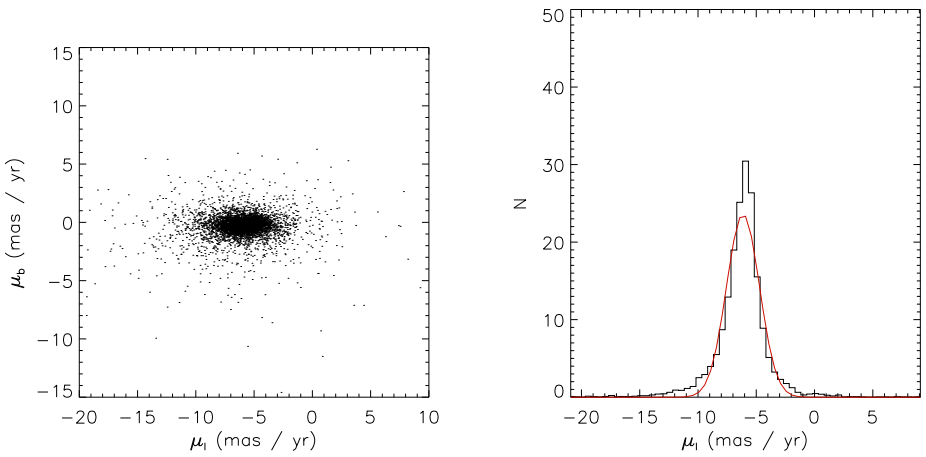

Figure 2.9: Proper motion diagrams of a catalogue that is based on the Besaçon model. Diagrams are comparable to the Figure 2.6

provides photometric, astrometric and spectroscopic information of Galactic field stars. The model of the Galaxy is composed of four components: The thin disc, the thick disc, the stellar halo, and the bulge. These components differ in age distribution, metallicity, radial metallicity gradient, IMF, and star formation rate. A detailed description of the synthesis model is given in Robin et al. (2003).

Based on this model for the stellar population and rotation for the Galaxy, we obtained a photometric catalogue that includes photometric and kinematic information. The kinematic information has been used to create a diagram similar to Figure 2.6. It is shown in Figures 2.9 and includes modeled stars in an area of $5' \times 5'$ around the Galactic coordinates $l = 291.6°$, $b = -0.6°$, the coordinates of NGC 3603 and for distances between 0 and 20 kpc. The obtained catalogue contains ∼8,400 entries in total, which is reduced to almost 6,000 sources by excluding sources that fall outside our 16 mag $<$ V $<$ 25 mag and 1 mag $<$ V$-$I $<$ 4 mag criteria. We identify an ellipsoidal distribution in Figure 2.9, the proper motion diagram of the modeled field stars in the left panel, which is centered at $\sim (-6/0)$. The proper motion distribution along the Galactic longitude is shown in the right panel of Figure 2.9. Regarding the shape of the distribution, we see that it resembles the one we have derived for NYC. In order to identify the centre of the distribution, we fit a Gaussian function to the observed distribution. Giving a best-fit peak located at -6.14 ± 1 mas/yr. From the absence of any relative motion of NYC reveals that it moves with comparable proper motion to that of the Galactic disc population.

2.4 Extinction, distance and age

Based on our photometric catalogue, we created a color magnitude diagram (CMD) of NYC; the m_{555}, $m_{555} - m_{814}$ CMD is shown in Figure 2.10. The distinction between candidate cluster members (small dots) and field stars (open circles) as described in Section 2.3 leads to a very well defined cluster sequence with high-mass main sequence (MS) stars, intermediate-mass stars located in the PMS–MS transition region between $m_{555} = 18$ mag and 20 mag, and more than 300 lower mass PMS stars down to $m_{555} = 24.5$ mag (Figure 2.10, middle). The efficiency of the proper motion member selection is evident in the left panel of Figure 2.10, particularly among PMS and faint stars that could not be distinguished from cluster members from their colors alone. The foreground sequence blueward of the PMS does likely not belong to the cluster, suggesting a residual contamination of 18 stars with 20 mag$< m_{555} <$ 24 mag.

In the following, we assume solar metallicity (Melena et al., 2008) for the cluster and the relation between absolute and selective extinction from Schlegel et al. (1998). The upper MS is well fitted by a 1 Myr Padova isochrone (Marigo et al., 2008, black solid line along the MS in the right panel of Figure 2.10) for $A_{\rm V}$=4.7 mag and a distance modulus of 14.1 mag. For the analysis of the PMS–MS transition region and the lower mass PMS we use Siess models (Siess et al., 2000), computed as in Da Rio et al. (2009), as well as PISA-FRANEC models (Degl'Innocenti et al., 2008, , PF09), transformed into the observational plane using ATLAS 9 model atmospheres (Castelli & Kurucz, 2003). The best-fitting isochrones yield a distance between 6.6 kpc (PF09) and 6.9 kpc (Siess) and a visual extinction $A_{\rm V}$=4.7 mag (PF09) and 4.6 mag (Siess), respectively for an age of 1 Myr. We note that the derived selective extinction is in good agreement with $E({\rm B-V}) = 1.25$ mag as reported by Sung & Bessell (2004), though the absolute extinction value derived by us is slightly higher due to the use of the Schlegel et al.-relations. The 1 Myr PF09 isochrone represents the PMS best, in particular at the PMS–MS transition region.

At an age of 1 Myr, stars with masses between 3.5 and 3.8 $M_\odot$ are expected to be in the short-lived radiative–convective (r–c) gap phase (Mayne et al., 2007). This phase corresponds to the formation of a radiative core in the interior of the stars, due to the increasing central temperature (Iben, 1965). We observe eight sources in the r–c gap at 18.5 mag$< m_{555} <$ 19 mag (Figure 2.10) and $m_{555} - m_{814} \sim 2.25$ mag (shown as diamonds in the right panel of Figure 2.10). If their PMS nature is spectroscopically confirmed, this is the first identification of PMS stars in this interesting evolutionary stage.

A previously unreported CMD feature is the apparent extension of the MS toward

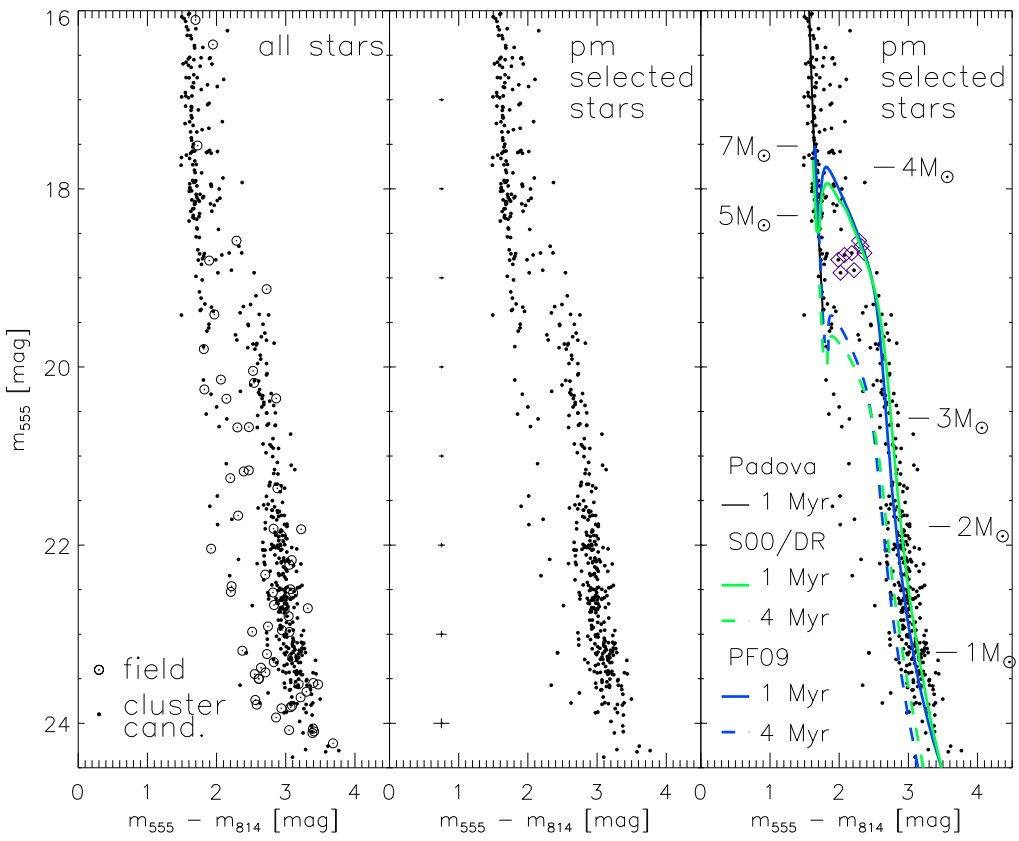

Figure 2.10: *Left:* $m_{555} - m_{814}$ vs. m_{555} CMD of cluster (small dots) and field stars (open circles). Clearly visible are the MS and PMS loci at $m_{555} - m_{814}$ ∼1.5 and 3 mag, respectively. *Center:* cluster member candidates with $P_{\rm mem} > 0.9$. Apparent is the narrow PMS after the proper motion selection. *Right:* cluster member candidates with the best-fitting Padova 1 Myr (MS, black solid line) and PF09 1 Myr as well as Siess 1 Myr (PMS, dark and light gray solid lines, respectively) isochrones overplotted. Diamonds mark the stars in the r–c gap. The extension of the MS below the transition region is not covered by the younger isochrones, but is reproduced by a 4 Myr isochrone (PF09, dark gray dashed line; Siess track, light gray dashed line).

lower masses below the PMS–MS transition region ($m_{555} \gtrsim 18.5$ mag). Isochrone fitting to the MS turn-on yields an age of 4 Myr. The derived age is consistent with recent estimates of the age of the two blue supergiants Sher 23 and Sher 25 (Melena et al., 2008). These stars might represent an earlier epoch of star formation in the giant H II region (see also Sung & Bessell, 2004).

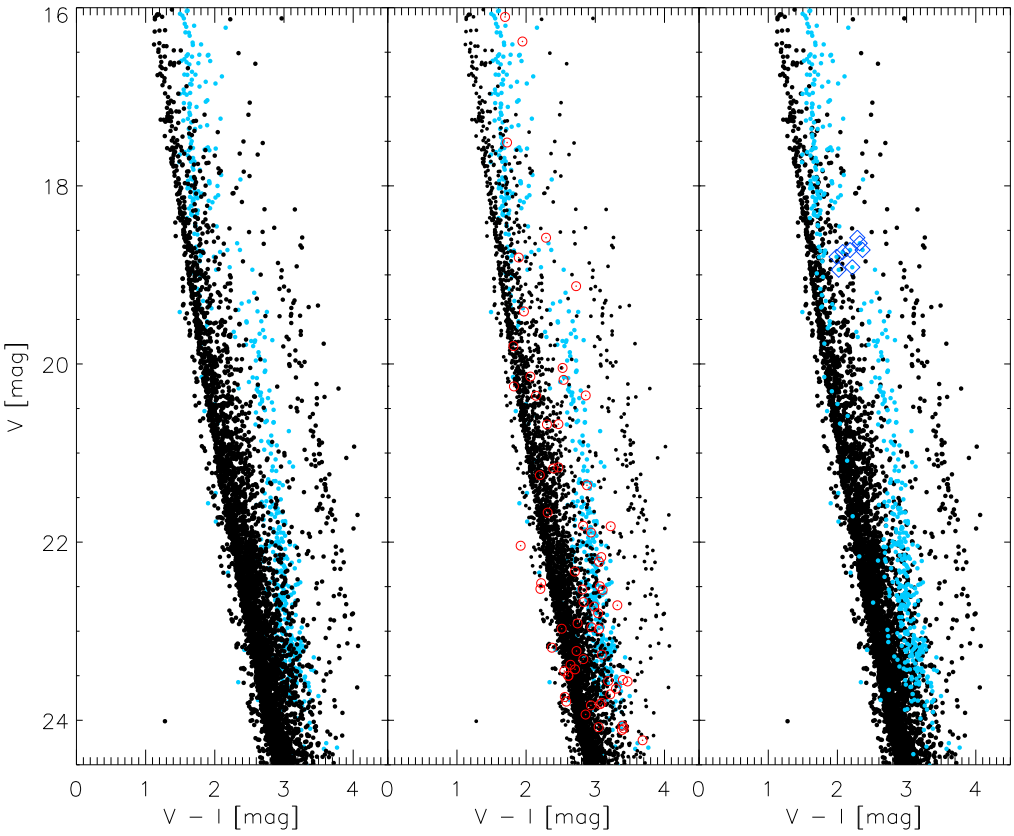

Figure 2.11: V vs. V-I CMD of the cluster and the data obtained from the Besançon models. The modelled stars are shown as black dots and cover an area of ~ 10 times the size of the PC1 frame. Cluster member candidates from our observations are shown as blue dots and identified field stars are shown as red circles. *Left panel:* The stars from the Besançon models are superimposed to the cluster members. *Middle panel:* Same as the left panel but with the field stars overplotted as red circles. *Right panel:* Cluster stars are superimposed to the modelled field sequence. The stars in the r-c gap are highlighted as diamonds. Comparison shows that the majority of the identified field stars follow the main sequence as obtained from model of the Galaxy and supports the goodness of our proper motion selection.

2.5 Velocity dispersion and cluster dynamics

2.5.1 Velocity dispersion

The distribution σ_{obs1D} of the proper motions $\mu_{\mathrm{obs1D}} = \frac{\mu_l + \mu_b}{2}$, as shown in the right panel of Figure 2.6, is a combination of internal proper motion dispersion and instrumental effects, resulting in $\sigma_{\mathrm{obs1D}} = \sqrt{\sigma^2_{\mathrm{pm1D}} + \sigma^2_{\mathrm{err}}}$. Similar diagrams as in the left panel of Figure 2.6 are shown in Figure 2.12 with the stars divided into magnitude bins of 1 mag. From left to right and top to bottom you see stars from the bright to the faint end. In each diagram the stars concentrate around (0/0) as in Figure 2.6 with

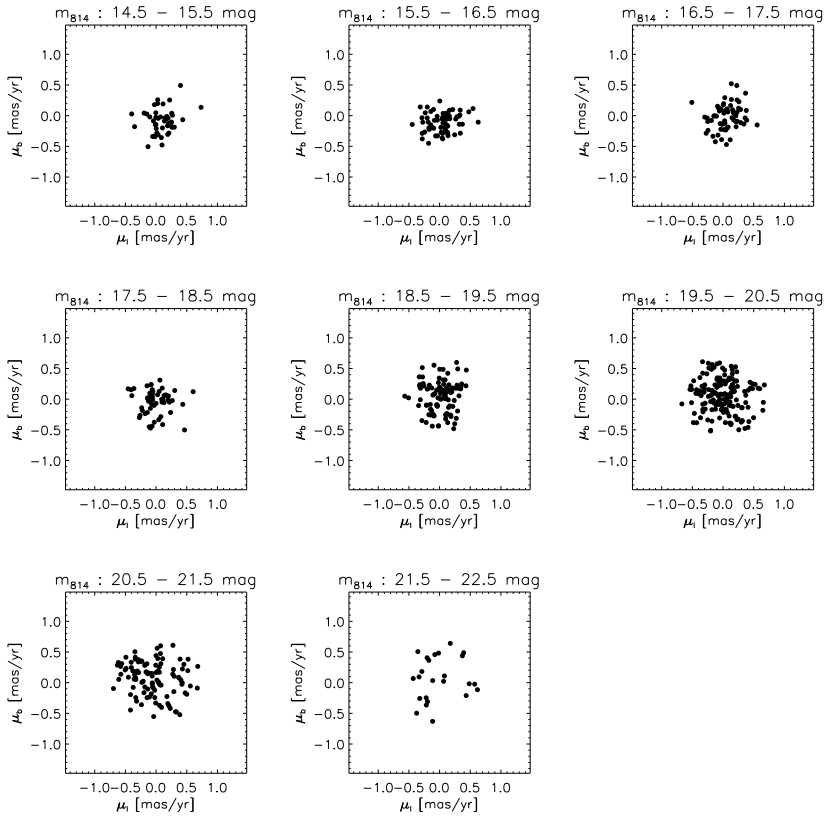

Figure 2.12: Proper motions of stars in the NYC reference frame in Galactic coordinates within magnitude bins of 1 mag in width. From top left to lower right the stars are counted in bins from $m_{814} = 13.5$ mag to $m_{814} = 22.5$ mag in steps of 1 mag.

an increasing scatter around the origin at fainter magnitudes. Figure 2.13 displayes the one-dimensional observed proper motion dispersion as a function of stellar magnitude (binsize=1 mag) for candidate cluster members. The proper motion dispersion is constant for stars with $14.5\,\mathrm{mag} \leq m_{\mathrm{F814W}} \leq 18.5\,\mathrm{mag}$ ($\approx$1.7–9 $M_\odot$).

Correcting the observed one-dimensional proper motion dispersion of $\sigma_{\mathrm{obs1D}} = 184 \pm 20\mu$as/yr for the instrumental effects discussed in Section 2.2 results in an intrinsic one-dimensional velocity dispersion $\sigma_{\mathrm{pm1D}} = 141 \pm 27\mu\mathrm{as\ yr}^{-1}$ for stars brighter than $m_{814} \approx 18.5$ mag, assuming a negligible effect of binary orbital motions (Girard et al., 1989). This corresponds to $\sigma_{\mathrm{cl1D}} = 4.5 \pm 0.8\,\mathrm{km\ s}^{-1}$ at a distance of 6.75 kpc. The constant velocity dispersion for stars in the mass range 1.7–9 $M_\odot$ indicates a lack of equipartition of energy among cluster members. This provides a strong indication that NYC is far from virial equilibrium. Nevertheless, an upper limit of the cluster mass can be obtained by deriving the virial mass M_{dyn} from the observed velocity dispersion (Spitzer, 1987):

$$M_{\mathrm{dyn}} = \eta \frac{r_{\mathrm{h}}\ \sigma^2_{\mathrm{cl3D}}}{G} \tag{2.8}$$

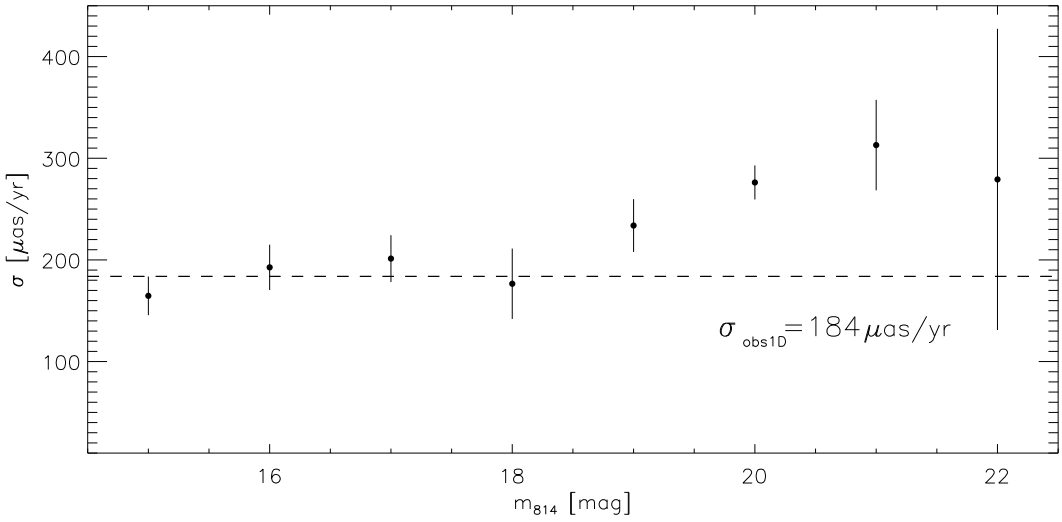

Figure 2.13: The observed proper motion dispersion as a function of stellar magnitude of the cluster member candidates. For 14.5 mag $<$ m$_{814}$ $<$ 18.5 mag, we obtain a standard deviation $\sigma_{\rm obs1D}$ = 184μas/yr with an uncertainty of 20μas/yr (dashed line).

where $\eta \approx 2.5$ (weakly depending on cluster density structure), $r_{\rm h}$ is the half-mass radius, $\sigma_{\rm cl3D}$ is the three-dimensional velocity dispersion, and G is the gravitational constant.

NYC is mass segregated with its core radius increasing with decreasing stellar mass (Nürnberger & Petr-Gotzens, 2002). A lower limit on $r_{\rm h}$ for the high-mass stars as derived from *HST* data is comparable to the core radius of ≈0.2 pc (Stolte, 2003), whereas Harayama et al. (2008) based on the analysis of near-infrared adaptive optics data estimate $r_{\rm h}$ = 0.7–1.5 pc for stars in the mass range 0.5–2.5 M$_\odot$. If we assume $r_{\rm h}$ = 0.5 pc and a three-dimensional velocity dispersion of $\sigma_{\rm cl3D} = \sqrt{3} \times 4.5 \pm 0.8$ km s^{-1}, we derive $M_{\rm dyn} = 17600 \pm 3800\,{\rm M}_\odot$.

Considering that this dynamical mass estimate provides an upper limit, it is in agreement with photometric studies of NYC, which assigned masses to individual stars, and estimated the total stellar mass to $M_{cl} \approx 10000 - 16000\,{\rm M}_\odot$ (Stolte et al., 2006; Harayama et al., 2008).

As derived in Section 2.3, NYC is comoving with the Galactic field, not showing a relative motion compared to the Galactic field. Comparison with the Besançon model suggested that the cluster moves with a proper motion of $\sim -6.14 \pm 1$ mas/yr in the Galactic plane with respect to the Sun. At a distance of 6.75 kpc this correspond to transversal velocity in the Galactic plane of $v_t = 196.5 \pm 32$km/s.

2.5.2 Dynamical timescales

Through the astrometric study presented in the previous section we have derived the velocity dispersion, leading to an estimate of the dynamical mass of NYC using a half-mass radius of 0.5 pc. Such information will be used in the following section to derive dynamical timescales for this cluster.

Dynamical time

The dynamical timescale describes the time that the cluster requires to establish virial equilibrium. With the known mass of the cluster and a characteristic radius (e.g., the half-mass radius r_{hm}) the dynamical time can be calculated via

$$t_{dyn} = \sqrt{\frac{GM}{r_{hm}^3}}, \tag{2.9}$$

where G is the gravitational constant. Using a $r_{hm} = 0.5\,\mathrm{pc}$ and the dynamical mass of $17,600\,\mathrm{M}_\odot$ yields $t_{dyn} = 0.05\,\mathrm{Myr}$.

Relaxation time

The time needed for a stellar system to achieve thermal equilibrium is called relaxation timescale and is related to the dynamical timescale (Spitzer, 1987) through

$$t_{rh} = \frac{N}{7\ln\Lambda} t_{dyn}, \tag{2.10}$$

where N is the number of stars and Λ is $c \times N$.

In the idealized scenario where a stellar cluster is composed of stars of equal mass with a homogeneous spatial and isotropical velocity distribution, the parameter c becomes 0.4 (Spitzer, 1987). Giersz & Heggie (1994) found an empirical value of $c = 0.11$ for clusters with stars of a single mass. The value of c will be even lower for systems that include stars over a large mass range (Portegies Zwart et al., 2010). The relaxation timescale reflects the time that it takes the kinetic energy of the stars to redistribute through two-body encounters such that the velocity distribution becomes Maxwellian. Following Equation 17 of Portegies Zwart et al. (2010), the ralaxation timescale can be expressed as

$$t_{rh} \sim 2 \times 10^8\,\mathrm{year} \left(\frac{\mathrm{M}}{10^6\,\mathrm{M}_\odot}\right)^{\frac{1}{2}} \left(\frac{\mathrm{r_{hm}}}{\mathrm{pc}}\right)^{\frac{3}{2}} \left(\frac{\langle \mathrm{m} \rangle}{\mathrm{M}_\odot}\right)^{-1} \tag{2.11}$$

with $\langle m \rangle$ describing the mean stellar mass of the cluster. To derive Equation 2.11

Portegies Zwart et al. (2010) adopted a value of $\ln\Lambda = 10$. Using the derived mass of 17,600 $M_\odot$ together with the earlier adopted half-mass radius of 0.5 pc and a characteristic mass of 1 $M_\odot$ (Harayama et al., 2008), we derived a half mass relaxation time of 10 Myr.

Number of stars

We have derived the dynamical time as well as the half-mass relaxation time. With Equation 2.10 we are now able to estimate the number of stars that NYC contains using the relation $7 \times t_{rh}/t_{dyn} = \frac{N}{\ln\Lambda}$. We plot the ratio of t_{rh} and t_{dyn} against the number of stars in a stellar system with three different values for Λ in Figure 2.14. Λ-values are chosen to $\Lambda_1 = 0.11\,N$ as the empirical value for a system of equal mass stars (black line), which has been adopted in the analysis and $\Lambda_3 = 0.4\,N$ for the idealized case. $\Lambda_2 = 0.05\,N$ was computed for comparison for a cluster of stars with a certain mass distribution. We derived $t_{rh}/t_{dyn} = 176$ and, together with $\Lambda = 0.11\,N$, we derived a number of cluster members for NYC of 8415 stars.

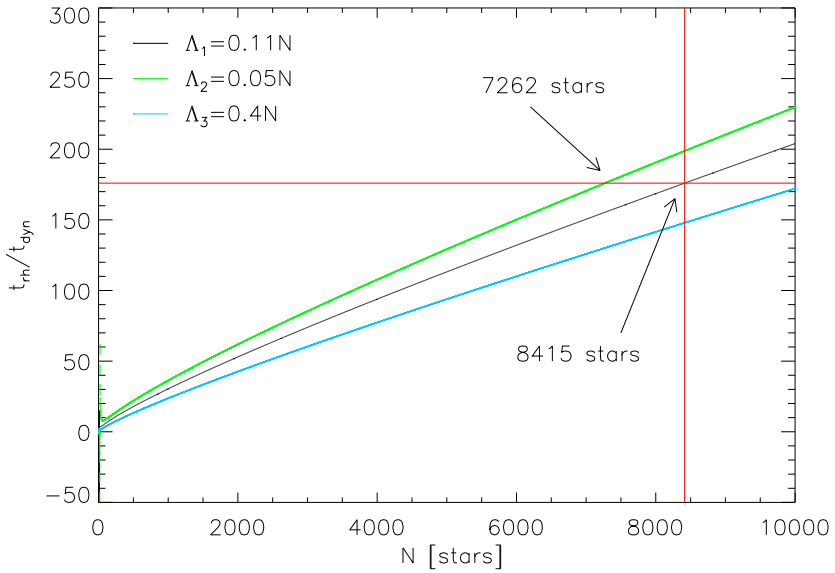

Figure 2.14: The ratio of the half-mass relaxation time to the dynamical time as a function of members of the clusters. Three values for Λ have been adopted, $\Lambda_1 = 0.11\,N$ as the empirical value for a system of equal mass stars (black line), $\Lambda_3 = 0.4\,N$ for the idealized case and $\Lambda_2 = 0.05\,N$ for a cluster of stars with a certain mass distribution. The ratio t_{rh}/t_{dyn} was derived to be 176, which is shown as the red horizontal line. The vertical red line shows the number of stars of a stellar system with $t_{rh}/t_{dyn} = 176$ and $\Lambda = 0.11\,N$.

Dissolution timescale

The velocities of stars in dynamically relaxed clusters show a Maxwellian velocity distribution. Stars in the high velocity tail might exceed the escape velocity and be stripped from the cluster. The depleted tail is refilled within a relaxation time reestablishing the Maxwellian distribution. Thus, the cluster gradually looses stars and expands subequently. The extraction of stars and expansion of the cluster eventually leads to the evaporation of the stellar population into the field. The corresponding dissolution timescale can be estimated, according to Portegies Zwart et al. (2010), by

$$t_{dis} \sim 2\,\mathrm{Myr}\left(\frac{\mathrm{N}}{\ln\Lambda}\right)^{0.75}\left(\frac{\mathrm{R_G}}{\mathrm{kpc}}\right)\left(\frac{\mathrm{V_g}}{220\mathrm{kms}^{-1}}\right)^{-1}. \tag{2.12}$$

In Equation 2.12 we assumed a circular orbit of the cluster around the Galactic center leaving a factor $(1-\epsilon)$ unadressed.

In the last section we have estimated the total number of stars in the cluster, thus we have to derive its distance to the Galactic center and its orbital velocity. To obtain the distance from the Galactic center we used the known distance between the Sun and NYC, the distance of the Sun to the Galactic center and the Galactic longitude of NYC. From simple geometry we derived a distance between the Galactic center and NYC of $R_G = 8.35\,\mathrm{kpc}$.

The Sun orbits the Galactic Center with $\Omega_0 \times R_0 = \theta_0 = 220\,\mathrm{km/s}$. With Equation 2.12 we estimated the dissolution time to be 3.4 Gyr. As seen, depending on the chosen Λ-values the number of cluster members differ with a lower number of stars if masses of stars are not equal. Furthermore, the dissolution timescale for a cluster on an elliptical orbit is lower compared to a circular orbit. Since we might have overestimated the number of cluster members and assumed a circular orbit, the dissolution timescale should be considered as an upper limit.

2.6 Mass function

Completeness

In order to obtain the correct cluster the mass function, accurate knowledge of the completeness function is required. In dense stellar fields the detectability of a source depends on its flux relative to the background noise and the local stellar density ('crowding'). Crowding describes the effect of a decreasing detection probability due to high stellar densities such that the brightness contrast between a point source and a possible bright neighbour limits individual source detectability. Together with the detection limit due to low signal-to-noise ratio of faint sources, these two effects define the completeness function. This function depends on the brightness of the source, the noise levels and its position in the observed field.

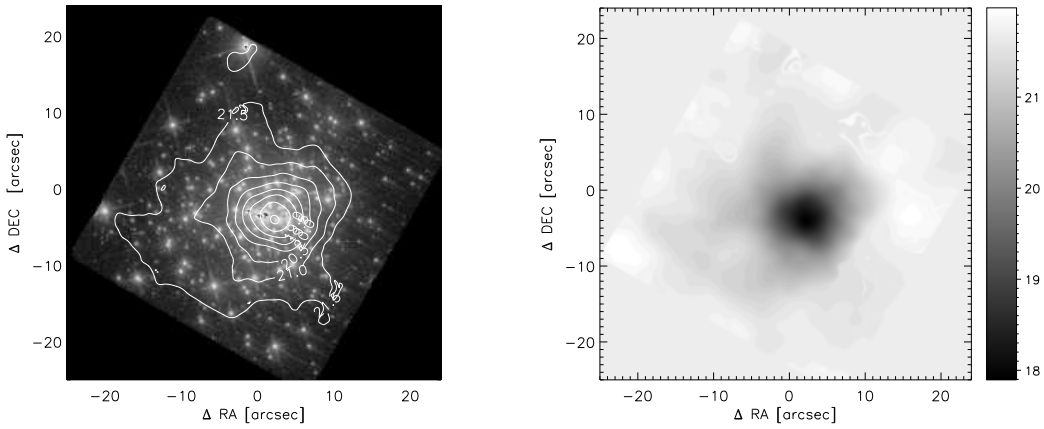

Figure 2.15: F814W-band completeness map of the short exposure of NYC. *Left Panel:* F814W-band image of NYC with 50%-completeness limits superimposed as white contours. The contour levels cover a magnitude range between 18 mag< m_{555} <22 mag (in steps of 1 mag). The image is centered (0/0) at $\alpha = 11^h15^m07.5^s, \delta = -61°15'35.8''$. *Right Panel:* F814W-band completeness map of the entire observed FoV. The grey shades correspond to the F814W-band magnitude at which a completeness of 50% is achieved. As visible, the completeness close to bright center of the cluster drops significantly due to crowing effects. Incrreasing incompleteness appears rather concentric revealing the symmetry of the cluster.

To determine the completeness function, we applied the same technique as described in Gennaro et al. (2011). We will briefly summarize the procedure here and refer to the Appendix of the paper for further details. We added 50 stars to our science image and re-processed the photometry to estimate the fraction of recoveries. 100 individual runs were processed to add a total of 5,000 stars to our image in each photometric bin of

0.5 mag width. The rather low number of artificial stars has been chosen not to change the crowding characteristics of observations. Thus, we achieved a typical separation between simulated stars of $d_{sim} \sim 29$ pixel.

The final product of our procedure for each photometric band 'j' is a funtion of position on the detector and magnitude of the star:

$$C_j(x, y, \mu) = \frac{\alpha(x, y)}{exp\frac{\mu-\beta(x,y)}{\gamma(x,y)} + 1}. \tag{2.13}$$

Here α (≤ 1) is the normalization factor, β the magnitude at which the completeness is $\alpha/2$ and γ describes how fast the completeness C_j drops to zero. With the derived values for (α, β, γ), we can assign a completeness factor to each star considering its measured magnitude and position.

The left panel of Figure 2.15 shows the F814W-band image of NYC for the central field with the 50% completeness limits at different magnitude superimposed as contours. The right panel depicts the same completeness limits over the observed field as a function of magnitude. The limiting magnitude increases significantly in the proximity of the brightest stars in the core of the cluster while further out a smooth degradation towards to lower density areas is observed. This illustrates the symmetry of the cluster with a rather radial decrease of crowding and thus incompleteness.

2.6.1 Mass luminosity relation

To derive the mass function of the core of NYC, we require knowledge of the MLR. We use the 1 Myr PMS isochrone from PF09 (Degl'Innocenti et al., 2008) to derive the relation between the stellar luminosity and present mass for the PMS stars. Masses for the stars that are in their MS phase are derived using the applied 1 Myr isochrone of Marigo et al. (2008). We have to consider the distance to NYC and the measured extinction in order to relate the present mass to the observed m_{555} magnitude and to obtain the MLR. We have measured reddening and distance modulus as derived in Section 2.4. The apparent m_{555} magnitude as a function of the present mass is shown in Figure 2.16. The MLR is used to derive the present stellar mass which is ascribed to the corresponding star.

Figure 2.16 shows an almost linear depence of the apparent magnitude for masses between 1 $M_\odot$ and 3 $M_\odot$. Above 3 $M_\odot$ the star enters the PMS-MS transition visible in the CMD in Figure 2.10 as the PMS isochrone bends towards the MS. In this phase stellar brightness increases faster with stellar mass until the star is close at the MS. Near the MS, when the star is close to equilibrium, it is getting fainter and arrives at

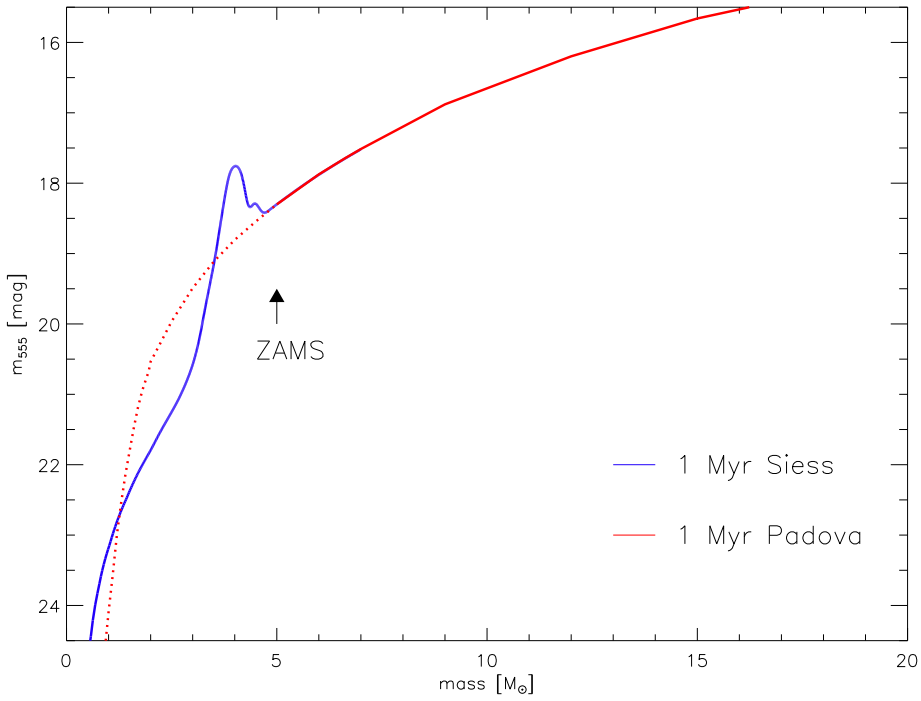

Figure 2.16: Mass luminosity relation of the applied isochrone for NYC. The MLR for the PMS is taken from the 1 Myr PMS isochrone from PF09 and shown as the blue line. For the MS we used the 1 Myr isochrone of Marigo et al. (2008) (red line). The ZAMS can be identified at masses of $\sim 5 M_{\odot}$.

the ZAMS. For a stellar system of 1 Myr, the ZAMS starts at $\sim 4.8\,M_{\odot}$.

2.6.2 Mass function of NYC

In order to obtain the PDMF of a cluster we use the derived MLR. In the case of NYC a single age model fit represents very well the majority of stars. Thus, we use the MLR taken from the 1 Myr PF09 isochrone for the PMS and the 1 Myr Padova track for the MS to ascribe the present mass to each star which belongs to our stellar sample of the cluster.

To derive the PDMF of NYC we used the method suggested by Maíz Apellániz & Úbeda (2005). They discuss the biases that are introduced by the binning process to derive the MF. Assuming a constant bin size can lead to misleading results, due to the correlation between the number of stars per bin (higher for lower masses) and the assigned weights (from the Poisson statistics). To circumvent this problem they suggested a variable bin size having an equal number of sources in each bin. They found, in this case, that the bias is almost independent on the assumed number of stars per bin, and remains low even for a single star in each bin.

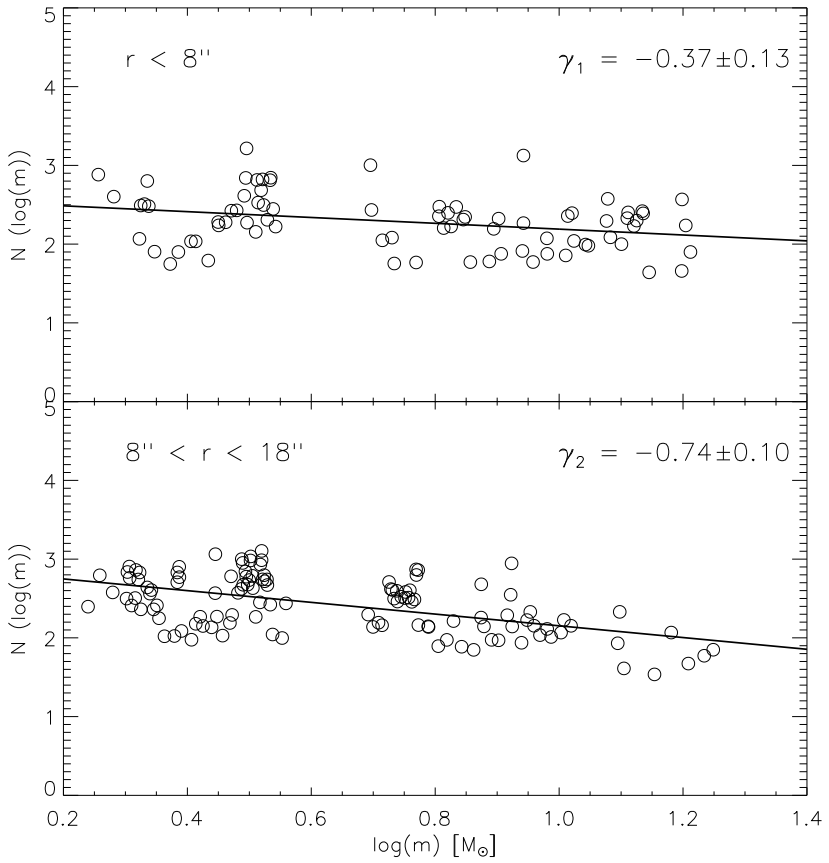

Figure 2.17: Mass functions of the inner region of NYC, derived following the suggested method of Maíz Apellániz & Úbeda (2005). Each 'bin' contains one star, which has been corrected for incompleteness and was divided by the width of the bin. *Upper panel:* PDMF of the inner 8″showing a rather shallow PDMF. The corresponding fit is overplotted as a straight line with a slope of $\gamma_1 = -0.37 \pm 0.13$. *Lower panel:* PDMF of a ring with 8″ as the inner and 17″ as the outer radius. The PDMF appears decreasing steeper, when compared to the inner PDMF. The straight line sows the best-fitting power law with a slope of $\gamma_2 = -0.74 \pm 0.10$.

To minimize the effect of the binning and to maximize the available statistical information, we have chosen to derive the PDMF in single star bins. Therefore, we sorted the stars of our catalogue by mass. Each 'bin' consists of a single star and its bin width is defined to be the mean of the mass of the two adjacent bins. For the most and least massive stars in the sample, the upper and lower boundaries of the bins are chosen to be symmetric about the actual mass of the star. The 'number' (1 by definition) of stars has been corrected for incompleteness associated with the star and divided by the width of the bin.

The resulting PDMF is illustrated in Figure 2.17. It displays two functions for two

regions at different distances to the center of the cluster. Both PDMFs show a shallow increasing function towards lower masses. The masses range from $1.6\,M_\odot$ to $20\,M_\odot$.

We find that both PDMFs are well fitted by a single power law. For the inner $8''$ of the cluster a power law slope of $\gamma_1 = -0.37 \pm 0.13$ is found, which is relatively shallow compared to a Salpeter-IMF with its slope of $\Gamma = -1.35$. Here we have to note that a significant source of uncertainty in the derivation of the MF slope are unresolved binaries. Depending on the binary fraction and the intrinsic slope of the stellar MF, the slope of the PDMF may change significantly (Sagar & Richtler, 1991). However, earlier studies presented similar slopes in the inner region (Harayama et al., 2008; Sung & Bessell, 2004). The PDMF that is derived from the $8'' - 17''$ annulus, shows a significant drop of the slope. It has been measured to be $\gamma_2 = -0.74 \pm 0.10$ which is again consistent with the values of Harayama et al. (2008) but somewhat shallower to the slopes that Sung & Bessell (2004) derived at similar radii. The innermost PDMF derived by Stolte et al. (2006) decreases towards higher masses with a slope of $\Gamma = -0.89 \pm 0.12$ for the region $7'' - 20''$ off the center of the cluster. Within in the error, this value agrees with our measurement. At larger radii, the PDMF was observed not to steepen significantly showing a present mass segregation in the center of the cluster while the outer regions are less affected. However, all derived power laws are notably shallower than the Salpeter slope of $\Gamma = -1.35$ revealing a top-heavy IMF of the cluster which might be a characteristic of such a vigorous star forming events.

2.7 Summary and Conclusions

Based on two epochs of high-accuracy astrometric *HST*/WFPC2 observations separated by 10.15 yr, relative proper motions of 829 stars were measured. A selection of candidate cluster members with $P_{\rm mem} > 0.9$ results in a clean cluster CMD. The best-fitting isochrone yields an age of 1 Myr, a distance of 6.6–6.9 kpc, and $A_{\rm V}$=4.6-4.7 mag for the PMS and intermediate-mass MS cluster members.

Stars at the location of the short-lived radiative convective gap, which occurs at 3.5–3.8 $\rm M_\odot$ at the age of NYC, are identified for the first time. We find hints of a sparse young low-mass population with an age of ~ 4 Myr, which might constitute an earlier generation of star formation in NGC 3603, and likely represents the low-mass counterparts to several blue supergiants in the vicinity of NYC.

For the first time, the internal velocity dispersion of the starburst cluster NYC could be measured. For stars with masses 1.7 $\rm M_\odot$ <M< 9 $\rm M_\odot$, we determine a one-dimensional velocity dispersion of $141 \pm 27 \mu$as yr^{-1}, corresponding to 4.5 ± 0.8 km s^{-1} at a distance of 6.75 kpc. From the fact that the velocity dispersion does not vary with stellar mass in this mass range, we deduce that NYC has not yet reached equipartition of energy. This is not entirely unexpected at the young age of the cluster, since its crossing time is estimated to be 1.4 Myr by Nürnberger & Petr-Gotzens (2002).

The same might be true for many extragalactic starburst clusters, where mass estimates rely on the measurements of velocity dispersions. If these clusters are also not yet in virial equilibrium, their masses might be systematically overestimated. Thus, NYC provides an important benchmark for our understanding of the early dynamical evolution and the long-term survival of young, massive stellar clusters in the Milky Way and in other galaxies.

Comparison of the derived dynamical mass of 17,600 $\rm M_\odot$ with estimates of the photometric mass of 10,000 and 16,000 $\rm M_\odot$ reveals that the cluster is, after the expulsion of its intracluster gas, out of – but not far from – dynamical equilibrium. The star formation efficiency (SFE) can be expressed as

$$\mathrm{SFE} = \frac{\mathrm{M_*}}{\mathrm{M_* + M_{gas}}} = \frac{\mathrm{M_*}}{\mathrm{M}} \tag{2.14}$$

and if we assume that the derived dynamical mass reflects the total mass in the cluster before gas expulsion (which is an underestimation since the cluster had already some time to adjust to the changes of the gravitational potential, it can be written as $\mathrm{M} = \mathrm{M_{dyn}} = \mathrm{M_*} + \mathrm{M_{gas}}$. With the photometric mass of $\mathrm{M_*} = 10,000 \mathrm{M_\odot}$ this yields a SFE for NYC of 57%. Considering a SFE of 30% is required for a cluster to remain bound

after gas expulsion we can predict that NYC will survive this early mass loss event. Even more, the dissolution timescale (not accounting for the early mass loss events) of NYC shows that the cluster if dissolving into the Galactic field through the gradual loss of stars will survive for a few Gyr ($t_{dis} \leq 3\,\mathrm{Gyr}$). The relaxation timescale was estimated to 10 Myr

We derived the MF of NYC for the central $8''$ and for a ring from $8 - 17''$ distance from the cluster. Both PDMFs appear shallower than the Salpeter-IMF showing a top-heavy MF. Variation of the two slopes reveal the present mass segregation in NYC.

Chapter 3

Trumpler 14 with MCAO

3.1 Introduction

As demonstrated in the previous chapter, space based observations offer diffraction-limited observations by avoiding the Earth's atmosphere that hampers high angular resolution. Despite offering a sharp view, space observatories are limited to mirror sizes of 'only' a few meters which results in, comparing *HST* to a 8m-class telescope, roughly ten times smaller collective area.

Studying stellar clusters with ground-based telescopes requires a combination of large FoV and great sensitivity as well as high angular resolution to resolve also the densest regions of such objects. With typical sizes of the order of arcminutes on the sky and including stellar populations down to the least massive and faintest stars observational challenges are introduced by centrally concentrated stellar agglomerations. This made the develoment of the Adaptive Optics (AO) technique indispensable and describes a milestone in connecting large telescopes and high angular resolution. AO systems correct the distortions of the wavefront that are induced by turbulence in the atmosphere. The size of the turbulent cells can be characterized by the coherence length r_0, meaning the length on which the wavefront remains undisturbed. The angle that includes the coherence length from the position of the observer is the isoplanatic angle which is proportional to the coherence length and inversely proportional to the altitude of the turbulence: $\theta_0 \propto r_0/h$. However, these turbulent cells are not constant cells evolve quickly on very short timescales – the coherence time τ_0. AO systems have to operate on these timescales which is related to the coherence length via $\tau_0 \propto r_0/v$, where v is the wind speed at the altitude of the turbulence. Since the atmospheric turbulence changes quickly with time, the corrections of the deformable mirrors must happen on timescales less than the coherence time of the atmosphere which is typically

of the order of milliseconds (e.g., Navarrete, 2011).

Despite this challenging task, AO systems have proven their outstanding ability in compensating atmospheric seeing for more than 20 years (see Figure 3.1 or, e.g., Merkle et al., 1989, 1990). The first common user AO system was the ADaptive Optics Near-Infrared System (ADONIS) and successor of the prototype system COME-ON (Merkle et al., 1989). It was mounted at the 3.6-m telescope in La Silla (e.g., Beuzit et al., 1994; Demailly et al., 1994) and provided the first ground-based diffraction-limited observations with previously unachieved angular resolution to the astronomic community.

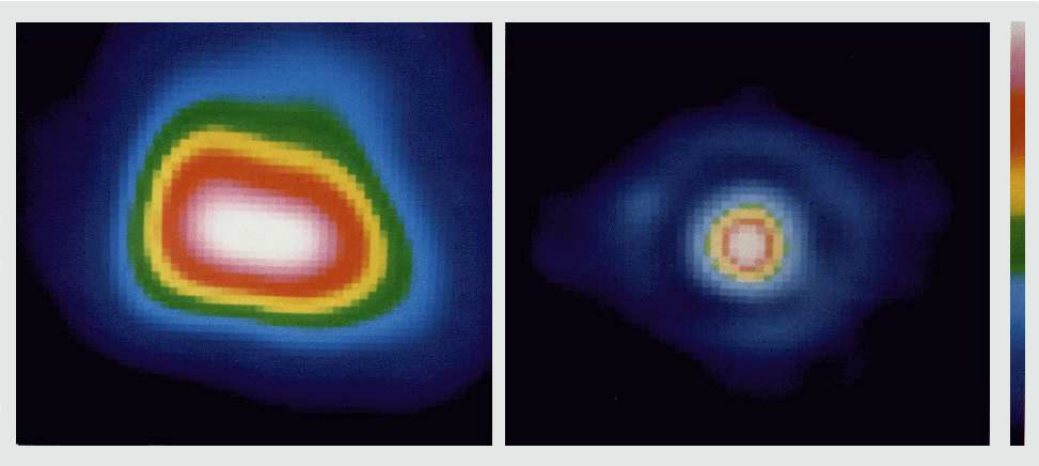

Figure 3.1: L-band ($3.5\mu m$) images of the Be star HR 6519 taken with the ESO 3.6-m telescope on La Silla (from Merkle et al., 1990). *Left*: HR 6519 with an deactivated AO loop, thus, seeing limited observations with seeing conditions of $0.7''$. *Right*: The same L-band image but the AO loop activated. The FWHM of the PSF shrinks from the actual seeing down to $0.22''$, which is the diffraction limit in L-band with the 3.6-m telsecope.

For an improved spatial performance over a larger FoV a spatially more homogeneous AO correction must be provided. Multi-conjugate AO (MCAO) systems are the natural development to provide this stability and to extend the performance of the AO system to larger FoVs. MCAO uses several GSs for computing the correction enlarging, thus, the observable area. In the framework of second generation instruments for the Very Large Telescope (VLT) and the European-Extremely Large Telescope (E-ELT), the Multi-conjugate Adaptive optics Demonstrator (MAD), was developed in 2007 as the first MCAO system at the VLT (Marchetti et al., 2003, 2004, 2007).

As a template to test the 'wide-field' correction of VLT-MAD, NGC 3372 provides an ideal environment to demonstrate the potential of MCAO systems for the studies of compact star clusters. The proximity of the Carina Nebula and its cluster population provides an ideal testbed to assess the capability of MAD since the combination of high

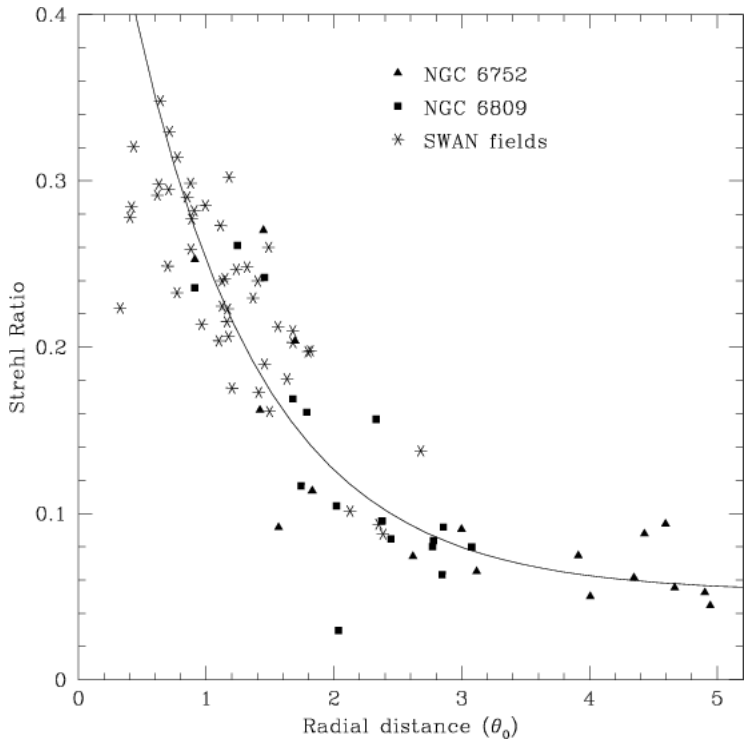

Figure 3.2: The decrease of Strehl ratio as a function of the isoplanatic angle θ_0, thus, as a function of distance from the position of the guide star (taken from Cresci et al., 2005).

spatial resolution and the wide-field at MAD allows to resolve the dense central region of the star cluster Trumpler 14 (Tr 14). NGC 3372, or Carina Nebula, is a Galactic giant molecular cloud and a site of vigorous and ongoing star formation including several young massive clusters (Figure 3.3). It includes not only dozens of young O- and B-type stars but also evolved Wolf-Rayet stars (e.g., Massey & Johnson, 1993). The youngest and most populous clusters of the region are the open clusters Tr 14 and Trumpler 16 (Tr 16), located in the central part of the Carina Nebula. The high-mass population and their strong UV radiation interacts with the surrounding material triggering subsequent star formation (e.g., Rathborne et al., 2002). The stellar population of Tr 14 includes several O-type stars, notably the O2If* star HD93129Aa (Smith, 2006), which has been found to be the most massive star in Tr 14 with an estimated mass in excess of 100 $M_\odot$ (Nelan et al., 2004). Assuming a Kroupa-type mass function this makes the cluster as massive as a few $10^3 M_\odot$ (e.g., Sana et al., 2010) and puts Tr 14 close to the regime of the Galactic starburst clusters like NYC or the Arches Cluster (Rochau et al., 2010; Stolte, 2003). As several studies have revealed, the region is the closest region harboring such a massive young cluster at a distance from the Sun of $2 - 3$ kpc (e.g., Ascenso et al., 2007b). The lack of evolved stars makes Tr 14 a very young cluster. The ages of the high-mass content of Tr 14 and Tr 16 are supposed to be around 1-2 Myr

Figure 3.3: A 2MASS JHK$_S$ image of the Carina Nebula including the two massive young clusters Tr 14 and Tr 16. North is up and east is to the left. The image is centered on Tr 14 while Tr 16 with its brightest member, the luminous blue variable η Carina, is visible in the southeast corner.

(Vazquez et al., 1996) and 2-3 Myr (Smith, 2006), respectively, while the formation of intermediate-mass stars probably started earlier. This is supported by the discovered core-halo structure of the cluster, with the halo being slightly older (Ascenso et al., 2007b). However, the ages of the clusters as well as the distance estimates remain controversial. One reason could be the anomalous extinction law that is observed in the clusters (e.g., Tapia et al., 2003).

3.2 VLT-Multi conjugate Adaptive optics Demonstrator

3.2.1 Optical performance

In the last two decades optical systems for astrophysical observations underwent significant improvements with the development of CCD detectors and the development of the AO technique which reduces the, 'twinkling' of stars during observations: the AO technique improves the performance of an optical system by reducing the distortions of the wavefront caused by the Earth's atmosphere. It measures the distortions of the wavefront and uses deformable mirrors to compensate the atmospheric blurring. Although the idea for such optical systems has existed for almost half a century (Babcock, 1953), the development of the first astronomical optical systems did not take place until the early 1990s.

Despite the outstanding performance of single conjugated AO (SCAO) systems in terms of angular resolution it depends strongly on the proximity to the GS. A measure for the quality of the correction is the Strehl ratio, after the German physicist K. Strehl (Strehl, 1895). The Strehl ratio is defined as the ratio of the measured peak intensity to the peak intensity of a ideal diffraction-limited image of a star of equal magnitude. Figure 3.2 displays the optical performance of AO assisted observations in terms of Strehl as a function of the isoplanatic angle. It reveals the drastic degradation of the AO correction with distance from the GS. Hence, SCAO observations are restricted to a rather small FoV. The isoplanatic angle describes the distance form the GS at which the Strehl ratio has decreased to 1/e of its maximum value and typical isoplanatic angles are of the order of $15''$ and, consequently, typical observed FoVs that provide a sufficient AO correction cover $\sim 30''$.

The correction of the AO system depends on the flux that is received by the wavefront sensor and thus relying on the brightness of the reference star. It also relies on the structure of the atmospheric turbulence and is subsequently strongly anisoplanatic. This limits the possible AO observations to areas on the sky that include stars fulfilling the GS flux requirements. However, AO systems have now proven their outstanding ability in correcting atmospheric seeing over the last 20 years. As mentioned, to provide a spatially more stable performance MCAO systems use several GSs to correct the blurring due to the Earth's atmosphere. Although the idea of multiple GSs is trivial, the technical feasibility remains challenging. The wavefront correction requires bright flux for a proper correction constraining AO observations to areas with nearby bright stars and, subsequently, the adaptability of the MCAO system.

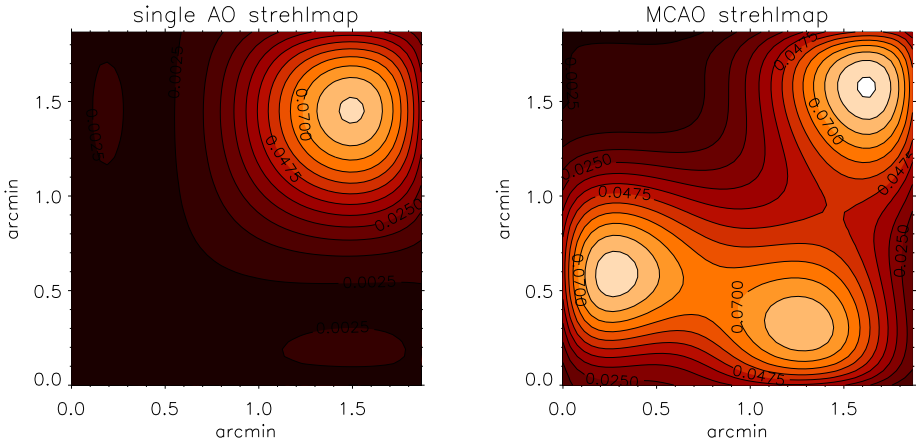

Figure 3.4: Simulated Strehl ratio maps over an 2′ FoV with Strehl ratios calculated according to Equation 2 of Cresci et al. (2005) to display the improvement of a MCAO system. *Left panel:* SCAO Strehl map with the maximum Strehl value according to our K_S-band observation of the central field at the location of the GS. *Right panel:* Strehl map of simulated MCAO observations with three GSs. Maximum Strehl values according to our measurement from the K_S-band observations set to the positions of the three GSs.
The fast drop of performance with distance from the GS for the SCAO is apparent. In the MCAO simulation we observe, in contrast, a relatively smooth spatial distribution of Strehl values over the 2′ FoV. The strong decrease of the Strehl ratio around a single GS is compensated by the AO correction from the other GSs.

3.2.2 Multi-Conjugate Adaptive Optics Demonstrator

As the first prototype MCAO system at the VLT (Marchetti et al., 2003, 2004, 2007), the aim of MAD was to test the technical feasibility of processing observations with multiple GSs. This offers several advantages such as a more moderate decrease of the Strehl ratio due to the higher number of correcting stars leading to a larger corrected FoV. MAD aims at demonstrating the feasibility of MCAO systems in general and to investigate different reconstruction techniques in particular. It is designed to correct blurring due to atmospheric turbulences over 2′ on the sky using Natural Guide Stars (NGS). Two Deformable Mirrors (DM) are used for the MCAO correction. One DM, optically conjugated at the telescope pupil, corrects for the ground layer turbulence while the second DM, conjugated at 8.5 km above the telescope, corrects for the field anisoplanatism.

Two possible ways to operate a MCAO system are the star- and layer-oriented mode, respectively. To examine the differences between the star- and layer-oriented reconstruction technique, two different wavefront sensors (WFS) are installed. The star oriented MCAO correction is supported by an Multi Shack-Hartmann WFS and

the Layer Oriented MCAO reconstruction makes use of a Layer Oriented Multi-Pyramid WFS. Both WFSs are able to sense simultaneously several NGS at visual wavelength but only one WFS will be used at a time. In our study the observations were carried out in star oriented mode.

MAD is equipped with the IR camera CAMCAO (CAmera for MCAO) using a HAWAII2 2kx2k HgCdTe detector. With a image scale of $0.028''$/px the camera has a $59'' \times 59''$ FoV (Amorim et al., 2006). A $2' \times 2'$ FoV can be covered by moving the camera while the telescope is tracking and the AO loop remains closed. This combination of wide field coverage and high angular resolution provides the ideal instrument for observations of Galactic clusters which are usually extended over a few arcminutes and, thus, makes MCAO the ideal instruments to observe stellar systems such as Tr 14.

Table 3.1: Details of the observations of the four different pointings. Note that the number of stars show the result of the PSF photometry for each region. The overlap between the four fields has not been accounted for, thus a star appearing in more than one field has been counted accordingly. Observations have been carried out at airmasses between 1.2 and 1.5

Name	Filters	$t_{\rm exp}$(s)	$t_{\rm tot}$(s)	Stars
Tr14main	H, K_S	$28 \times (30 \times 2s)$	1680	1347
Tr14south	H, K_S	$16 \times (15 \times 2s)$	480	519
Tr14east	H, K_S	$16 \times (15 \times 2s)$	480	437
Tr14southeast	H, K_S	$16 \times (15 \times 2s)$	480	493

3.3 Observations and data analysis

We proposed to use VLT-MAD to observe the relatively close massive young cluster Tr 14 in H- and K_S-band. Observations were carried out during the night of July 17, 2008 by the VLT-MAD team. Deep H and K_S images were obtained to map the innermost region of the young massive cluster Tr 14 ($\alpha = 10^h43^m55^s, \delta = -59^o33'03''$). Four different pointings with CAMCAO were used to cover a $2' \times 2'$ FoV. Single DITs are chosen to 2 seconds to reduce saturation while the minimum DIT of ~ 0.8 seconds was avoided to keep a useful fraction of overheads. Single images of one minute were obtained ($NDIT \times DIT = 30 \times 2s = 60s$). The pointing on the central area of the cluster has been chosen to be the deepest observation with almost 30 minutes of exposure time, while the adjacent three fields were observed for only 8 minutes each. A summary of the observations can be found in Table 3.1.

Raw data reduction and image combination was processed using the ESO image processing software Eclipse (Devillard, 2001). For sky and dark subtraction as well as for flat field correction the calibration images taken during the science run were used. The sky and dark subtracted, flat field corrected images are subsequently combined. For the core of the cluster, 28 single images with 1 min of exposure time (30×2s, short DITs to avoid saturation) were combined to a single frame with 28 min of total integration time. For image combination we used the shift and add function of the jitter tool of Eclipse. The final FoV of the central field covers an area of $68'' \times 68''$.

The same procedure has been used to combine the 16 different images, with $15 \times 2s = 30s$ of exposure time each, of the three remaining fields. The four different pointings together cover an area of $\sim 1.7' \times 1.7'$. A HK$_S$ color composite of the covered area is shown in Figure 3.5. Clearly visible is the most massive member HD93129Aa as the brightest star in the field. The three GSs (marked by green circles in Figure 3.5) are enclosing a triangle without too acute angles, thus, well suited for a good MCAO

performance.

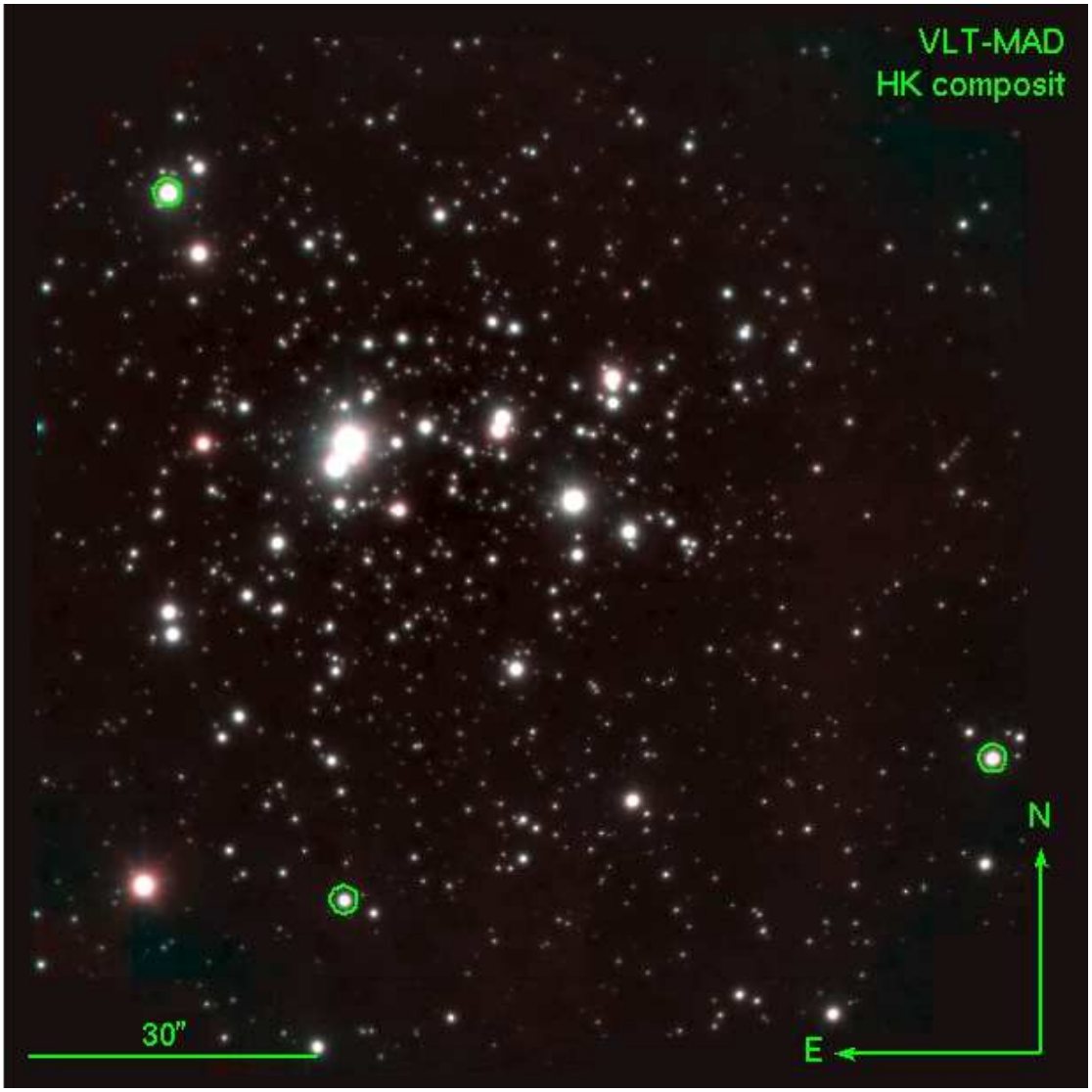

Figure 3.5: Central core of Tr 14 as seen with VLT-MAD ($1.7' \times 1.7'$). This H,K_S color composite shows the densest region of the cluster including the most massive cluster member HD93129Aa as the brightest star in the field. The three chosen guide stars for the MCAO system are marked with green circles.

3.4 Technical analysis of the MCAO data

To demonstrate the basic idea of improvement of the AO performance with MCAO systems, we simulated a SCAO and MCAO observations over a $2'$ FoV. Since SCAO supported observations are restricted to a rather small FoV due to isoplanatic angles of the order of $\sim 15''$, the isoplanatic angle has been chosen accordingly, $\theta_{iso} = 15''$. The Strehl ratio decreases with distance to the GS. We assumed that the radial variation follows a trend as given by Equation 2 of Cresci et al. (2005):

$$SR = S_0 exp[-(\frac{\Delta\theta}{\theta_{iso}})^{\frac{5}{3}}] \tag{3.1}$$

with θ_{iso} as the isoplanatic angle and S_0 as the maximum Strehl ratio of the observation. Figure 3.4 shows the comparison of a SCAO performance (left panel) with the performance of a MCAO system using three GSs (right panel). The positions of the GSs and their associated maximum Strehl ratios have been set according to our K_S-band observations (see Table 3.2 in Section 3.4.1).

To investigate the corrective performance of the MCAO systems by comparing computed and observed Strehl ratios, we extracted stellar properties in the combined images of the different regions using Sextractor (Bertin & Arnouts, 1996). This lead to a measurement of the peak flux as well as the full width at half maximum (FWHM) of the detected sources. The mean FWHM was found to vary between $0.22''$ and $0.26''$ in H- and K_S-band, respectively. In comparison, the seeing limited NTT/SofI observations of Tr 14 by (Ascenso et al., 2007b) had a FWHM around $0.7''$. The relatively bad seeing conditions, under which the observation were accomplished, hampered a better correction. Considering the good geometry and brightness of the GSs together with good seeing conditions allow MAD to easily achieve AO corrections down to a FWHM of $0.15''$, or even below. Photometry of the NTT-SofI observations is later used for photometric calibration (Section 3.4.3). The theoretical diffraction-limited PSF was created with *imgen* of the *Eclipse* software. We derived the Strehl ratios of our H- and K_S-band observations and created, subsequently, corresponding Strehl maps.

To quantify the difference between MC- and SCAO, we compared our observations to simulated SCAO observations. We created a grid representing our observed MAD FoV and assigned values of Strehl ratios to each grid element with maximum Strehl ratios located at the GS positions. Maximum Strehl values are chosen according to our observations. The spatial variation of the Strehl ratio was assumed to follow Equation 3.1 (Cresci et al., 2005) with S_0 as the maximum Strehl ratio and an isoplanatic angle $\Theta_{iso} = 15''$ as a typical value of SCAO observations.

3.4.1 Performance in the central region

Results of the simulations for the central field are summarized in Table 3.2 together with the results from our observations. In the simulations we found mean Strehl values of 2% and 1.6% for the H- and K_S-band, respectively.

The distributions of Strehl ratios in the H- and K_S-band observations are shown in Figure **??** and **??** as contours superimposed onto the corresponding image. Maximum Strehl values of 9.8% (H-band) and 12.6% (K-band) were measured. The Strehl map reveals further a shallow decrease of the Strehl ratio over the FoV indicated by mean Strehl ratios of 6.0% for the H-band and 5.9% for the K_S-band observations. The larger mean Strehls ratios in our MAD observations reveal the improved spatial stability of the PSF in our MCAO observations compared to SCAO ones.

Although SCAO observations provide higher peak Strehl ratios, the decreasing performance with distance to the GS makes a good characterization of the PSF at larger distances difficult. Especially in crowding-limited sources, such as dense stellar clusters, this hamperes the census of the stellar population. The greater homogeneity of the PSF provided by MCAO observations allows, therefore, the coverage of larger AO corrected areas on the sky, crucial for studies of extended stellar populations.

Table 3.2: Strehl values over the $1' \times 1'$ FoV

Origin	Filter	max. Strehl	min. Strehl	mean Strehl	stddev of Strehl ratio
Obs. MCAO	H	9.8%	3.3%	6.0%	1.25%
Obs. MCAO	K_S	12.6%	1.3%	5.9%	1.6%
Sim. SCAO	H	9.8%	$< 0.01\%$	1.6%	2.4%
Sim. SCAO	K_S	12.6%	$< 0.01\%$	2.1%	3.1%

3.4.2 Performance in the outer regions

The central field and the three adjacent fields offer data of different photometric depth. Therefore, we divided the analysis into the different pointings concerning their total exposure time. In the following we will carry out a similar analysis as in the previous section for the smaller and shallower observations of the adjacent field in the proximity of the center of Tr 14. To evaluate the MCAO performance, Strehl ratios have been derived as described in Section 3.4.1. The corresponding maps of Strehl ratios in H- and K_S-band for the three different fields are shown in the Figures 3.6- 3.8. The iso-Strehl levels are again shown as contours superimposed onto the corresponding images. The simulations assessing the discrepancy between SCAO and MCAO described in

Section 3.4.1 have been used to assess the wide-field performance of VLT-MAD. We have computed the SCAO simulation over the entire 2′ FoV and cut out the corresponding area for the different fields.

East: The field to the east of the center of Tr 14 does not include any of the three GSs. Therefore, the rather small maximum Strehl value with 6.3% has been observed in the H-band. The highest Strehl in the K_S-band is still relatively large with 12.3%. However, the high values are located in the southern part of the chip close to the GS in the southeastern frame. The decrease of Strehls is still quite shallow which is depicted by the small standard deviations of 0.6% for the H-band and 1.8% for the K_S-band around mean Strehl ratios of 3.1% and 7.6% for the H- and K_S-band, respectively. We have not analysed simulated SCAO observations for the eastern field due to the absence of the GS.

Table 3.3: Strehl values eastern region

Pointing	Origin	Filter	max. SR	min. SR	mean SR	stddev of SR
East	Obs. MCAO	H	6.3%	0.6%	3.1%	0.6%
East	Obs. MCAO	K_S	12.3%	1.6%	7.6%	1.8%

South: The region to the south of the center of Tr 14 hosts one of the GSs. The spatial distribution of Strehls is comparable to the central field and agrees well with the simulated MCAO observations. Strehl ratios have been derived and are similar to the central field with 9.0% and 14.7% as peak values and mean values of 4.2% and 7.7% for the H- and K_S-band. Compared to simulations reveal significantly lower means of 1.8% and 3.0% for the SCAO simulations.

Table 3.4: Strehl values of the southern region

Pointing	Origin	Filter	max. SR	min. SR	mean SR	stddev of SR
South	Obs. MCAO	H	9.0%	0.4%	4.2%	1.1%
South	Obs. MCAO	K_S	14.7%	3.0%	7.7%	2.1%
South	Sim. SCAO	H	9.0%	$< 0.01\%$	1.8%	2.1%
South	Sim. SCAO	K_S	14.7%	$< 0.01\%$	3.0%	3.4%

Southeast: The region to the southeast of the center of Tr 14 is another field hosting a GS. Maximum Strehl and mean values are found very similar to the other two GS-hosting field with 9.5% (max.) and 6.3% (mean) in H-band and 13.8% (max.) and 9.5% (mean) in K_S-band.

All three regions including a GS are showing a similar AO performance underlying the wide-field corrective power of VLT-MAD. Even in the eastern field, without any

GS, we observe a reasonably well performance. The shallow degradation of Strehl ratios over the $2'$ FoV reveals and proves the superiority of a MCAO system comparing the spatial stability of the PSF and demonstrates the feasibilty of an MCAO system to correct the atmospheric blurring over a significantly larger area on the sky.

Table 3.5: Strehl values of the southeastern region

Pointing	Origin	Filter	max. SR	min. SR	mean SR	stddev of SR
Southeast	Obs. MCAO	H	9.5%	1.6%	6.3%	1.4%
Southeast	Obs. MCAO	K_S	13.8%	2.1%	9.5%	1.8%
Southeast	Sim. SCAO	H	9.5%	$< 0.01\%$	1.9%	2.2%
Southeast	Sim. SCAO	K_S	13.8%	$< 0.01\%$	2.7%	3.2%

3.4.3 Photometric calibration and completeness

Photometric calibration

To study the stellar content of Tr 14, we use IRAF/DAOPHOT (Stetson, 1990) to perform PSF photometry. We found a Penny-PSF, consisting of a Gaussian kernel and Lorentzian wings, as the best-fitting PSF to our observations. In addition, a second order variable DAOPHOT PSF provides a good match to the MAD data obtained in the star-oriented mode. Photometric calibration was performed using the photometric data of Tr 14 based on NTT-SofI observations by Ascenso et al. (2007b). Their calibration is based on 2MASS photometry.

Comparing NTT-SofI photometry with our MAD photometry provides the zero point (ZP) offsets for the MAD photometry. Offsets in the photometry as a function of right ascension and declination after calibration are shown in Figure 3.10, depicting the stability over the detector. The figure shows that the ZP offset is constant across the MAD FoV, i.e. there are no systematic effects in our photometry due to anisoplanatism or variable Strehl ratios. A linear fit to the observed distribution quantifies the difference in the photometry and provides the ZP correction which has been used for calibration. After applying the derived offset, the final photometry was checked for any deviations with magnitude or for the presence of color terms. No variation was detected in either case. The final photometric catalogue includes 1347 stars. Excluding stars with DAOPHOT photometric uncertainties above 0.1 mag (375 sources), we used a catalogue of 972 stars for the further analysis. It comprises stars over a dynamic range of $\sim$ 10 mag down to $K_S \sim 18.85$ mag.

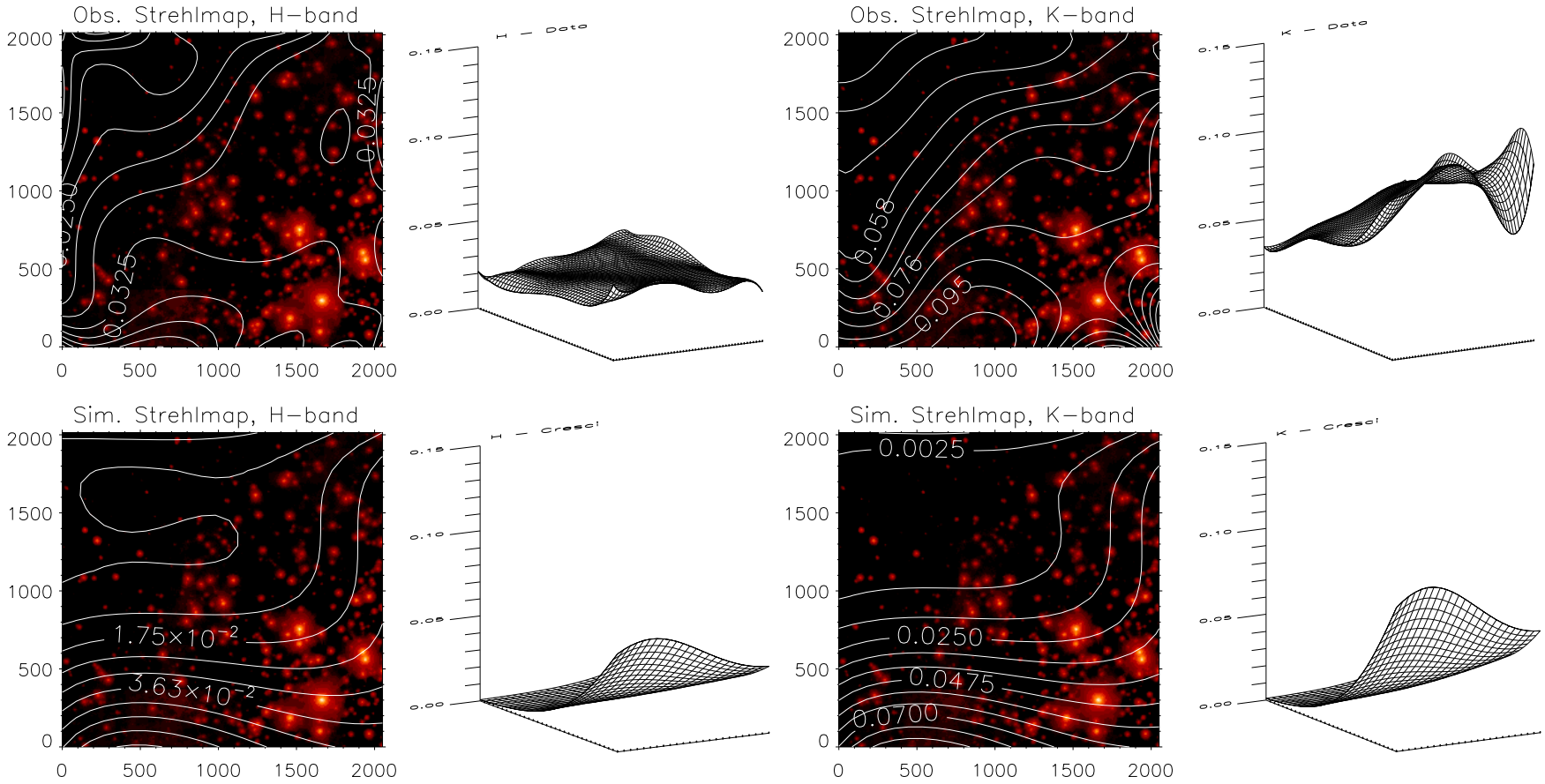

Figure 3.6: H- and K$_S$-band Strehl maps for the eastern region and the corresponding MCAO simulation. No prominent peak is observed due to the lack of a GS in the observed FoV

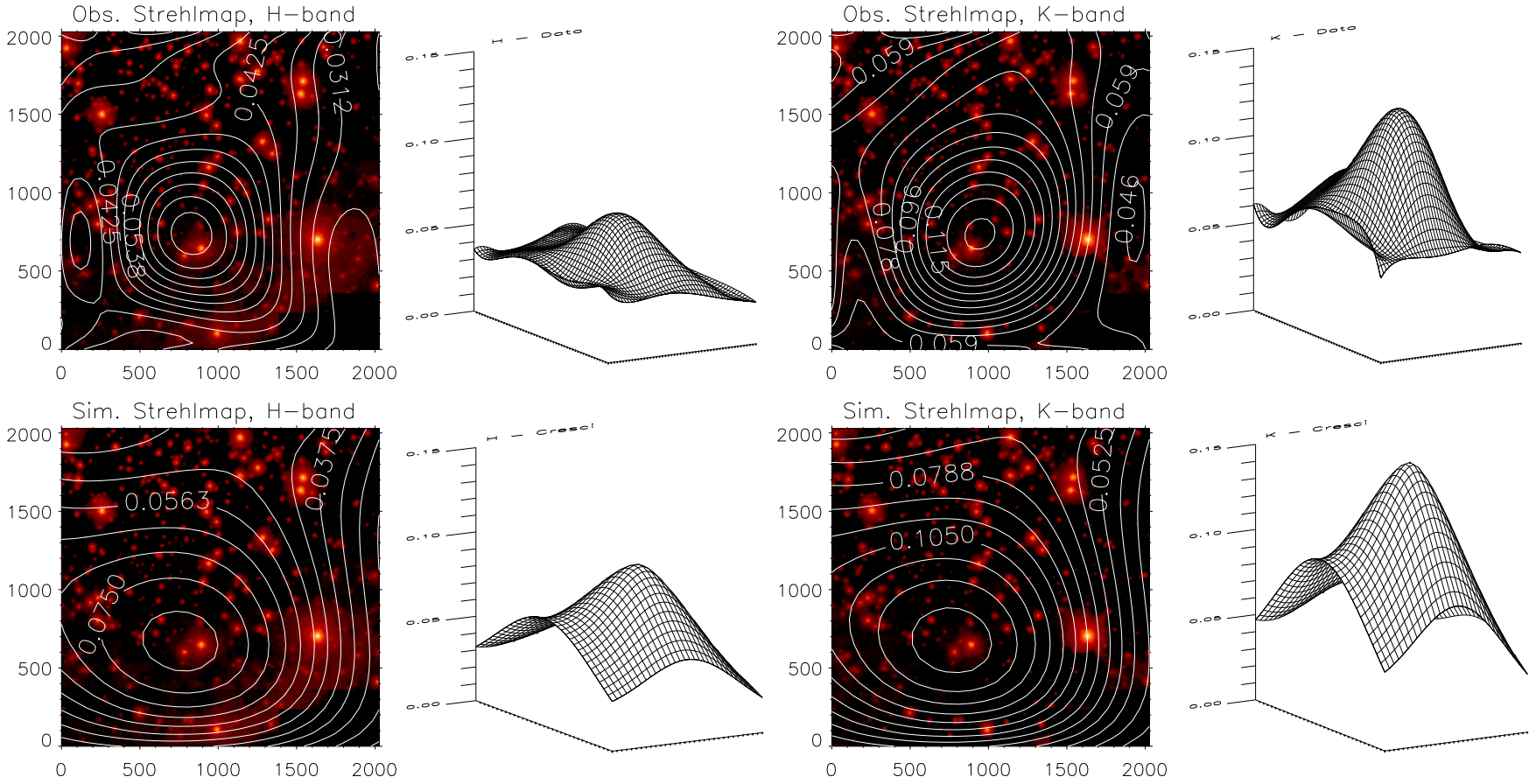

Figure 3.7: H- and K_S-band Strehl maps for the southern region and the corresponding MCAO simulation. The spatial variation of the Strehl ratios is similar in the observations and the simulations.

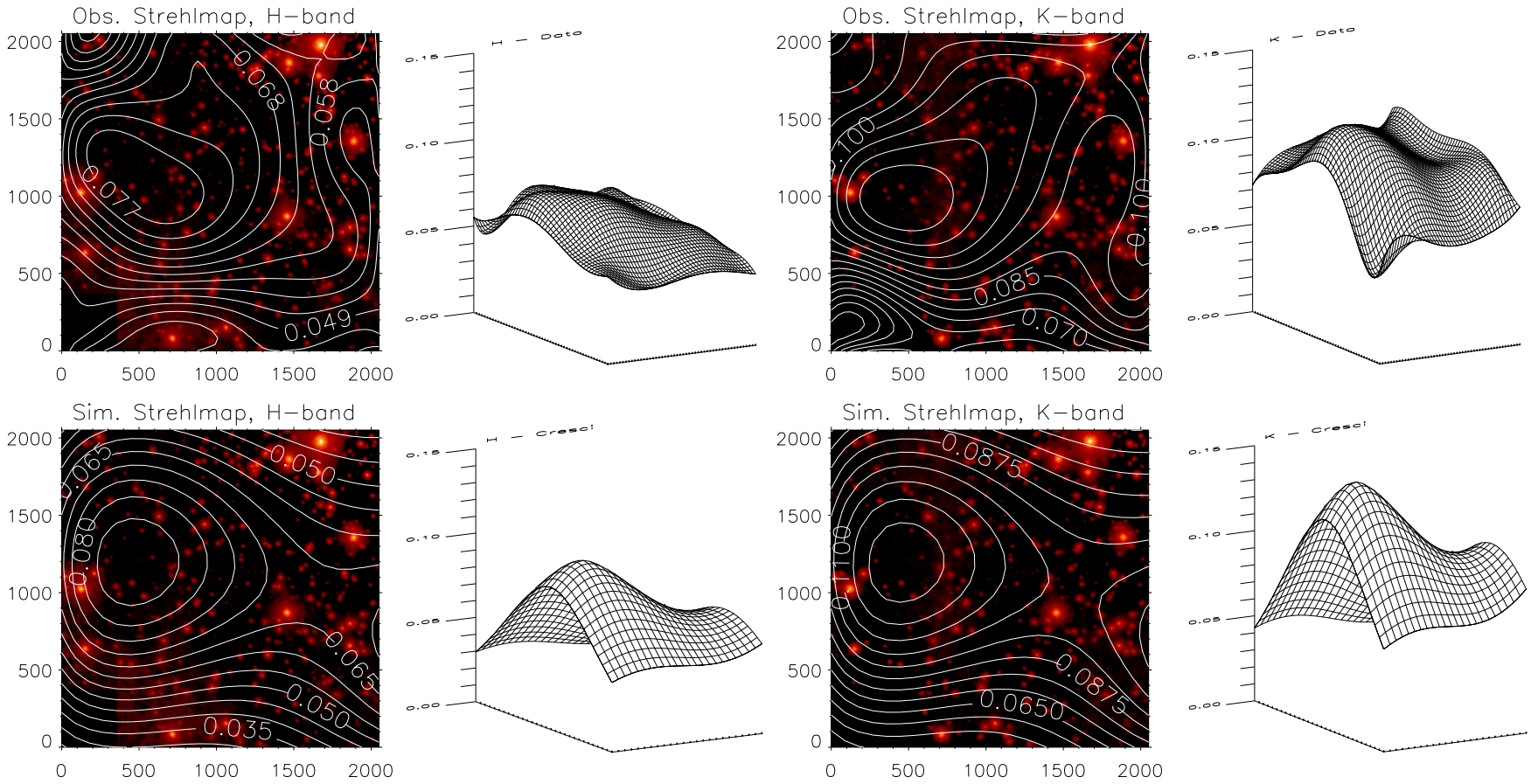

Figure 3.8: H- and K_S-band Strehl maps for the southeastern region and the corresponding MCAO simulation. The observed maximum Strehl values are found around the GS and the values decrease similar to the simulated Strehls.

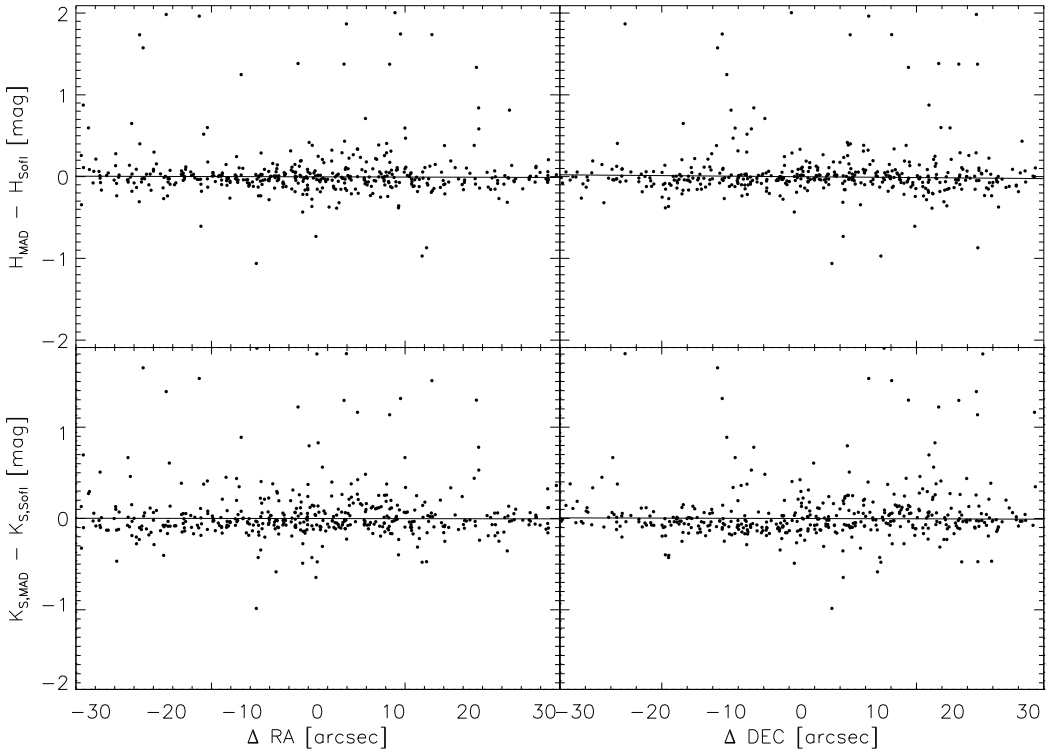

Figure 3.9: Observed differences between the MAD and the NTT-SofI photometry after application of the constant zero point (ZP) correction. ZP offsets are measured and plotted as a function of right ascension (left panels) and declination (right panels) for the H-band (upper panels) and K_S-band (lower panels). Straight lines show the linear fit to the observed distribution revealing the spatial stability of the photometry when compared to seeing limited observations.

Completeness

As described in Section 2.6, accurate knowledge of the completeness function is key information in order to derive a correct LF and, subsequently, a correct MF. In dense clusters the completeness does not only depend on the brightness of the source but on the crowding characteristics of the cluster.

We derive the completeness function $C_j(x, y, \mu)$ (Equation 2.13) with the same technique as in Section 2.6. We re-processed the photometry on the science image with 50 additional artificial stars. 100 iterations were carried out leading to a total of 5,000 added stars for each photometric bin of 0.5 mag width. Estimating the fraction of recoveries provide the completeness. With 5,000 stars added in total we achieved a typical separation between simulated stars of $d_{sim} \sim 34$ pixel. Given our average Full-Width at Half Maximum (FWHM) after the AO correction of $\sim 0.25''$, we sample the whole frame on a scale which is about ~ 4 times the PSF. Only 50 stars were added per iteration to maintain the crowding characteristics of our Tr 14 observations.

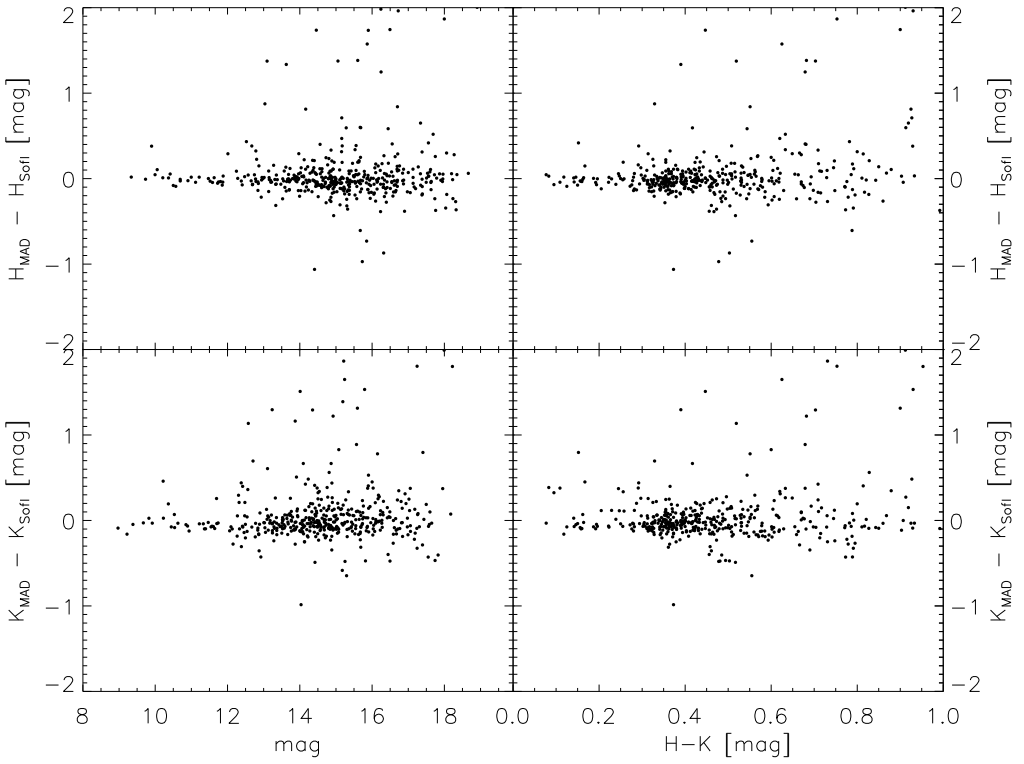

Figure 3.10: Photometric offset after the calibration as a function of magnitude (left panels) and as a function of H-K_S color (right panels). In all cases the offset does not show any variation with magnitude or exhibit any color term.

Derivation of the parameters α, β and γ, we can assign a completeness factor to each star according to its position and brightness.

The left panel of Figure 3.11 shows the K_S-band image of Tr 14 for the central field with the 70% completeness limits at different magnitude superimposed as contours. The right panel depicts the same completeness limits over the observed field as a function of magnitude. For the adjacent fields we assessed the completeness in the same way and the resulting maps are shown Figure 3.12. From top to bottom the corresponding maps for the eastern, southern and southeastern field are displayed.

The limiting magnitude increases significantly in the proximity of the brightest stars while in the area with fainter stars the completeness shows a smooth distribution over the field with a rather faint average limiting magnitude. This illustrates the resolving power of MAD and, in addition with the proximity of the cluster, reveals that crowding is not a major source of incompleteness compared to the stellar faintness.

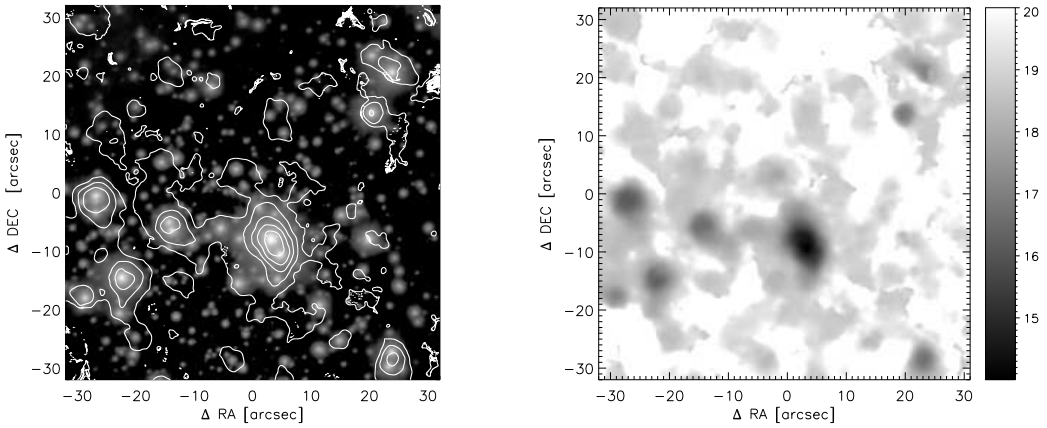

Figure 3.11: K_S-band completeness map of Trumpler 14. *Left Panel:* K_S-band image of Trumpler 14 with 70%-completeness limits superimposed as white contours. The contour levels cover a magnitude range between 15 mag< K_S <19 mag (in steps of 1 mag). The image is centered (0/0) at $\alpha = 10^h43^m57.2^s, \delta = -59°23'44.2''$. *Right Panel:* K_S-band completeness map of the entire observed FoV. The grey shades correspond to the K-band magnitude at which a completeness of 70% is achieved. The strong local decrease of completeness close to bright stars without displaying any global structure shows that crowding effects are less important compared to a possible faintness of the stars.

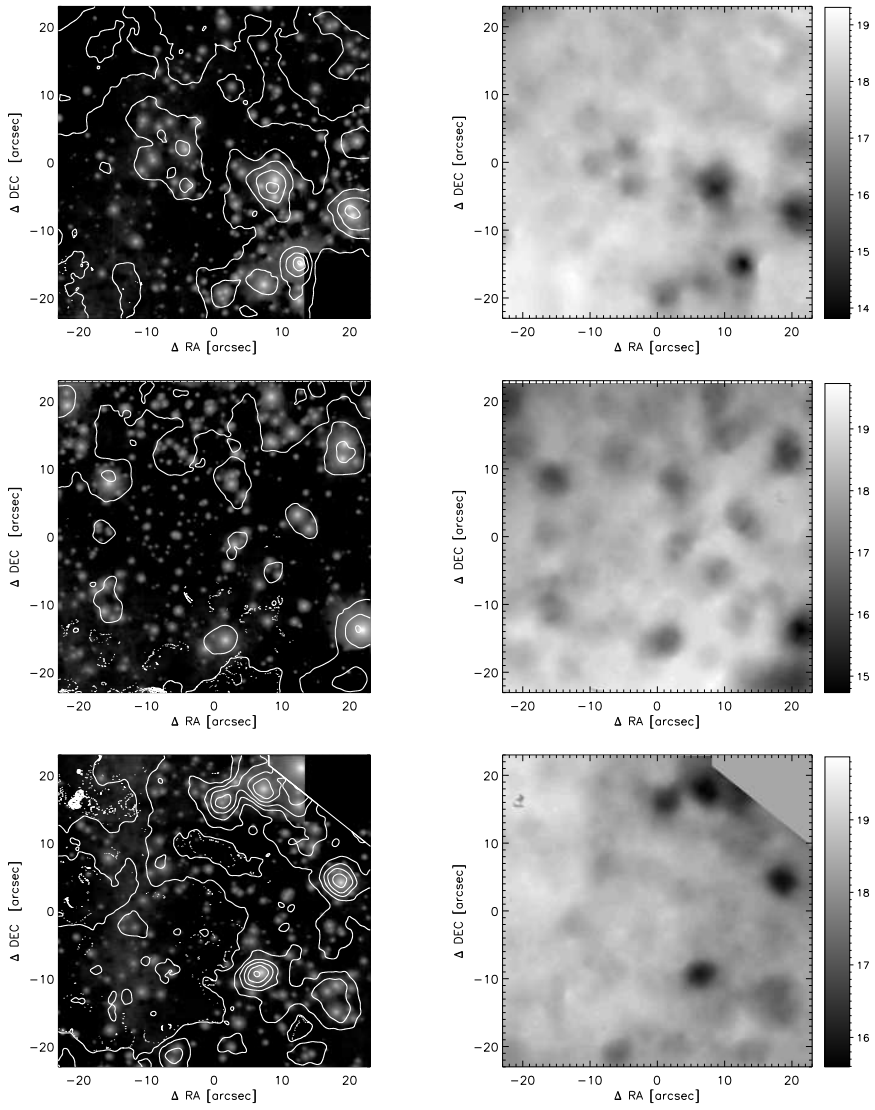

Figure 3.12: K_S-band completeness map of Tr 14. *Left Panels:* K_S-band images of Trumpler 14 (*top:* east, *middle:* south, *bottom:* southeast) with 70%-completeness limits superimposed as white contours. *Right Panels:* K_S-band completeness map of the entire observed FoV. The grey shades correspond to the K-band magnitude at which a completeness of 70% is achieved. We identify again strong local changes of the completeness in the proximity of bright stars. The absence of global structures (as in Figure 2.6) shows that crowding effects are less important.

3.5 Scientific analysis of the MCAO data

3.5.1 MAD color magnitude diagram

With the photometry of the deep central field, we created a K_S vs. H-K_S CMD shown in Figure 3.13. The CMD allows the identification of the cluster population, primarily the clusters pre-main sequence (PMS) population between 10 mag< K_S <16 mag and 0.2 mag< $H - K_S$ <0.5 mag. The transition from PMS to the MS is sparsely populated but can be identified at 10.5 mag < H < 12 mag with 0.1 mag < $H - K_S$ < 0.3 mag. Stars redder than H-K_S=0.5 mag suffer either from severe differential extinction in the region, are background objects, highly reddened by the Carina Nebula or belong to the cluster as PMS stars surrounded by circumstellar material such as a disk causing the K_S-band excess. Without a comparison field, we cannot precisely quantify the contaminating fore-and background field star population and, hence, subtract statistically the contaminating field.

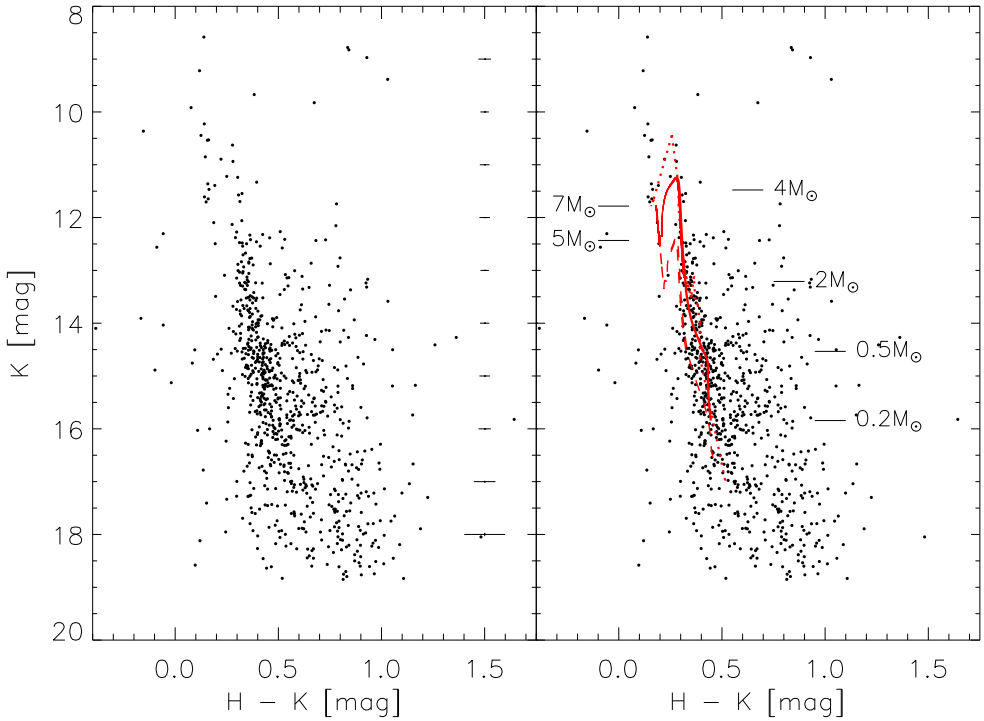

Figure 3.13: K_S vs. H-K_S CMD of the central 0.75 pc of Tr 14. The cluster population can be identified as the dense region of the CMD and goes down to (and beyond) the H-burning limit. It is well represented by a Siess isochrone of 1 Myr in age (thick red line), but ongoing amd continuous star formation might still be present in Tr 14, represented by the younger (0.5 Myr; thin red line) and older isochrone (3 Myr; dashed line). Labeled masses are taken from the 1 Myr old isochrone.

The identification of the cluster sequences (PMS, PMS-MS transition region) allows the comparison with stellar evolutionary models. We used Siess models (Siess et al., 2000), computed as in Da Rio et al. (2009), using the BT-Settle grid of Allard & Freytag (2010). As shown by Allard & Freytag (2010), this grid matches very well the empirical colors of stars in the NIR wavelength range, so we are confident in assuming this models as representative of the H and K_S colors of Tr 14. Isochrones that resemble the observed features are shown in the right panel of Figure 3.13 superimposed onto the CMD. The cluster PMS is best represented by the 1 Myr isochrone indicating that Tr 14 is a very young stellar population. The derived distance modulus ($DM = 11.8 \pm 0.2$ mag) corresponds to a measured distance of $\sim 2.3 \pm 0.2$ kpc. The visual extinction was simultaneously measured to $A_V = 3.0 \pm 0.2$ mag, using $R_V = 4.16$ (Carraro et al., 2004) and the relation of visual and near-infrared extinction according to Cardelli et al. (1989). The distance and extinction estimates are comparable with earlier derived photometric distances (e.g., Ascenso et al., 2007b; Carraro et al., 2004). With a different combination of distance and extinction ($d = 2.6 \pm 0.2$ kpc, $A_V = 2.8 \pm 0.2$ mag), a slightly younger isochrone (0.5 Myr) represents as well the PMS-MS transition region around $K_S \sim 11$ mag (see Figure 3.13 or Sana et al., 2010). However, isochrones of ages below 1 Myr should be handled with care due to the unknown initial conditions the cluster emerged from. Furthermore, the PMS-MS transition is sparsely populated which might lead to erroneous estimates of the age (e.g., unresolved binaries).

Comparing the CMD with the Siess isochrones, we identify the 1 Myr isochrone to best resemble the PMS. However, a number of stars to the blue are inconsistent with the isochrone (14 mag$< K_S <$ 16 mag). Photometric uncertainties alone seem not to be large enough to explain their positions in the CMD. An alternative explaination is that they belong to a somewhat older population of PMS stars of 3 Myr. This supports earlier statements of continuous star formation in the Carina Nebula, creating a surrounding older halo population with ages up to 5 Myr (Ascenso et al., 2007b).

3.5.2 Luminosity function

Selection of different populations

Since the observations have been carried out without observing a comparison field, the isolation of the cluster population remained challenging. In order to get a better idea of the cluster population we applied the following approach: We created a Hess diagram based on our H- and K_S-band observation (left panel of Figure 3.14)which shows the stellar density in the color-magnitude plane rather than the single stars.

The Hess diagram was divided into 20 strips, 0.5 mag wide, along the PMS. In

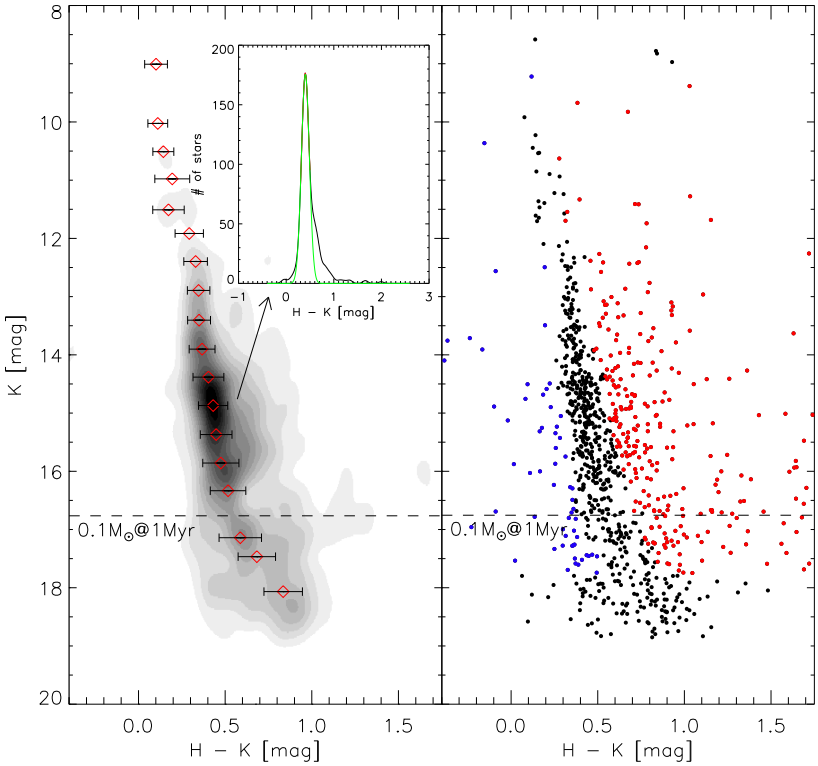

Figure 3.14: *Left Panel:* Hess diagram based on our photometric catalogue. To distinguish the bulk of the PMS stars from the blue and red population of the CMD we cut the Hess diagram into strips of 0.5 mag in magnitude. The red diamonds show the central magnitude of each bin (y-axis) and the color of the peak of the underlying density (x-axis). The erros bars show the 1σ-deviation from the fitted Gaussian function and the different populations have been divided by being either in- or outside the 1.5σ limit. *Right Panel:* The CMD as in Figure 3.13 with the identified 'blue' and 'red' population highlighted. The blue population has not been considered at deriving the LF of Tr 14 while the red population has been included. *Inlay Panel:* An example of the density distribution for a magnitude bin (here: 14.6 mag$<$ K_S $<$ 15.1 mag). The black line shows the stellar density as a function of color and the peak and its immediate surrounding was used to fit the Gaussian function. The best fit is overplotted as the green line.

each bin we counted the number of stars as a function of color. An example of such histogram is shown in the inlay diagram in Figure 3.14. Around the peak we find a rather symmetric distribution, which is well represented by a Gaussian function; the peak positions are highlighted as red diamonds in Figure 3.14. The best-fitting Gaussian function fit is shown by the green line superimposed to the stellar distribution. $1\,\sigma$ deviations from the peak are plotted as the vertical error bars.

We intend to isolate the bulk of PMS stars from the 'blue' field population as well as from the red sources which are excess or extincted sources from the cluster or

background objects. Comparison of the Hess diagram with the CMD revealed that a limiting deviation of $1.5\,\sigma$ divides best the different populations. Sources being off the peak are considered as MS field stars (bluer than peak) or as 'reddened' cluster sources (redder than the peak) and displayed by the blue and red dots in the right panel of Figure 3.14, respectively. Constraining the different regions of the CMD is in our case the best way to get a least biased view onto the stellar population of Tr 14 and, subsequently, the best possible LF.

K-band Luminosity Function

The LF is the number of stars as a funcition of magnitude. To build the LF we considered the CMD of the cluster shown in Figure 3.13 and the different 'populations' that have been identified in Section 3.5.2. Stars of the PMS (black dots in Figure 3.14) and of the PMS plus the reddened sources, respectively, are counted in magnitude bins of 0.5 mag and the counts are corrected for incompleteness. The LF has then been normalized to the considered area. The final K_S-band LF is shown in Figure 3.15. The two panels show the same LF in linear scaling (upper panel) and in logarithmic scaling (lower panel). Both panels include the uncorrected LF (histogram), the completeness corrected LF (thick solid line) and the completeness corrected LF of the PMS plus the sources identified as 'red' sources (dashed line). The steep increase for stars fainter than $K_S \sim 16.5$ mag in the LF is due to the faintness of the stars and the subsequent high incompleteness.

Figure 3.15 shows a rising function for the bright stars which turns into a decreasing function between K_S=14.5 mag and K_S=15.5 mag, corresponding to the mass bin with $0.2\,M_\odot < M < 0.5\,M_\odot$. After the turnover we observe a decreasing function until the incompleteness leads to a steep rise. Decreasing K_S-band LFs has been identified in several clusters (Zinnecker & McCaughrean, 1991) and by simulating model LFs of synthetic clusters (e.g. Lada & Lada, 2003). Also Zinnecker & McCaughrean (1991) simulated primarily K-band LF for coeval clusters of non-accreting PMS stars. They found time-dependent LFs exhibiting maxima that shift with time. Comparing our LF with the maxima at $K_S \sim 14.75$ mag with the results of Zinnecker & McCaughrean (1991) reveal comparable functions for clusters between 0.7 and 1 Myr. Such maxima can be caused by Deuterium-burning stars that lead to a peak and a turnover of the LF. In a 1 Myr old cluster a PMS star of $0.3\,M_\odot$ starts burning Deuterium, which is in agreement with the masses we find to correspond with the observed peak in the LF. The mass-luminosity relation that is obtained from the applied 1 Myr PMS isochrone is visible in Figure 3.16. It shows a bump at $\sim 3.5\,M_\odot$ which corresponds to the PMS-MS transition. Due to such bump we have a degeneracy concerning the K_S-band brightness

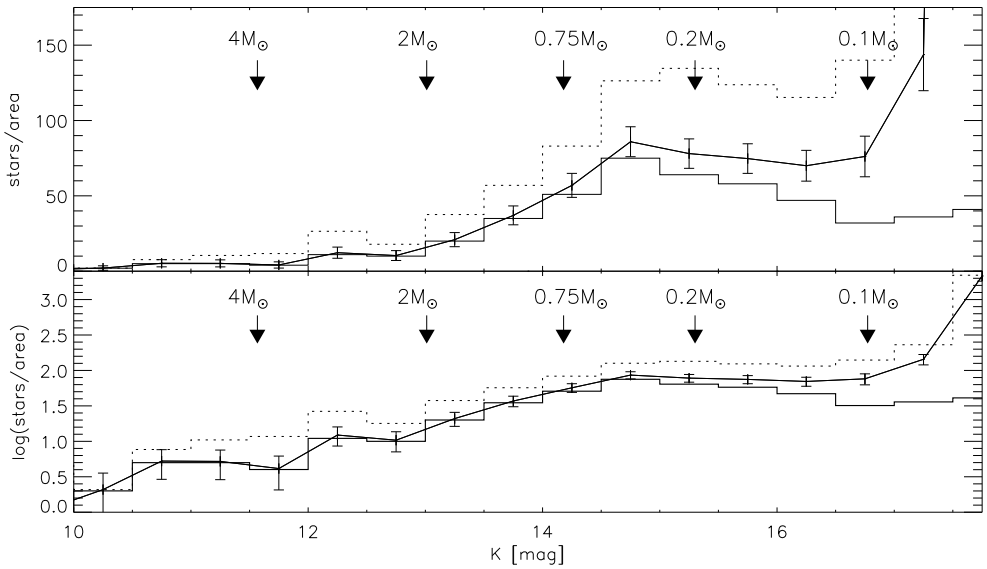

Figure 3.15: *Upper Panel:* K_S-band LF of Tr 14. Displayed is the number of stars found in magnitude bins of 0.5 mag normalized to the observed area. The histogram shows the number of detected sources while the straight line depicts the same number but corrected for incompleteness. The dashed line is the completeness corrected LF including also 'red' sources. *Lower Panel:* The same LF as in the upper panel but with the abscissa showing the logarithmic number of stars; again the LF (histogram), the completeness corrected LF (straight line) and the PMS+'red' sources LF (dashed line) are shown. The errors in both panels are from Poisson statistics of each bin and set accordingly to the logarithmic scale in the lower panel. Masses, highlighted by the arrows are taken from the 1 Myr Siess isochrone. The LF rises with decreasing magnitude to a turnover observed in the $0.25\,M_\odot - 0.54\,M_\odot$ bin (PMS) and/or in the $0.18\,M_\odot - 0.25\,M_\odot$ bin (PMS+'red' sources).

due to PMS getting fainter when approaching the MS. In our LF we observe a small excess at ~ 12.5 mag which we identify as being caused by the stars which are close to the ZAMS. Such a feature in the LF, if clearly identified, can be used as an age indicator, since the turn-on point to the MS depends on the age of the stellar systems such as the turn-off point of the MS.

3.5.3 Mass luminosity relation

We have used the 1 MyrPMS isochrone of our modified Siess tracks (Siess et al., 2000; Da Rio et al., 2009) to derive the relation between the stellar luminosity and present mass since most of stars of Tr 14 are populating the PMS which ends with the ignition of the central hydrogen at the turn-on. The present mass is given as well as the absolute magnitude by the stellar models. To obtain the MLR for Tr 14 the distance and extinction of the cluster have to be considered. From the isochrone fitting procedure we

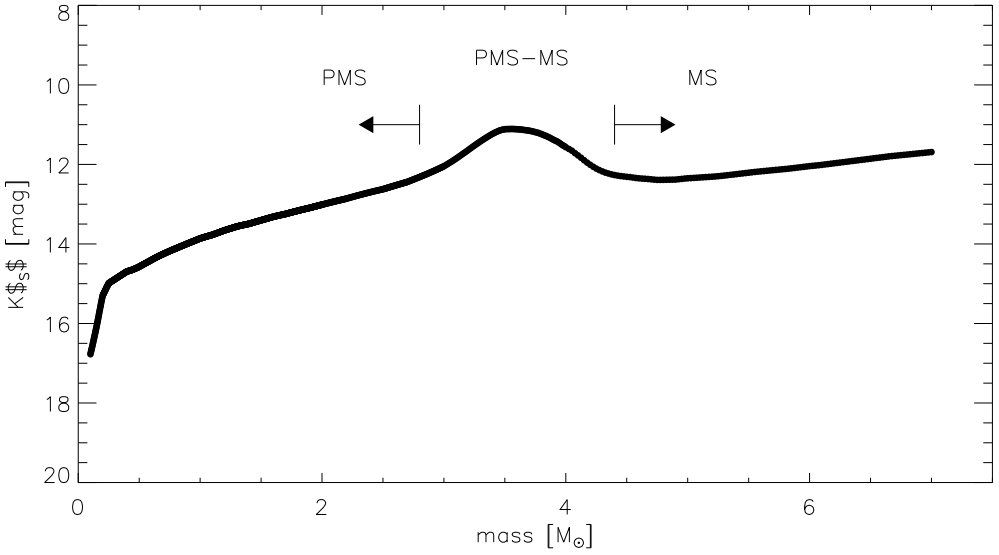

Figure 3.16: Mass luminosity relation for Tr 14 based on the applied 1 Myr Siess isochrone. The bump around $3.5M_\odot$ corresponds to the PMS-MS transition. At lower masses, the stars are still in their PMS phase while at masses M> $4.5M_\odot$ stars are populating the MS.

have reddening and distance modulus which have been used to relate the present mass to the observed magnitudes. The apparent magnitude as a function of the present mass is shown in Figure 3.16. Subsequently, a present stellar mass is derived and ascribed for each star, estimated with the derived MLR.

The turn-on to the MS has been found at $K_S \sim 11 - 12$ mag (Section 3.5.1). Figure 3.16 shows an almost linear depence of the apparent magnitude from the mass for stars fainter than $K_S \sim 12$ mag. The evolutionary phase of the PMS is going down towards substellar masses and represented by the steep decline in stellar brightness with decreasing stellar mass (Figure 3.16). The bulk of the PMS, with masses between $0.2\,M_\odot$ and $\sim 3.5M_\odot$, shows a almost linear relation between stellar brightness and mass. The bump, observed between $3.1M_\odot$ and $4.25M_\odot$ describes the stars in the transition phase from a fully convective PMS star to a MS star that is stabilized by the hydrogen burning. Towards even higher masses we see a linear increase towards higher masses that represent the MS for masses up to $7\,M_\odot$.

3.5.4 Mass function

The Trumpler 14 Mass Function

As seen in Section 2.6.2, the slope of the PDMF can be described by

$$\gamma = \frac{d \log N(\log \mathrm{m})}{d \log \mathrm{m}} \ , \tag{3.2}$$

where $N(\log \mathrm{m})$ is the PDMF. Thus it counts the logarithmic number of stars in logarithmic mass bins. We use the MLR of Figure 3.16 in order to obtain the PDMF of Tr 14. In the case of Tr 14, a single age model fits the cluster reasonably well, we used the MLR taken from the 1 Myr Siess isochrone and ascribed the present mass to each star which belongs to our stellar sample of the cluster.

To derive the PDMF of Tr 14, we used again the method suggested by Maíz Apellániz & Úbeda (2005). Minimizing the bias of the binning, we derived the PDMF from single star bins. The resulting PDMF is illustrated in Figure 3.17. It displays two functions composed of *i)* only the PMS stars (index: PMS_i) and of *ii)* PMS stars and the 'red' sources (index: all_i). Both PDMFs show a decreasing with mass in the regime of the intermediate- and low-mass stars ($\mathrm{M} \gtrsim 0.55\,\mathrm{M}_\odot$ in contrast to an increasing function between 0.25 and $0.55\,\mathrm{M}_\odot$. Towards even lower masses we see the PMDF rising again with a second turnover observed at $\sim 0.175\,\mathrm{M}_\odot$. It is not clear whether this increasing number of stars with lower masses is a feature of the cluster or, more likely, caused by an increasing contribution of the field population or an increasing incompleteness of the stellar sample. Therefore, stars with $log(m) < -0.6$ are not considered for the fit to the PDMF of Tr 14. We find that above $0.25\mathrm{M}_\odot$ it is well fitted by a two-component power law which turns over at a characteristic mass. Power law slopes were found to $\gamma_{PMS_1} = -0.45 \pm 0.19$ and $\gamma_{all_1} = -0.31 \pm 0.12$ for the higher mass component. Within the errors both PDMF slopes agree with each other but are notably shallower than the Salpeter slope of $\Gamma = -1.35$. Although unresolved binaries may alter the slope of the stellar PDMF significantly (Sagar & Richtler, 1991), even with a high binary fraction, the change in slope would not be large enough to resemble the Salpeter- or Kroupa-IMF in that mass regime.

Characteristic masses at which the PDMFs turn over are found to $0.63\,\mathrm{M}_\odot$ (PMS) and $0.49\,\mathrm{M}_\odot$ (PMS+red sources). For the lower masses, we observed a flatter PDMF towards lower masses down to $\sim 0.25\,\mathrm{M}_\odot$. Power law slopes change to $\gamma_{PMS_2} = 0.52 \pm 0.62$ and $\gamma_{all_2} = 0.72 \pm 0.34$, respectively. The observed turn-over at $\sim 0.175\,\mathrm{M}_\odot$ cannot be clearly identified as a real feature of Tr 14, primarily due to the unknown contribution of the Galactic field. However, such a turnover has been observed at similar masses in

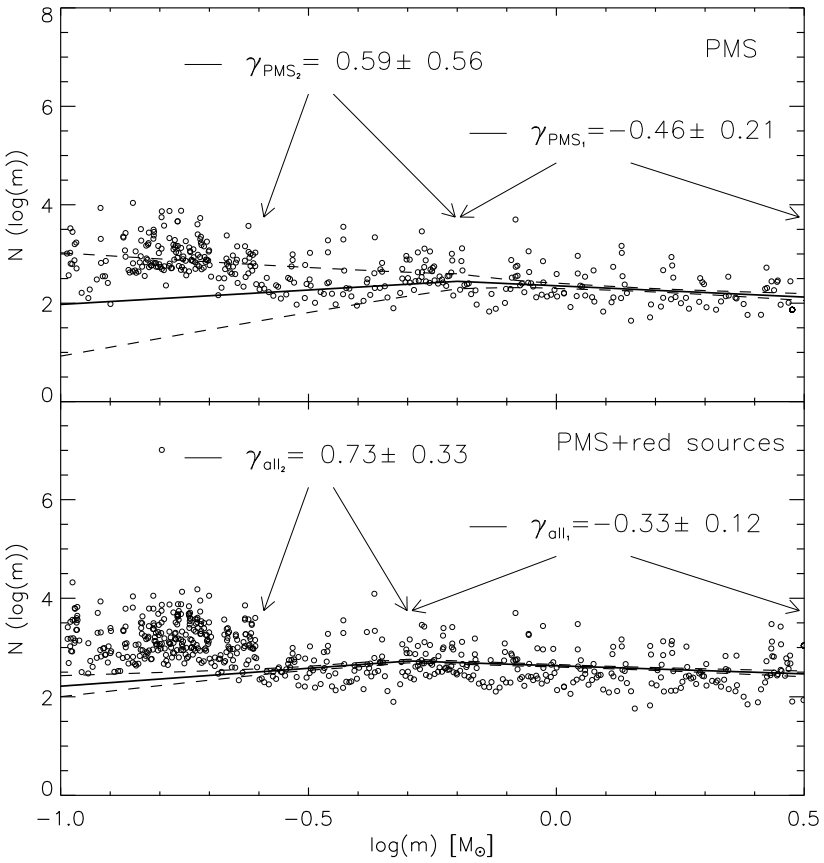

Figure 3.17: Mass function of Tr 14 derived following the suggested method of Maíz Apellániz & Úbeda (2005). Each 'bin' contains a single star, which has been corrected for incompleteness and was divided by the width of the bin. The two MFs are composed of stars of only the PMS (upper panel) and of the PMS plus the 'red' sources (lower panel). The best fits to the MFs are shown as straight lines while dashed lines display the 1σ interval. The 'high-mass' part is well represented by a power law with a slope of $\gamma_{PMS_1} = -0.45 \pm 0.19$ (PMS) and $\gamma_{all_1} = -0.31 \pm 0.12$ (PMS+red sources). The 'intermediate' part appears increasing with stellar mass ($\gamma_{PMS_2} = 0.52 \pm 0.62$ (PMS) and $\gamma_{all_2} = 0.72 \pm 0.34$ (PMS+red sources) with a turnover observed between $\sim 0.5\,M_\odot$ (PMS+red sources) and $\sim 0.63\,M_\odot$ (PMS). At even lower masses we tentatively see another turnover at log(m)~ -0.75 .

various clusters of different mass (Bastian et al., 2010, and references therein).

The mass of 0.5-0.6 $M_\odot$, at which the flattening is observed, agrees very well with the change in slope of the Kroupa-IMF (Kroupa, 2001). However, the exponents of a Kroupa-IMF above $0.5\,M_\odot$ is more like a Salpeter-IMF (Salpeter, 1955, , $\alpha = -1.35$). Below $0.5\,M_\odot$ the Kroupa-IMF is a rising function towards lower masses ($\alpha = -0.3$) rather than a flat or decreasing function that we found in Tr 14. In comparison with the Salpeter-IMF and Kroupa-IMF, our PDMF appears shallower in the intermediate-

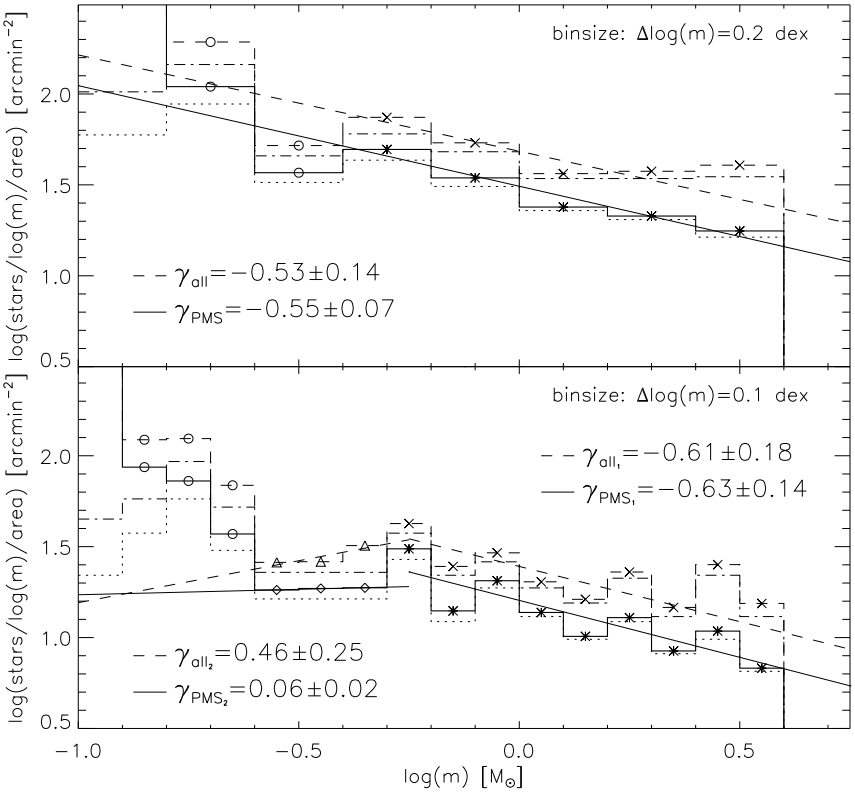

Figure 3.18: Mass functions of Tr 14 derived with the 'traditional' method. *Upper Panel:* The PDMF through star counts with bin of $\Delta log(m) = 0.2$dex. Above $0.5\,M_\odot$ it is in agreement with the PDMF ($\gamma_{PMS} = -0.55\pm0.07$ and $\gamma_{all} = 0.-53\pm0.14$). *Lower Panel:* The PDMF of Tr 14 from counting stars in bins of $\Delta log(m) =$ 0.1dex. We observe similarly shallow slopes of $\gamma_{PMS} = -0.63 \pm 0.14$ and $\gamma_{all} = -0.61 \pm 0.18$ for the higher mass regime. At $\sim 0.5\,M_\odot$ we observe a turnover with slopes of $\gamma_{PMS} = 0.46 \pm 0.25$ and $\gamma_{all} = 0.06 \pm 0.02$.

and low-mass part, meaning more stars towards higher masses. Such an overabundance is suggestive for the lower mass stars being affected by the more massive population. Even more, our observations only cover the central arcminute of Tr 14, i.e., only the inner 0.75 pc of the cluster. In mass segregated clusters more massive stars are more centrally concentrated leading to a shallow MF in the high-mass regime and the effect of the higher mass stars is, consequently, enhanced. Furthermore, in the very-low-mass regime we observed a shallower PDMF, depicting fewer stars than expected. In consequence, the lower the mass of a star the larger is the fraction of stars missed when expecting a Kroupa-IMF for Tr 14. Possible explainations for such a deficiency of very-low mass stars could be a smaller formation rate for such stars or a result of mass segregation expelling these stars from the cluster center to larger orbits. However, the latter has only been observed for stars above $10\,M_\odot$ (Sana et al., 2010).

The observed features of a flattening of the MF around $\sim 0.55M_\odot$ and a turnover at

Table 3.6: Slopes of the different mass functions

Mass range [$M_\odot$]	Binning	γ_{PMS}	$\sigma_{\gamma_{PMS}}$	γ_{all}	$\sigma_{\gamma_{all}}$
$m_c - 3.4\,(2.5)$	1 star	-0.45	0.19	-0.31	0.12
	0.1 dex	-0.61	0.18	-0.63	0.14
	0.2 dex	-0.53	0.14	-0.55	0.07
$0.25 - m_c$	1 star	0.52	0.62	0.72	0.31
	0.1 dex	0.06	0.02	0.46	0.25
	0.2 dex	—	—	—	—

$\sim 0.2 M_\odot$ is not an unique feature of Tr 14, but observed in several other clusters. For instance, similar features at comparable mass are observed in the Orion Nebular Cluster (ONC, e.g. Hillenbrand, 1997; Da Rio et al., 2010). The PDMF of Da Rio et al. (2010) shows a flattening of the MF at $log(m) \sim -0.45$ and a turnover at the same location as we found in Tr 14 at $log(m) \sim -0.75$. Interestingly, compared to the Kroupa-IMF the ONC-IMF exhibit an overabundance in very-low-mass stars, in constrast to our finding of a deficiency of such stars. Even more, the turnover at $0.2\,M_\odot$, if a real feature of Tr 14, fits to the observations of several clusters displaying a change from an increasing to a decreasing function towards lower masses. Some examples are the ONC, as mentioned, as well as IC 348, and σ Ori showing such a break at comparable masses (Bastian et al., 2010, and their Figure 3).

'Traditional' Mass Function

For comparison, we constructed the PDMF also in the 'traditional' way, counting stars in logarithmic mass intervals with $\Delta log(m) = 0.2\,dex$ and $\Delta log(m) = 0.1\,dex$. Stars were counted and the counts normalized to the considered area. The results are corrected for incompleteness and the resulting PDMFs are shown in Figure 3.18. Above $0.5\,M_\odot$ the derived power law slopes agree within the errors with the PDMF of Figure 3.17. Towards lower masses we also identify the drop of the mass function below $0.5\,M_\odot$ followed by an steep increase below $0.25\,M_\odot$. The 0.1 dex spacing provide only three data points in that mass range to allow to fit a power law to the distribution. Power laws slopes agree with the derived values from the PDMF of Figure 3.17. In all three cases (Figure 3.17 and 3.18) we have not fitted the MF below $0.25\,M_\odot$, due to an assumed higher contribution of the field and/or the uncertainties introduced by the increasing incompleteness. The corresponding slopes of all MFs are summarized in Table 3.6.

3.6 Radial (in)dependence of the mass function

We have derived the LF and the MF for the central region of Tr 14 in the Sections 3.5.2 and 3.5.4. The area covered by our observations further allows to investigate whether or not mass segregation is present in the cluster. To assess the presence of a possible mass segregation we study the radial dependence of the mass distribution. We, therefore, combined the four catalogues of the different regions to a single catalogue. The correspoding map of all detections is shown in the left panel of Figure 3.19.

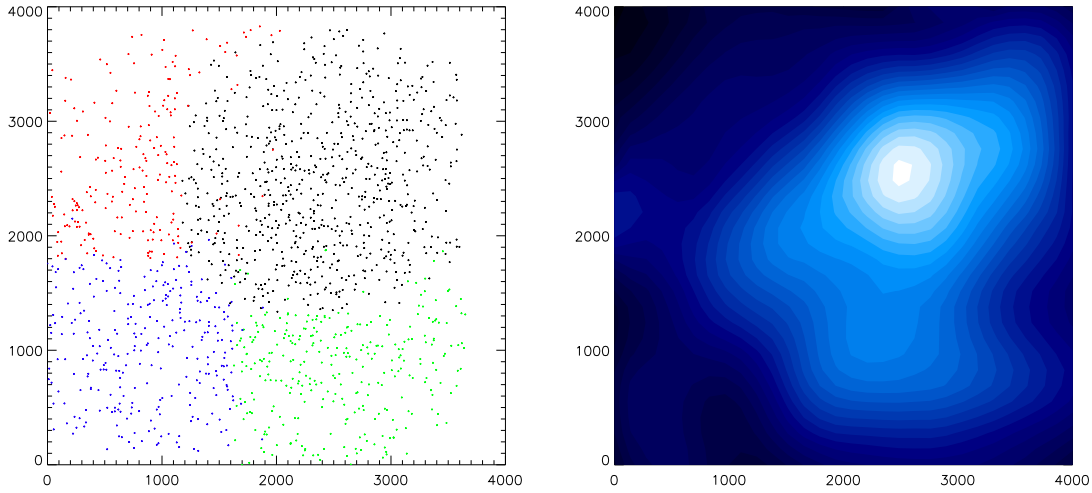

Figure 3.19: *Left panel*: Map of all stars that are detected in the four pointings. North is up and east is to the left. Stars of the deepest observations of the center are shown as black dots, the detections of the other pointings are shown in red dots (eastern region), blue dots (southeastern region) and green dots (southern region). *Right panel:* Density map of the same area to determine the center of the cluster. The dark blue shades show the area of lower density, brighter region corresponds to a higher stellar density. The center is seen as the bright region in the upper right area.

In order to study the radial variation of the PDMF, we have to determine the center of the cluster. Stellar positions are used to derive a density map of the region. We subdivided the covered area into a grid of boxes of 100×100 pixels in size and counted the stars in each box. The number was corrected for incompleteness associated with the stars, thus, we derived the density according to:

$$\rho_{i,j} = \frac{\sum_{i,j} N_{ij} \times C_{ij}}{A} \tag{3.3}$$

where ρ describes the stellar density, N_{ij} the number of stars with the corresponding completeness C_{ij} that have been counted in box ij. A finally describes the area of the

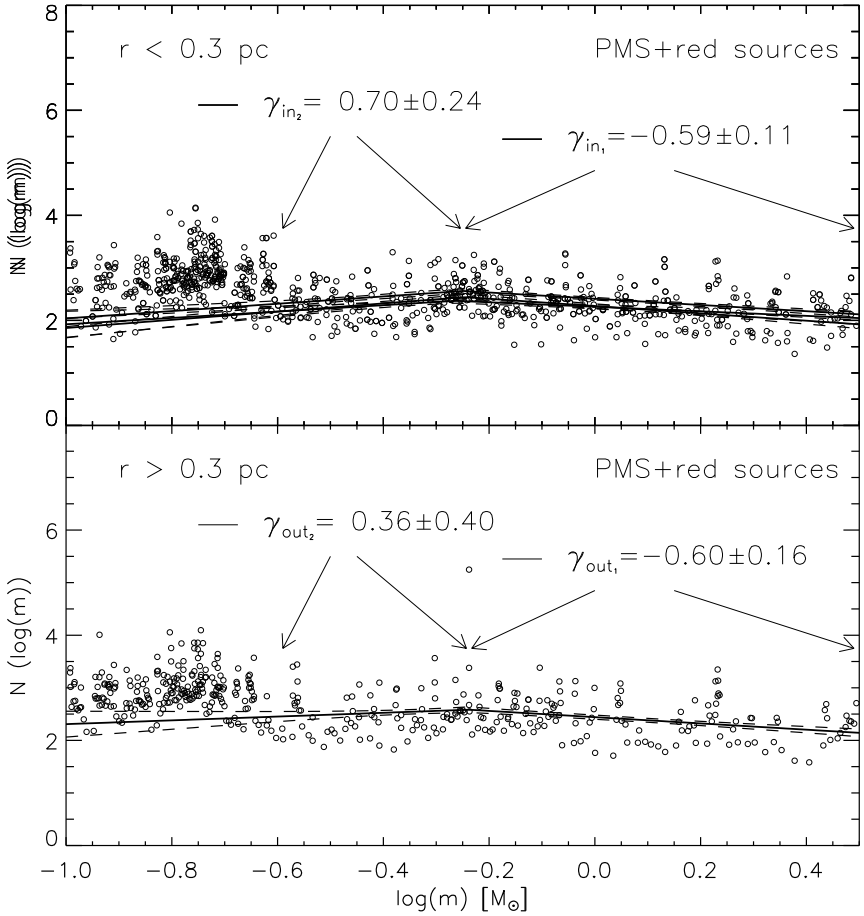

Figure 3.20: Two PDMFs derived as described in Section 3.5.4. The upper panel displays the PDMF of the inner 0.3 pc of the cluster while the lower panels shows the same PDMFs but for the stars beyond 0.3 pc. Power law slopes of the higher mass part agree very well. Also the lower mass regions show comparable slopes within the error, although these are quite large. The similarity of the power law slopes reveal the absence of mass segregation.

box. A smoothed version of the density map is shown in the right panel of Figure 3.19. Dark blue shades are displaying areas of relatively low stellar density while brighter contours show an increasing stellar density. The center of the cluster can be clearly identified as the bright spot in the upper right and show a rather symmetric profile. We fitted a 2D Gaussian function to the region around the peak to determine the position of the peak density which was subsequently used as the cluster center.

A diagnostic tool for the detection of the phenomenon of mass segregation in a star cluster is its PDMF, which is expected to be radially variable if mass segregation is present. Therefore, in order to see whether Tr 14 shows mass segregation or not, we derived its PDMF for the central region and a second PDMF which describes the mass

distribution beyond the very inner core. At the central region we selected the inner 0.3 pc of Tr 14 (assuming the distance of 2.3 kpc), which corresponds to 960 pixels of our MAD observations. For the 'outer' region every star detected beyond this radius has been considered.

We derived the different PDMFs as described in Section 3.5.4 for the two selected radial distances. The resulting PDMFs are shown in Figure 3.20. As in the PDMF of the central region we fitted a two-phase power law and excluded the region of the increasing PDMF for masses below $\sim 0.25\,M_\odot$ log(m) $= -0.6$. The resulting best fits are overplotted as straight lines with the $1\,\sigma$ intervals shown as dashed lines. Due to the lower density beyond 0.3 pc and since the PDMFs of Figure 3.17 show no significant difference if derived only from the PMS or from PMS and the 'red' sources, we derived the inner and outer PDMF from the combined sample of PMS and 'red' sources.

Table 3.7: Slopes of the different mass functions

Region	γ_1	σ_{γ_1}	γ_2	σ_{γ_2}	ch. mass [$M_\odot$]
inner region	-0.59	0.11	0.70	0.24	$0.56 M_\odot$
outer region	-0.60	0.16	0.36	0.40	$0.58 M_\odot$

The derived PDMFs are shown in Figure 3.20 with the inner PDMF in the upper panel and the outer PDMF in the lower panel. In the higher mass regime the PDMF decreases similarly with power law slopes of ~ -0.60, thus no variation could be identified. For the lower mas regime ($0.25 M_\odot - 0.52\,M_\odot$) slopes have been found to vary between 0.41 and 0.68; differences in the PDMF are visible, but the uncertainty of the derived values hamper a clear identification as an intrinsic feature of the radial mass functions. Interestingly the associated characteristic mass, that was derived simultaneously, appeared at very similar masses consistent with the value derived earlier for the PDMF of the PMS stars. It was found to be $log(m) = -0.24 \pm 0.14$ and $log(m) = -0.25 \pm 0.05$, corresponding to a mass between 0.56 and $0.58\,M_\odot$. Slopes of the two PDMFs are listed in Table 3.7 and do not show a significant variation as it would be expected in a mass segregated cluster. This depicts the absence of segregation on the very inner region of Tr 14 among the stars considered ($0.25 M_\odot - 3.2\,M_\odot$).

Sana et al. (2010) also investigated a possible mass segregation in Tr 14 using the same data set. Instead of examining the radial dependence of the MF they used minimun-spanning tree approach. Their result agree with our finding as they observed mass segregation only for stars with masses larger than $10\,M_\odot$. Our analysis supports the absence of mass segregation below $3.2\,M_\odot$. However, the origin of the concentration of the high-mass stars is still elusive, it could be either of dynamical origin, via stellar encounters, or the massive stars are formed in the centers of clusters, the so-called

primordial mass segregation.

3.7 Summary

We presented deep H and K observations of the young massive cluster Tr14, observed with MAD, the first MCAO system at the VLT. We revealed an impressive performance of the AO system over a large FoV. By showing maps of Strehl ratios show a low variation over the $68'' \times 68''$ FoV. Mean Strehl values are measured to 11.5 and 10.5 with a standard deviations of 2.0 and 2.4 in H- and K-band, respectively. Simulation of single AO observation over the same field of view revealed smaller mean Strehls (5.0 in H and 4.9 in K) with larger standard deviations (4.2 in H and 4.7 in K). Although with lower maximum Strehl ratios (17.3 in H-band, 19.6 in K-band), when compared to single AO systems, this shows a significant improvement of the spatial stability of an AO performance and demonstrates the superior performance of MCAO systems for wide-field AO corrected observations.

PSF photometry has been applied to derive properties of Tr14. Photometric calibration was accomplished using seeing limited NTT/SofI observation. A constant offset of 1.52 mag in H and 2.02 mag in K was found compared to seeing-limited observations (Ascenso et al., 2007b). The photometric catalogue comprises 819 sources which were used to create the deepest infrared CMD of Tr14 so far, reaching $K \sim 18.85$ mag which corresponds to 0.1-0.2 $M_\odot$ on the PMS. When compared to the expected population of field stars, we find the CMD best represented by an isochrone of 1 Myr in age while hints for ongoing star formation as well as for an older population which supports a scenario of continuous are observable. Star formation over the last 3 Myr would support earlier studies concluding with a slightly older halo population (Ascenso et al., 2007b).

This study reveal the great improvement of AO corrections provided by MCAO systems in case of wide field AO corrected observations. The stability of the correction for atmospheric turbulence in combination the correction over a few arcminutes provides an ideal combination for investigations that depend on high spatial resolution instruments as well as a large FoV. Therefore, VLT-MAD gives a very promissing impression of the future prospects of observations with upcoming new telescopes and instruments.

The derivation of the MF of Tr 14 revealed a shallow MF that turns over at a characteristic mass of $\sim 0.55\,M_\odot$. The power law slopes of $\gamma \sim -0.6$ show that it is flat in the inner region of the cluster suggesting a deficiency in low mass stars when compared to, e.g., the Kroupa-IMF. Furthermore, no radial variation of the MF has been observed revealing that mass segragation is not present among the stars of intermediate mass.

Chapter 4

The Red SuperGiant Cluster 1

4.1 Introduction

With the recent identification of the massive red supergiant clusters RSGC 1 (age 7-12 Myr, mass 20,000 $M_{\odot}$, Figer et al., 2006), RSGC 2 (age 15-20 Myr, mass 40,000 $M_{\odot}$, Davies et al., 2007; Bica et al., 2003) and RSGC 3 (age 7-12 Myr, mass 20,000 $M_{\odot}$, Alexander et al., 2009; Clark et al., 2009), which are located in the Scutum Crux spiral arm at distances ∼6 kpc from the Sun, and obscured by 10 to 20 mag of visual extinction, the sample of young massive clusters has been extended towards more evolved massive young clusters. Covering ages up to 20 Myr, these red supergiant clusters allow to study PMS in different phases of their evolution and, thus, provide important input for the calibration of stellar evolutionary models. Furthermore, they do not only allow to study stars in the PMS (which lasts ∼20 Myr for a solar-type star) but also MS and post-main sequence evolution. They are found in a rather small area in the Galaxy close to the Galactic plane. The distance of ~ 6 kpc to the sun and their Galactic longitudes between $24^{\circ} < l < 29^{\circ}$ put the RSGCs at a distance of ~ 3.5 kpc from the Galactic Center right at the tip of the Galactic bar and the Scutum Crux Spiral arm (Figure 1.1). This location is, furthermore, connected to the inner boundary of the molecular ring, inherently, since the Galactic bar is mainly responsible for its formation (e.g., Athanassoula, 1992). The RSGC-complex shows similarities to a starburst event at the inner ring of NGC 1097 (Sandstrom et al., 2010). They identified a circumnuclear starburst ring with strong emission in the far-infrared that dominates the far-infrared of the galaxy. The origin might be dust heated by older (> 10 Myr) stars but is still under debate to which a study of the RSGC-complex can offer an important contribution.

In this complex a vigorous star forming event happened between 10 to 20 Myr

ago producing more than $10^5 M_\odot$ in stars. The recent identification of an association of young objects around RSGC 3 has shown, that the entire area can be seen as a giant star formation complex in the Milky Way (Negueruela et al., 2011). Such a complex is unique for the Milky Way, but not an uncommon feature in starburst galaxies. Therefore, it can be considered as a Galactic analogue of extended star forming complexes as observed in starburst galaxies (e.g., Bastian et al., 2005). This makes the RSGC-complex an ideal testbed and template to study massive post-main sequence stellar evolution.

The RSGCs include dozens of red supergiants and are, therefore, of undoubted importance for the study of this class of objects. Spectroscopic and photometric studies have revealed their spectral classes as well as their membership to the different clusters (e.g. Figer et al., 2006; Davies et al., 2007; Alexander et al., 2009; Clark et al., 2009). Due to the recency of the detection of the RSGCs, deep observations are not yet available and required to study their large stellar population across the mass spectrum, from the most massive stars to young, solar mass objects. These populations are particularly interesting for the study of stellar evolution: in fact, these system host simultaneously PMS stars (for the intermediate masses), MS stars, as well as massive stars that evolved off the MS. The large number of members guarantees a numerous population in every mass range, and their coevality allows one to test evolutionary models simultaneously in the three phases of stellar evolution.

Thus far intermediate to low-mass stars have only been studied in starburst clusters with ages in the range 1 to 4 Myr (NYC, Westerlund 1 & 2). In these studies, the comparison with different sets of PMS isochrones has proven extremely useful in age dating intermediate to low-mass populations in NYC (Rochau et al., 2010), Westerlund 1 (Brandner et al., 2008) and Westerlund 2 (Ascenso et al., 2007b).

Based on the identification of 14 red supergiants in RSGC 1 with masses in the range 15-25 $M_\odot$, Figer et al. (2006), assuming a standard Kroupa-IMF, estimated the total cluster mass to be $\sim 20,000\,M_\odot$. NIR observations will enable us to identify cluster members, and test if the assumption of a standard IMF is valid.

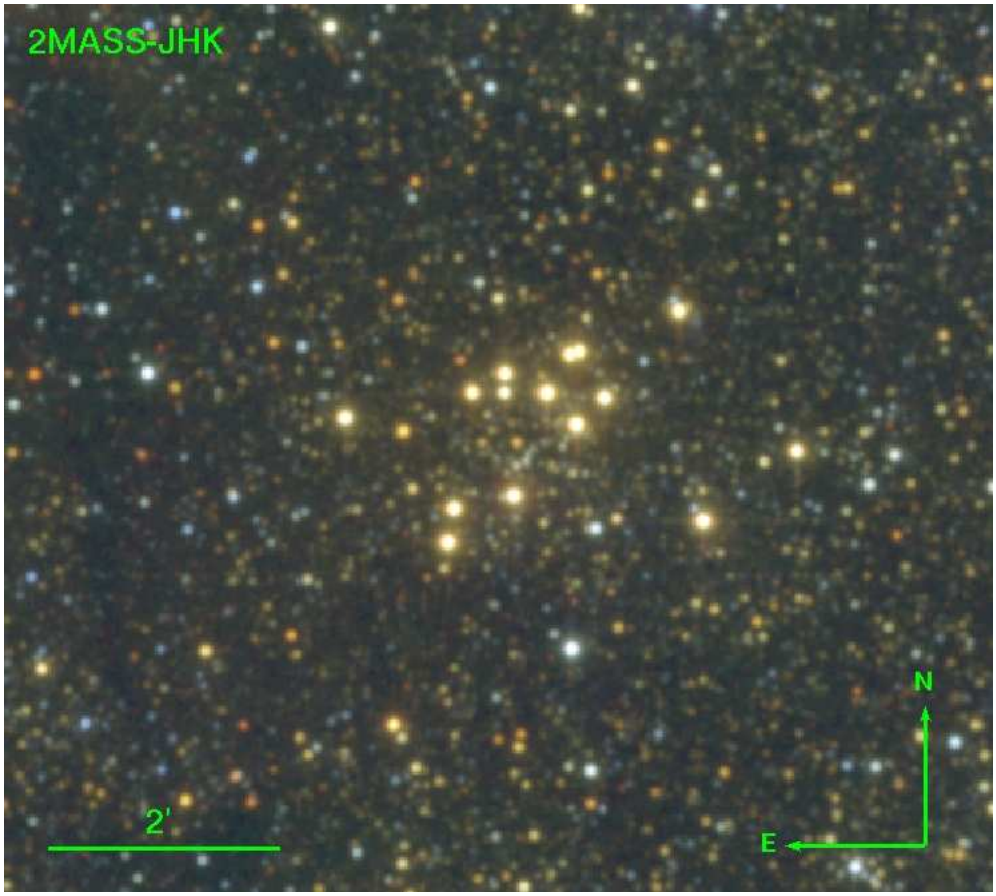

Figure 4.1: RSGC 1 JHK$_S$ composite observed by 2MASS. The red supergiants are clearly visible as the brightest stars in the field.

4.2 RSGC 1 with Omega2000

4.2.1 Data description and analysis

The cluster of red supergiants RSGC 1 is hidden by a visual extinction of $A_V \sim 24.5$ mag and, thus, invisible at optical wavelength. Due to the large amount of foreground extinction and the large angular extension of the cluster near-infrared observations with a large FoV have been inevitable.

The Omega2000 camera mounted on the 3.5m-telescope of the Centro Astronomico Hispano Aleman (CAHA) on Calar Alto provides the required wide-field-, near-infrared- (JHK_S) imaging capabilities under the natural seeing conditions. The $15' \times 15'$ FoV is covered by a Hawaii-2 2048×2048 detector providing a pixel scale of $0.45''$/pixel. We aim at studying a broad stellar census of a cluster with an age between 7 and 12 Myr to map the stellar population beyond the sensitivity and crowding limits of IR surveys such as 2MASS and UKIDSS. Longer exposures and higher angular resolution provide improved photometry to better constrain and discriminate the cluster population from the surrounding Galactic field.

The FoV is sufficiently large such that the entire cluster is covered by a single pointing of Omega2000. Furthermore, the FoV is large enough, compared to the extent of RSGC 1 that we do not need to observe an offset field for the quantification of the contaminating fore- and background population. Adjacent areas are suitable for assessing the contribution of the Galactic field and can be taken from the same pointing.

Total exposure times for the different filters have been chosen to 75 min in J-, 40 min in H- and 32 min in K_S-band to obtain accurate and deep photometry of the cluster and its underlying population. The details of the observations can be found in Table 4.1. Single exposure times compromise between photometric depth and avoiding strong saturation effects. However, due to the presence of bright stars in the field, especially the red supergiants with their K_S-band magnitude of $\sim$ 5–6 mag, saturation effects could not be completely circumvented. We will replace the saturated stars with the existing JHK_S photometry from 2MASS, and relatively long DITs of 60 s in H- and K_S-band and 75 s in J-band are chosen. With the total exposure times in J-, H- and K_S-band we further bridge the gap between the 2MASS photometry and the observations that have been carried out with the Multi-Object InfraRed Camera and Spectrograph (MOIRCS) mounted on the Subaru telesecope (Section 4.3).

Data reduction has been processed using the Omega2000 Data Reduction Pipeline. The bad pixel mask was created from the dark frames which have also been used to build a master dark frame for the corresponding nights. For the K_S-band observations

Table 4.1: Observations with Omega2000

Date	Filter	FoV	$t_{\rm exp}$	$t_{\rm tot}$	sources
01+24/06/10	J	$15' \times 15'$	60×75s	4500s	90136
25/06/10	H	$15' \times 15'$	40×60s	2400s	116847
01/06/10	K_S	$15' \times 15'$	32×60s	1920s	121275

of RSGC 1 the flat field has been obtained from dome flats of the same night. In case of our J- and H-band observations skyflat observations have been carried out and were used to create the mastersky flatfield. Using the science and the calibration frames as input for the Omega2000 Data Reduction Pipeline we obtained fully reduced combined image. The final outputs are shown in Figure 4.2 as a JHK_S color composite.

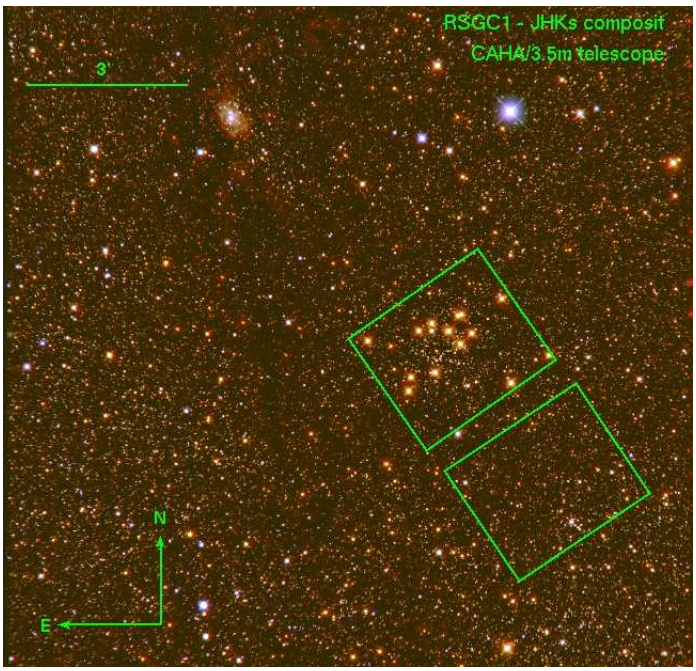

Figure 4.2: RSGC 1 JHK_S composite observed by the Omega2000 at the CAHA 3.5m-telescope. The red supergiants are clearly visible in the right part of the frame. The two green boxes indicate the FoV covered by the MOIRCS observations.

Photometric calibration with 2MASS

We performed PSF photometry on the final images of each band to identify the stars in the field. The best fitting PSFs were found to be a PSF with a Moffat profile in J- and in H-band while for the K_S observations the optimal PSF is comprised of a Gaussian kernel with Lorentzian wings (Penny-function). The final catalogues comprise tenthousands of detections and the results of the photometry process are also summarized in

Table 4.1. To calibrate our photometry, we used a photometric catalogue from 2MASS. Systematic offsets between the 2MASS and Omega2000 photometry allow us to the

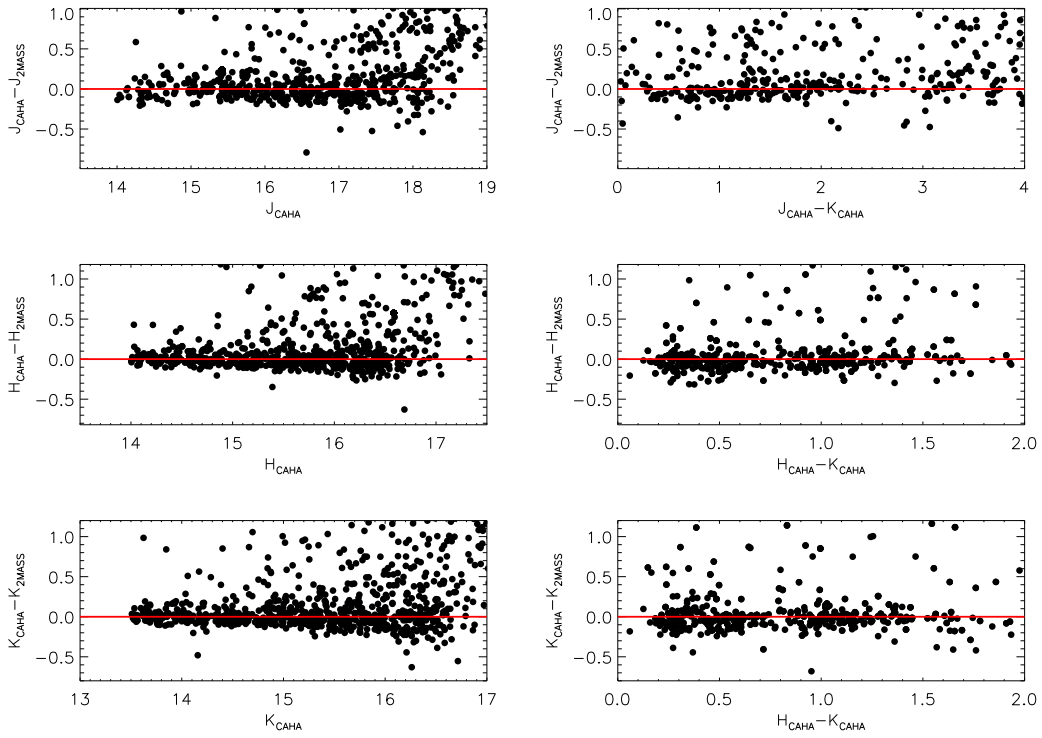

Figure 4.3: Offsets between 2MASS and Omega2000 after applying the ZP correction. In all three filters the the residual offset scatter around zero without showing and variation with magnitude or color.

quantify the photometric ZP offsets. Towards the faintest measured magnitudes we observe largely increasing offsets due to uncertainties in the photometry and such sources have not been considered for the ZP estimation. Bright sources, beyond the linearity regime, were also excluded since they deliver erroneous photometric measurements. Offsets between 2MASS and Omega2000 photometry have been found constant over the considered magnitude range from which we derived the ZP correction. The left panels of Figure 4.3 show the difference between our and the 2MASS photometry as a function of magnitude in the three bands (J-, H- and K_S-band from top to bottom) after applying the ZP correction. Apart from the scatter due to photometric errors, the corrected magnitudes show no systematic variation with stellar magnitude. The right panels Figure 4.3 display again the photometric offsets but as a function of color (J-K_S and H-K_S, respectively) and reveal the absence of color terms, thus, no color correction has to be applied.

4.3 RSGC 1 with MOIRCS

4.3.1 Data description and analysis

As we have seen in the previous section, the combined photometry of 2MASS and Omega2000 allows us to study the stellar population in the area of RSGC 1 down to a limiting magnitude of $K_S \sim 16$ mag. Assuming a cluster at 6 kpc and $A_V \sim 24.5$ mag, this magnitude corresponds to a mass of a MS star of $\sim 4.75\,M_\odot$. To extend the stellar census of RSGC 1 towards lower masses even deeper observations are needed requiring higher angular resolution to avoid crowding effects and higher signal-to-noise ratios through larger collecting areas or longer exposures.

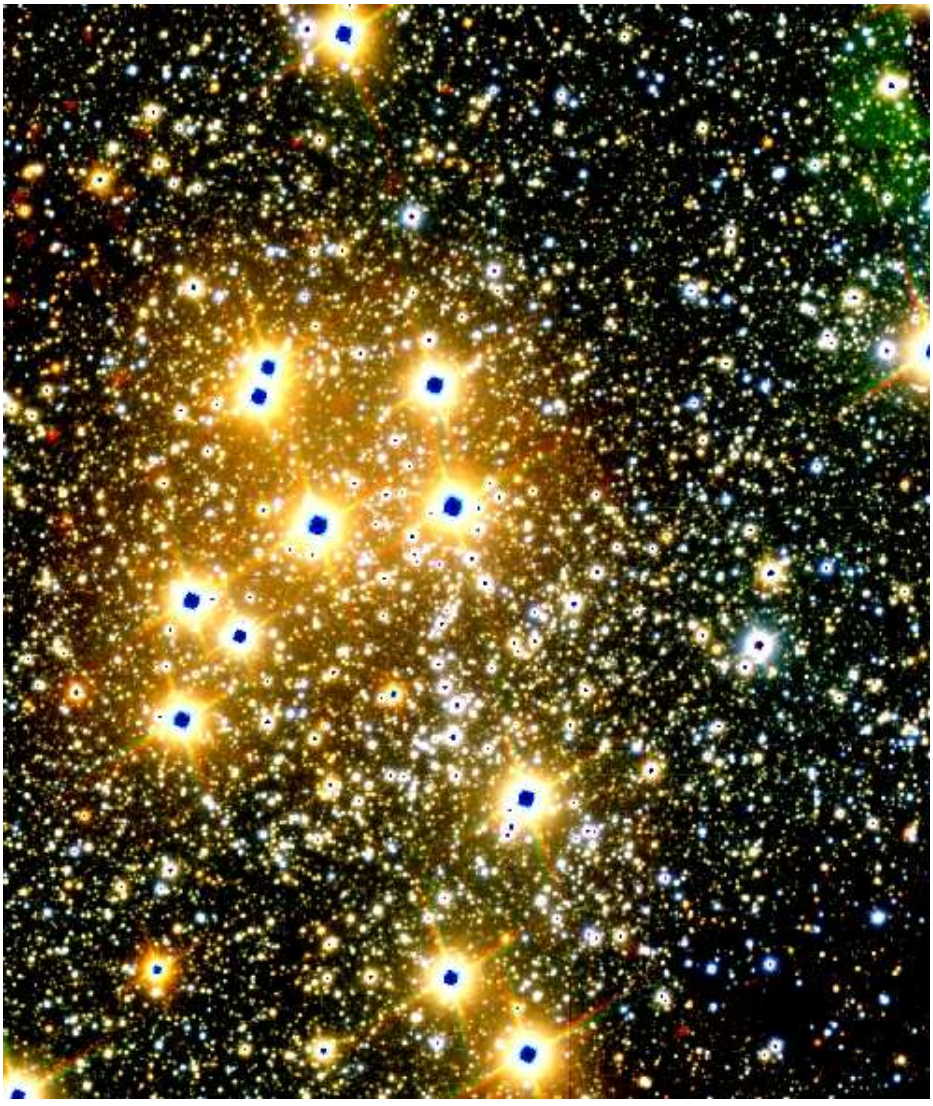

Figure 4.4: RSGC1 JHK_S composite observed by MOIRCS. Clearly visible are the red supergiants in the field as well as the strong saturation in the data.

Table 4.2: Observation with MOIRCS

Date	Filter	Chip	$t_{\rm exp}$	$t_{\rm tot}$(s)	sources
30/07/10	J	Chip1	9×110s	990s	23415
30/07/10	J	Chip2	10×110s	1100s	17960
31/07/10	H	Chip1	8×42s	336s	28279
31/07/10	H	Chip2	7×42s	294s	23184
26/09/10	K_S	Chip1	8×21s	168s	34589
26/09/10	K_S	Chip2	8×21s	168s	34146

To assure photometric depth and accuracy and to extend the stellar census beyond the CAHA observations, we carried out observations using the Subaru Telescope on the summit of Mauna Kea, Hawaii. With its primary mirror of 8.2 m is provides a sufficiently large collecting area for deep observations and MOIRCS provides the required wide-field-, near-infrared- (JHK_S) imaging capabilities under the natural seeing conditions. The $4' \times 7'$ FoV is covered by two Hawaii-2 2048×2048 arrays with the angular resolution of $0.117''$/pixel. The two chips, each covering an area of $4' \times 3.5'$ on the sky, map the region of RSGC 1. The pointing has been chosen such that the center of the cluster falls onto the center of Chip1. The second detector covers an area that is centered $\sim 4'$ away from the center of the cluster and will provide the comparison field for the assessment of the contribution of the Galactic field. At a distance of 6 kpc, $4'$ correspond to a physical distance of ~ 7 pc, sufficiently large to assume no or low contamination from the nearby cluster. The total exposure times for the different filters are ~ 16.5 min in J-band, ~ 5.5 min in H-band and ~ 3 min in K_S-band. Details of the observations can be found in Table 4.2.

For the data reduction, the flatfield was created by I. Tanaka, the support astronomer during the night of the observations. Dark frames where used from the same night. With all available calibration files and the science frames we have processed the data using the data reduction pipeline *MCSRED* created by S. Uchida. The *MCSRED* output is presented as a JHK_S color composite in Figure 4.4. MOIRCS with its $4' \times 7'$ FoV could only provide single exosures with a minimum DIT of 21 seconds. Therefore, the observations suffer from severe saturation, not only for the red supergiants but for sources down to $K_S \sim 14.5$ mag. This is visible as an overdensity of Subaru detections (blue dots) in the K_S vs. H-K_S CMD shown in Figure 4.7 at a magnitude of $K_S \sim 14.5$ and a color of H-$K_S \sim 1$ mag. Smaller DITs could have been achieved by reducing the FoV. Since the accomplishment of the program relies on a large FoV, we had to keep the long DITs.

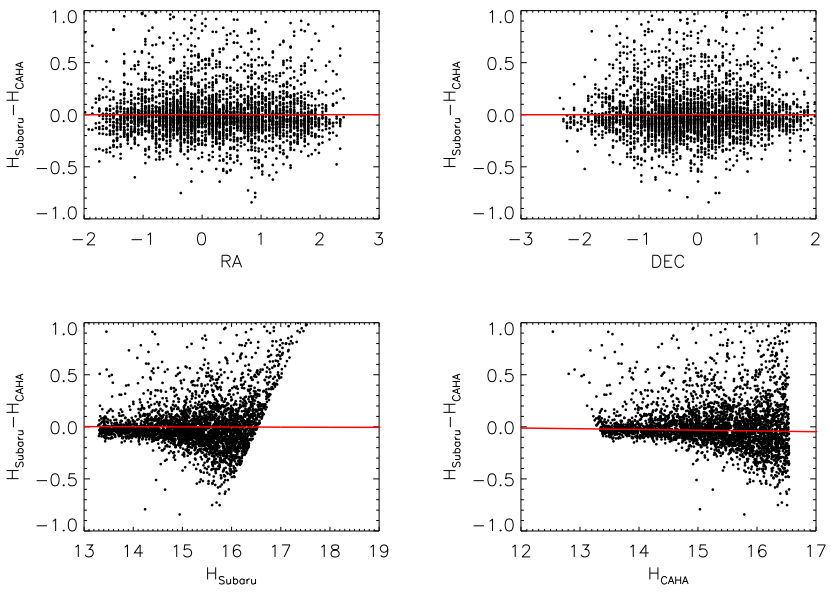

Figure 4.5: Photometric offsets of the MOIRCS photometry of Chip1 after applying the correction as written in the text. Red line show linear fit to the corresponding offset distribution. No systematic offset as a function of right ascension, declination or magnitude is observed.

PSF photometry was performed on the reduced and combined final images of each band. We found a Penny function to be the best representative PSF for our observation in J-, H- and K_S-band as well as in both chips. It was further chosen to be spatially variable to the second order over the field. Details of the observations are summarized together with the outcome of the photometry and can be found in Table 4.2. Due to the large minimum exposure time of 21 seconds and the subsequent severe saturation the detection of bright sources with counterparts in the 2MASS catalogue are inhibited; all 2MASS sources are saturated in our science frames. Therefore, we use the calibrated photometry of the Omega2000 observations that provides significant overlap to calibrate our MOIRCS photometry into the 2MASS system. Comparison of the catalogues reveal a linearly decreasing offset with decreasing stellar brightness. A linear fit to the offset distribution is accounted for this dependence. A similar correction was applied to the residual offset as a function of right ascension and declination. An example (H-band) for residual offsets after the final calibration for both chips are plotted in Figure 4.5 and 4.6, respectively. Corresponding fits (superimposed as red lines) reveal the absence of further systematic offsets. Also color terms are not observed, thus, applying the described procedure to our photometry provides a sufficient calibration.

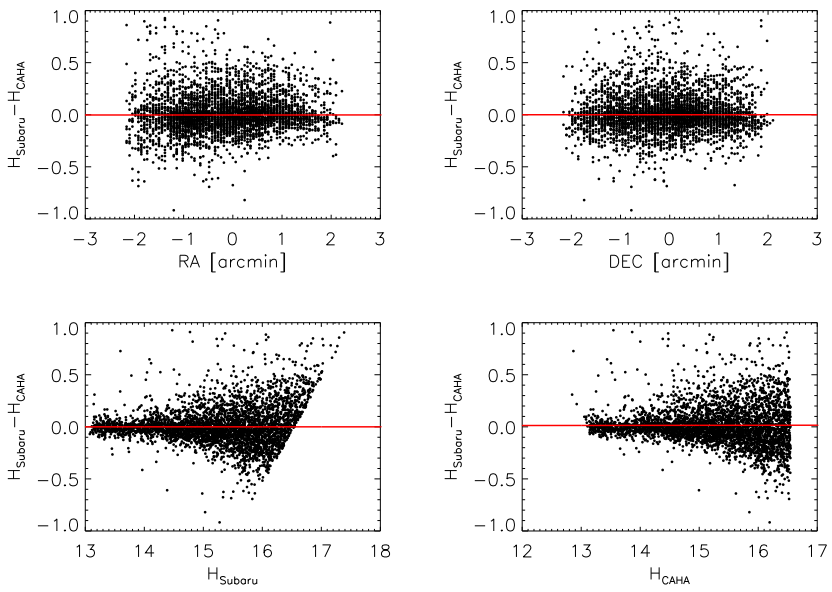

Figure 4.6: The same diagram as Figure 4.5 but for Chip2. Again, no systematic offset as a function of right ascension, declination or magnitude is detected.

4.3.2 Catalogue combination

A K_S vs H-K_S CMD of all detected sources is shown in Figure 4.7. It includes also sources with high photometric uncertainties as well as sources suffering from non-linearity or saturation of the detector. It provides another visual inspection of the goodness of the calibration and reveals the great dynamic range of almost 15 magnitudes. The red supergiant population of the cluster is visible as the group of stars with K_S-band magnitudes between 5 and 6 mag in the cluster CMD. It further depicts the strong saturation that is observed in the MOIRCS data visible as the concentration of stars at $K_S \sim 14.5$ mag and H-$K_S \sim 1$ mag (blue dots). The improved quality of the photometry comparing Omega2000 and MOIRCS becomes apparent as the increasing scatter of Omega2000 sources (black dots) below $K_S \sim 16$ mag, while the MOIRCS observations still describes a relatively narrow distribution.

To obtain a final combined photometric catalogue of the region, we selected magnitude intervals according to the photometric uncertainties. Uncovered areas in the color-magnitude plane, due to simple magnitude cuts, were filled with stars from the next shallower catalogue fulfilling the corresponding magnitude and color constraints. Applied magnitude cuts between the different catalogues are displayed as vertical lines in Figure 4.8.

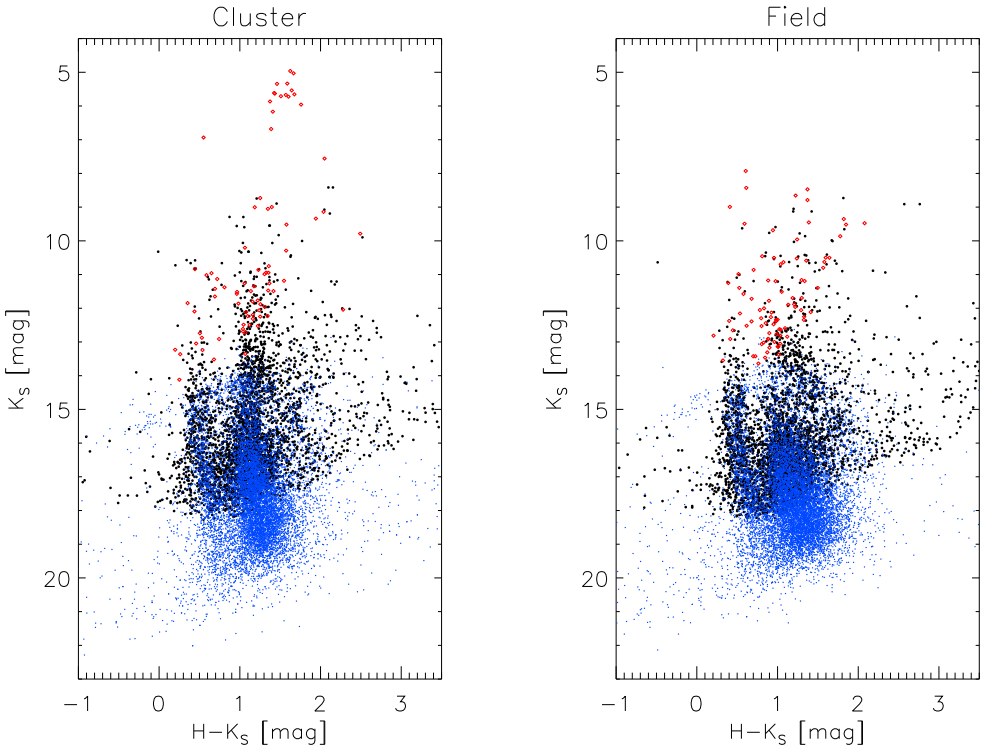

Figure 4.7: K_S vs. H-K_S CMD of all sources detected with 2MASS, Omega2000 and MOIRCS in the MOIRCS-FoV. 2MASS sources are shown as red diamonds, stars detected with Omega2000 are shown as black dots. Blue dots correspond to the photmetric catalogue of the MOIRCS observations.

4.4 Structure of RSGC 1

The large area covered by the MOIRCS observations allows us to construct the stellar surface density profile of RSGC 1 to derive structural properties of the cluster. To obtain the density profile we divide the observed field into concentric annuli around the center of the cluster. We then determine the completeness-corrected number of stars in each annulus and normalize this to the considered area. To locate the center of the cluster we considered only stars that are brighter than $K_S = 15$ mag, since the contamination of the Galactic field for $K_S < 15$ mag is significantly lower (see Figure 4.7). A map of the reduced photometric catalogue is shown in the left panel of Figure 4.10. From this catalogue we derived the local stellar density by finding the 10 nearest neighbors to each star. The distance d_{Nth} to the outermost star defines the density via $\rho_{stars} = \frac{\mathrm{N}}{A_\mathrm{N}}$, where N is the number of considered nearest neighbors and $A_\mathrm{N} = \pi \times d_{Nth}^2$ describes the area covered by the N+1 stars. A smoothed map of the resulting density distribution is shown in the right panel of Figure 4.10. The cluster can be identified in the northern area as excess density around the major peak. It must be noted, however, that the

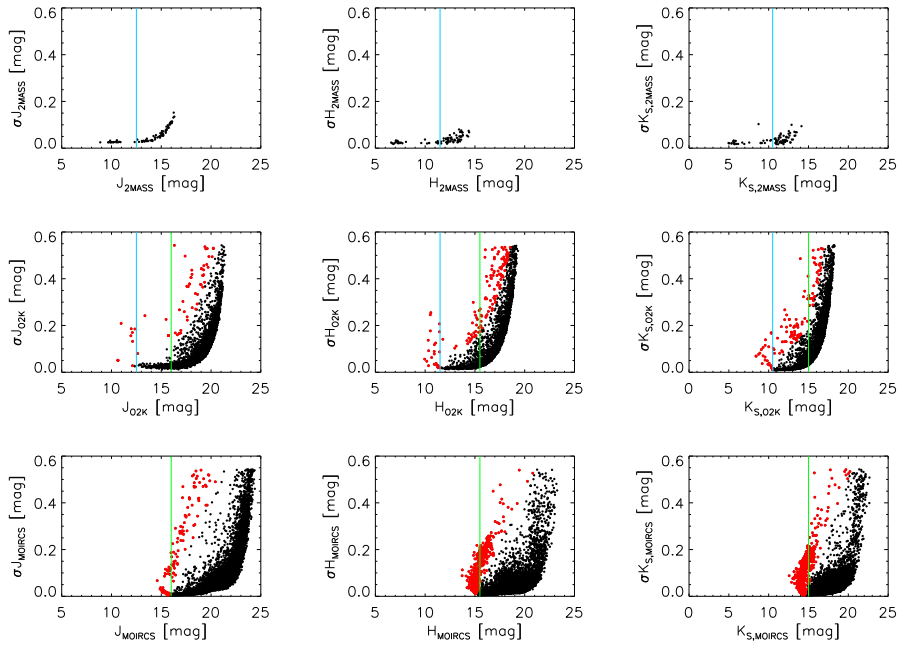

Figure 4.8: DAOPHOT photometric uncertainties for the J- (left panels), H- (central panels) and K_S-band (right panels) for the stars detected by 2MASS (upper panels), Omega2000 (middle panels) and MOIRCS (bottom panels). The vertical lines display the magnitude levels and intervals of the corresponding photometric catalogue that have been considered to create the final photometric catalogue. Red dots display the stars that have been excluded from the catalogue.

apparent concentric decrease of stellar density around the peak does not reflect the real shape of the cluster, because the presence of the red supergiants significantly reduces the completeness towards the west (see also Figure 4.17). Despite the high incompleteness, we can identify the outskirts of the core of RSGC 1 as enhancements of the density compared to the background level. Interestingly, these appear elliptical in shape. In order to estimate the degree of elongation and to assess the center of the cluster we fitted an ellipse to the outer region of the core. The best-fitting ellipse (purple ellipse), as well as its center (purple diamond), are overplotted to the source map and the surface density map in Figure 4.10. The center of the ellipse is found off the maximum peak density, and the resulting center at $\alpha = 18^h37^m57^s$ and $\delta = -06°52'47''$ has been used for the following analysis.

We measure an eccentricity of $\epsilon = 0.685$ and the major axis is inclined by $\sim 20.6°$ with respect to the Galactic plane. A similar elongation has been observed in Westerlund 1 (Gennaro et al., 2011). One possible solution is that Westerlund 1 is a merger product, while internal dynamics and differential Galactic rotation could be excluded as possible reason. A clear answer on the origin of the nature of the elongation is not straightforward. However, the similarities between Westerlund 1 and RSGC 1 in terms

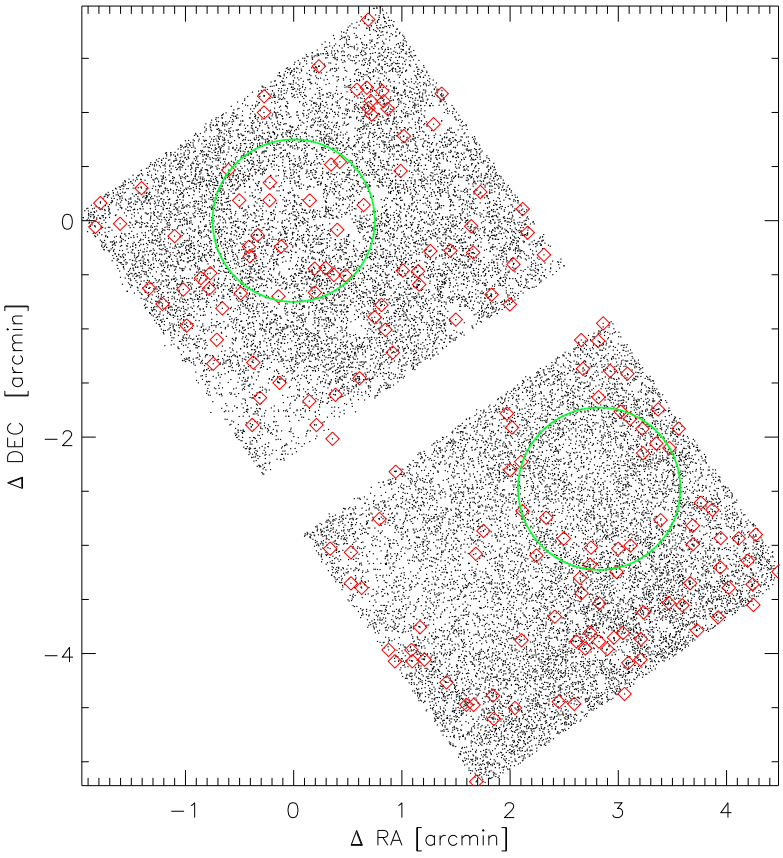

Figure 4.9: Stellar sources detected by 2MASS, Omega2000 and MOIRCS. The core of RSGC 1 is located in the upper area with its center being the center of the green circle. The circle has a radius corresponding to the core radius of RSGC 1. The green circle in the lower area displayes the field that has been chosen as the offset field. Red diamonds highlight the bright stars in the field detected by 2MASS.

of in mass, extend and distance to the Galactic center as well as the elongation are intriguing.

As the center of the cluster has been estimated, we divided the observed area into concentric annuli with a 15″ width. Stars are counted within each annulus and corrected with the corresponding incompleteness factor $c_i = c_{i,H} \cdot c_{i,\mathrm{K_S}}$, such that the completeness-corrected number of stars in annulus i becomes $N_{i,c} = \sum_* \frac{1}{c_*}$. Normalizing to the considered area A_i yields the stellar surface density $f_i = N_{i,c}/A_i$ which is shown in Figure 4.11. Error bars correspond to Poisson statistics. The density profile shows a steep decrease towards the outer regions of the cluster. The low density in the very center of the cluster is due to the high incompleteness induced by crowding and the bright stars in the center. The stellar surface density drops to a minimum at $\sim 3.5'$ distance. Further away it increases again for reasons: On one hand we have identified

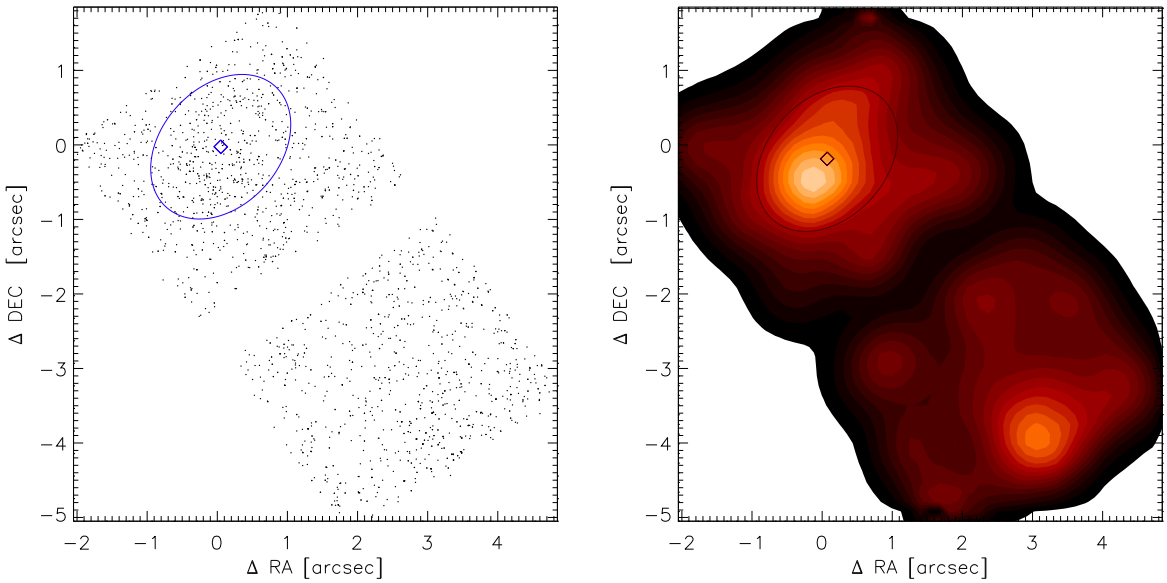

Figure 4.10: *Left panel:* Stellar sources from our photometric catalogue that have been detected in 2MASS or in our Omega2000 observations. *Right panel:* Smoothed map of the stellar surface density. The core of the cluster can be identified as the excess in stellar density in the northern part. The best-fitting ellipse to the density distribution and its center are shown as a purple ellipse and diamond, respectively.

a second peak in the stellar density map being located in the south of the offset field (Figure 4.10). On the other hand, the entire region exhibits patches of interstellar matter leading to variable extinction in the area. For instance, the eastern edge of the FoV exhibits a lower stellar density which can be related to a higher extinction which can be seen in both the JHK$_S$ color composite and the density map as low density regions and in the completeness map as regions of relatively high completeness.

4.4.1 Structural parameters

To derive structural parameters of RSGC 1, we applied an empirical model introduced by Elson et al. (1987) (from here on EFF) to the stellar surface density profile of the cluster. The EFF model has been applied primarily to clusters in the LMC and describes clusters without tidal truncation. It provides the opportunity to accurately derive the core radius, the central stellar density and the steepness of the profile. The core radius (r_c) is the distance from the center of the cluster at which the stellar density drops to half of its central value. The EFF profile is a power law and written as:

$$f(r) = f_0(1 + r^2/a^2)^{-\gamma/2} + f_{\rm field} \tag{4.1}$$

where f_0 is the central stellar surface density, a is a measure of the core radius and γ is the power-law slope, which describes the decreasing surface density of the cluster at large radii ($f(r) \propto r^{-\gamma}$ for $r \gg a$). The background field contribution is assumed to be constant over the field and estimated by $f_{\rm field}$. We fit the EFF profile in order to estimate the core radius together with a uniform background level. As the increasing stellar density in the outer regions is primarily due to differences in the extinction pattern, the density measured beyond $r = 4.25'$ has not been considered during the fit.

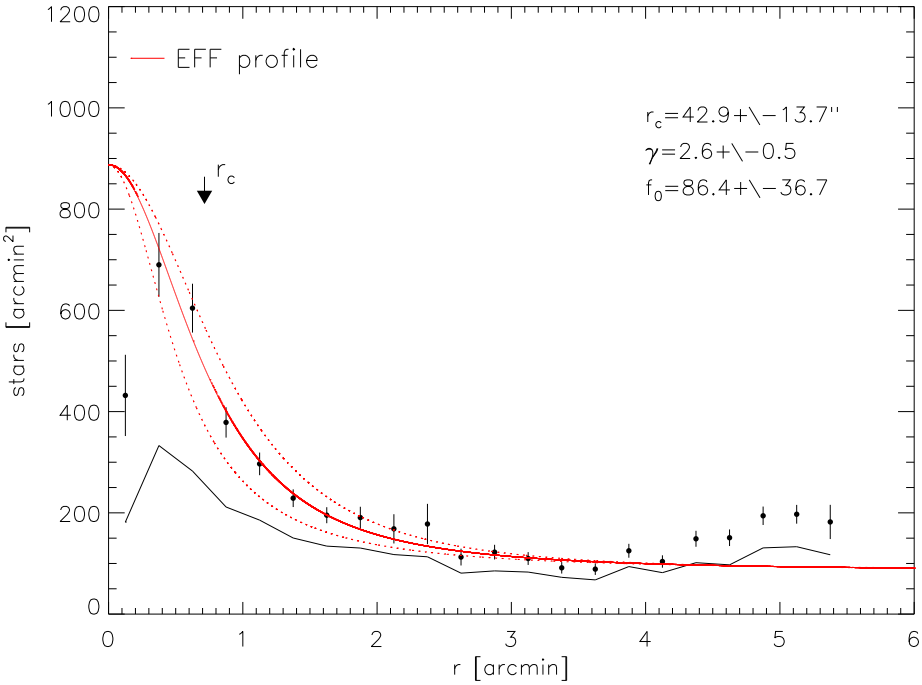

Figure 4.11: Surface density profile of the reduced catalogue. Stars are counted in annuli with 15″ width around the center of the cluster. The completeness-corrected density profile is well approximated by a EFF profile with a core radius of 42″ and a slope of $\gamma = 2.6$.

The best-fitting EFF profile is overplotted to the surface density profile of RSGC 1 as a straight red line in Figure 4.11. It reveals a power law slope of $\gamma = 2.6 \pm 0.5$ and a measure for the core radius of $a = 50.9 \pm 16.2''$. The field contribution to the surface density was estimated to be $f_{\rm field} \sim 86.4 \pm 36.7$ stars/$arcmin^2$. The parameter a can be related to the core radius via $r_{\rm c} = a(2^{2/\gamma} - 1)^{1/2}$ according to the EFF model, following (Elson et al., 1987). With $a = 50.9 \pm 16.2''$ we obtain a core radius of $r_c = 42.9 \pm 13.7''$. At a distance of 6 kpc, this corresponds to be 1.3 ± 0.4 pc.

4.5 Identification of the cluster population and its photometric study

4.5.1 Color magnitude diagram

The derivation of the core radius allows us to select a region with a high fraction of cluster members. We construct two K_S vs J-K_S CMDs of stars within one core radius centered on the cluster. An area of the same size has been selected in Chip2 as representative for the field contamination (green circles in Figure 4.7).

To isolate the cluster population from the contaminating field several approaches are possible. We used high-precision astrometric measurements to discriminate cluster stars from field stars in Chapter 2, and the different locations of cluster and field in the CMD in Chapter 3. Here we are using a statistical approach (introduced by Gennaro et al., 2011)) to subtract the contaminating field. In the following text we will briefly describe the technique applied. For a detailed description of the method we refer to Gennaro et al. (2011).

A standard subtraction method to clean a CMD from the contaminating field is gridding the CMD of the cluster region and the offset field (e.g., Rochau et al., 2007). Comparing detected sources of two corresponding grid elements deliver an estimate for the contamination. However, different photometric uncertainties and completeness introduce biases in the subtraction. Therefore, Gennaro et al. (2011) introduced a new method to assess the contaminating field population by considering photometric uncertainties. Instead of counting stars in a bin in the CMD, the density distribution in a magnitude-magnitude diagram is calculated. The local density was derived considering the completeness as well as photometric uncertainty, according to Equation 1 from Gennaro et al. (2011). Photometric uncertainties are taken into account as the position of a star in the magnitude-magnitude diagram is represented by an ellipsoidal probability distribution with the photometric uncertainties as the semi-major and semi-minor axes. Comparison of the densities in the cluster and the offset field yield a rejection probability (Gennaro et al., 2011). To clean our CMD from the field contamination, we exclude each star with a rejection probability higher than 20%. The resulting CMD is shown in Figure 4.12 The cleaned CMD shows the MS population of RSGC 1, which is identified at J-$K_S \sim 3.5$ mag. However, we also detect residual foreground stars blueward of the MS, which are clearly separated from the MS of the cluster. The blue isochrones in the right panel of Figure 4.12 are 2σ off the fiducial line to isolate the cluster population from residual field stars. The sample within 2σ is later used to derive the core mass function of RSGC 1.

Figure 4.13 shows the color-color diagram of the photometric catalogue with the probable cluster member highlighted as red dots. The red supergiant red visible in the upper right corner nicely separated from the MS population. The contaminating foreground population can be seen as the group of stars in the lower left corner. The color-color diagram display only few red sources, so few stars showing IR excess.

The clean MS and group of red supergiants allows us to compare the CMD with stellar evolutionary models. We applied MS isochrones the Geneva group (Schaller et al., 1992; Meynet et al., 1994) to estimate the age and reddening of RSGC 1. The extinction can be measured by the near-infrared colors of the MS, and the age can be assessed by comparing the isochrones with the group of red supergiants. The isochrone that best resembles the observed CMD is overplotted. With solar metallicity, it confirms an age of 10 ± 1 Myr, and locates the cluster at a distance of 6 kpc.

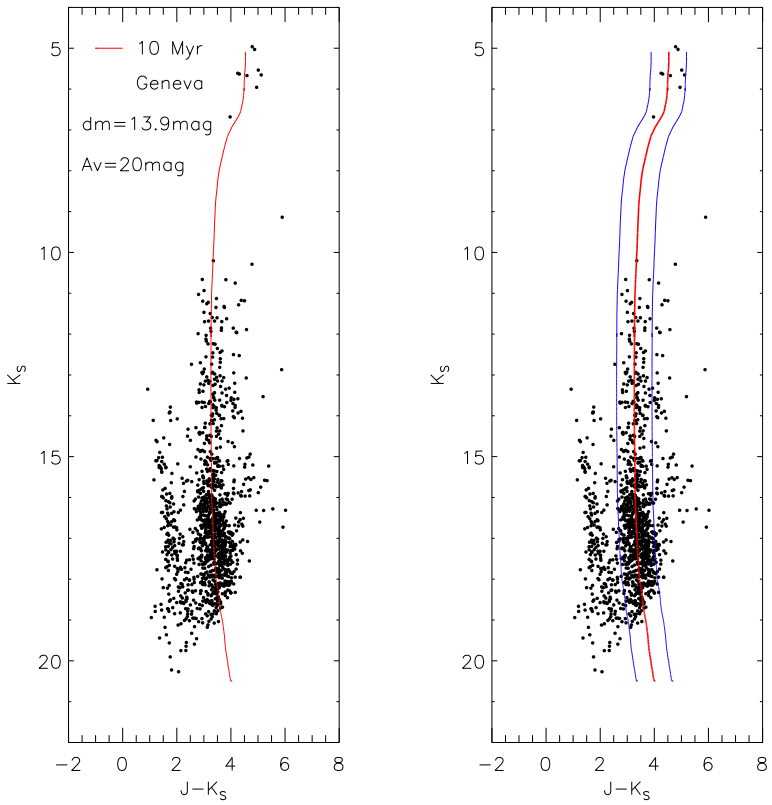

Figure 4.12: K_S, J-K_SCMDs. Black dots show the stars that are considered as cluster member candidates due to a low rejection probability of < 0.2. Overplotted Geneva tracks isochrones reveal an age of 10 ± 1 Myr with a visual extinction if $A_V = 20$ mag (red lines) and a distance of 6 kpc to the cluster. The remaining field population has been excluded by selecting only stars that are within two standard deviations around the fiducial line (blue lines).

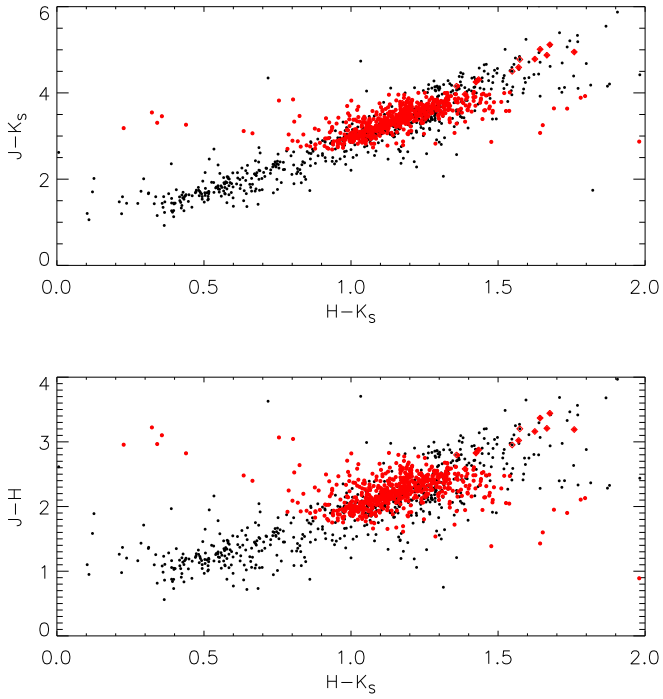

Figure 4.13: J-K$_S$, H-K$_S$ and J-H, H-K$_S$ color-color diagrams of RSGC 1. Small black dots display all sources with a rejection probability of < 0.2. Red dots show the detected cluster members candidates (see Figure 4.12), while the bright sources (red diamonds) have been taken from 2MASS. The diagram shows an absence of a population of excess sources.

4.5.2 Blue to red supergiant ratio

RSGC 1 with its extended population of red supergiants provides the ideal environment to study the post main sequence evolution of massive stars. Key information for the calibration of post-main sequence models is the ratio of blue to red supergiant in a stellar cluster. It provides important input to the development of stellar models and has been observed to depend on metallicity with a lower metallicity, leading to a higher B-R ratio (Meynet et al., 2011).

In RSGC 1 14 RSGs have been identified spectroscopically (Figer et al., 2006). In order to derive the B-R ratio, we estimate the number of BSGs from our observations. In near infrared observations the MS appears as a vertical sequence in the CMD and the BSG phase extends the MS towards higher magnitudes: colors (H-K$_S$ as well as J-K$_S$) remain at comparable levels. Consequently, in the K$_S$ vs. J-K$_S$ CMD of RSGC 1 (Figure 4.12) the transition from the MS stars to the blue supergiants (BSG) has almost no change in color, making the identification is challenging.

To identify the starting point of the BSG phase we used the Padova and Geneva

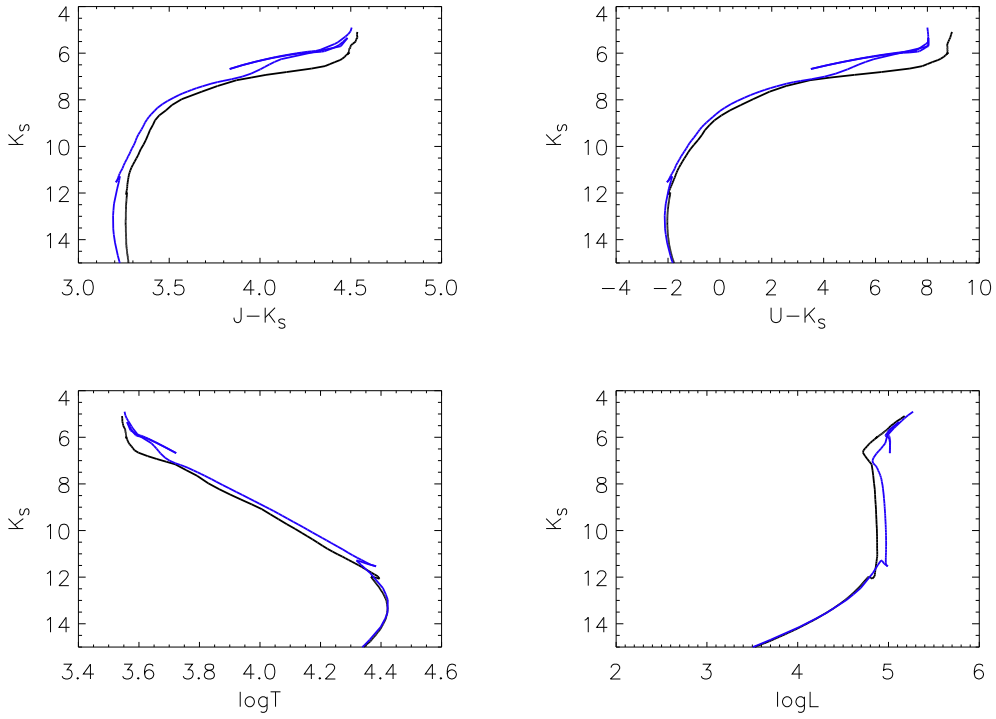

Figure 4.14: *Upper left panel:* Isochrones from Padova (blue line) and Geneva (black line) in a K_S vs. J-K_S CMD. *Upper right panel:* The same tracks, but in a K_S vs. U-K_S CMD. *Lower left panel:* The apparent K_S magnitude for RSGC 1 as a function of effective temperature. As the star expands it cools down and the tracks move to lower temperatures for $K_S < 12$ mag. *Lower right panel:* Apparent steep increase of the K_S band magnitude at constant stellar luminosoty as it enters the BSG phase.

isochrones that best represent the cluster population. Figure 4.14 shows four panels with relations of the K_S to the J-K_S and U-K_S colors as well as to the effective temperature and luminosity of the star. To derive the apparent magnitude K_S, we applied the derived distance and extinction. The RSG position is located close to the tip of each isochrone, but the BSG starting point is difficult to identify.

As a star enters the BSG phase it cools down significantly as it expands. This can be identified with a decreasing temperature, and an increasing apparent brightness in the infrared, while the luminosity remains relatively constant. The increasing K_S-band brightness is connected to the increasing radius of the star and describes the starting point of the BSG phase. We identified the starting point at $K_S = 11.5$ mag and logT $= 4.4$. Due to uncertainties in the distance measure, photometry as well as through differential extinction we assumed $K_S = 12$ mag as the limiting magnitude for the BSG phase. This is shown as the blue dotted line in Figure 4.15. With this simplistic approach we identified 36 ± 5 stars fullfilling these constraints. With the

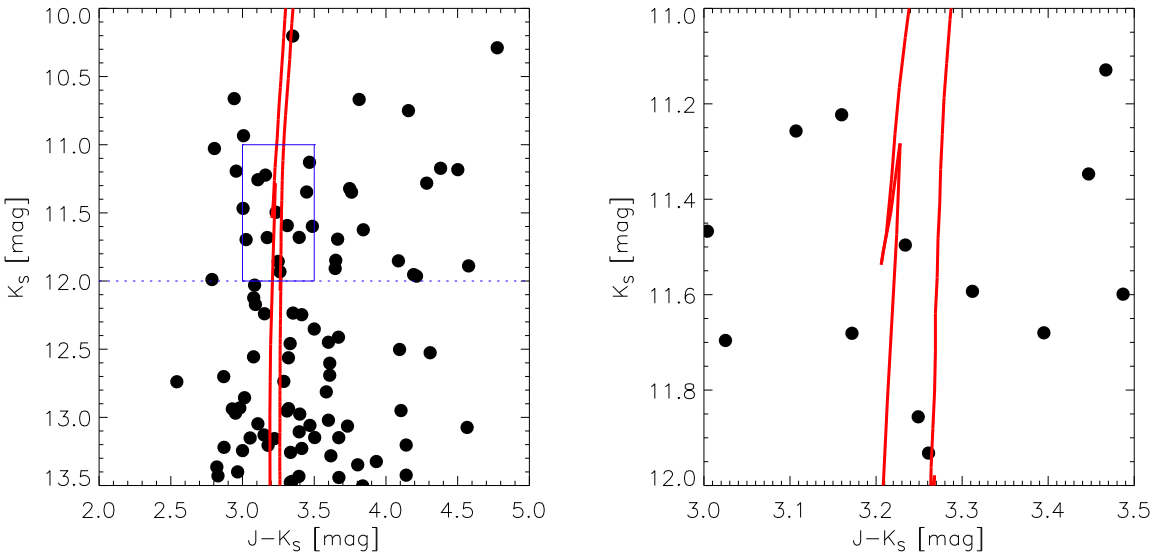

Figure 4.15: *Left panel:* Zoom-in to the region of the CMD in which the BSG starting point was detected. Dotted line enclose the area that has been considered as the BSG region. The blue box is magnified in the right panel. Right panel: Zoom-in onto the starting point of the BSG phase.

spectroscopically confirmed 14 RSGs in the cluster, we obtain a B-R ratio of $B/R = \frac{36\pm5}{14} \sim 2.6 \pm 0.4$. This is close to the B-R ratio of 3.21 that has been derived by Figer et al. (2006). Due to our lowered magnitude constraints we consider it this ratio as an upper limit for the B-R ratio. However, comparing this finding with Figure 1 of Eggenberger et al. (2002) showed that a value of 2.6 yields a solar metallicity in agreement with our applied isochrone.

4.6 Mass function of the RSGC 1

Completeness

As mentioned in Section 2.6.1, we require accurate knowledge of the completeness function to derive the MF of a stellar cluster. In dense stellar fields the effect of crowding and faintness limits a source' detectability. The associated completeness depends, therefore, on the position of the star in the field and its magnitude. To derive the completeness function, we added artificial stars to the science frame and re-processed the photometry. We recall the Equation 2.13 decribing the completeness as a function of position on the detector and magnitude of the star:

$$C_j(x, y, \mu) = \frac{\alpha(x, y)}{exp\frac{\mu-\beta(x,y)}{\gamma(x,y)} + 1}. \tag{4.2}$$

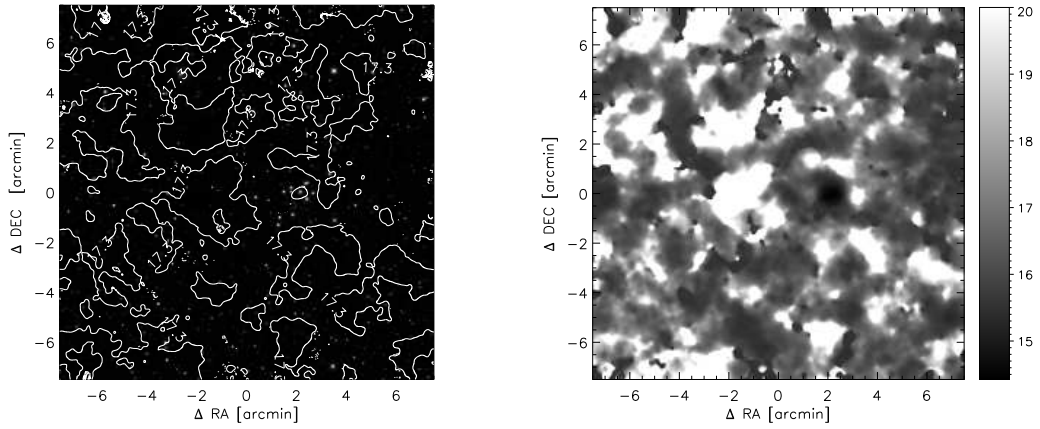

Figure 4.16: *Left Panel:* K_S-band image of RSGC 1 as observed with Omega2000. The 50%-completeness limits are overplotted as white contours. *Right Panel:* K_S-band completeness map of the entire observed FoV. The grey shades correspond to the K_S-band magnitude at which a completeness of 50% is achieved.

Omega2000: In case of the Omega2000, we added a total of 5,000 added artificial stars to our image in each photometric bin of 0.5 mag width. The typical separation between the simulated stars is, therefore: $d_{sim} \sim 34$ pixel. The left panel of Figure 4.16 shows the K_S-band image of the Omega2000 observations with white contours displaying different magnitudes at which 50% completeness limits is reached. The right panel depicts the 50% completeness map as a function of magnitude. The region of RSGC 1 is visible as the area depicting the lowest completeness and thus the brightest limiting magnitudes.

MOIRCS: For the MOIRCS observation we included 5,000 artificial stars in each photometric bin of 0.5 mag width. 100 iteration were used again to maintain the crowding characteristics. For MOIRCS we obtain a typical separation between the simulated stars of $d_{sim} \sim 34$ pixel. The left panel of Figure 4.17 shows the K_S-band images of the two MOIRCS chips with 50% completeness levels overplotted as white contours. The cluster can be identified in the right panel (completeness map), the positions of the RSGs are prominent with high incompleteness value in the proximity.

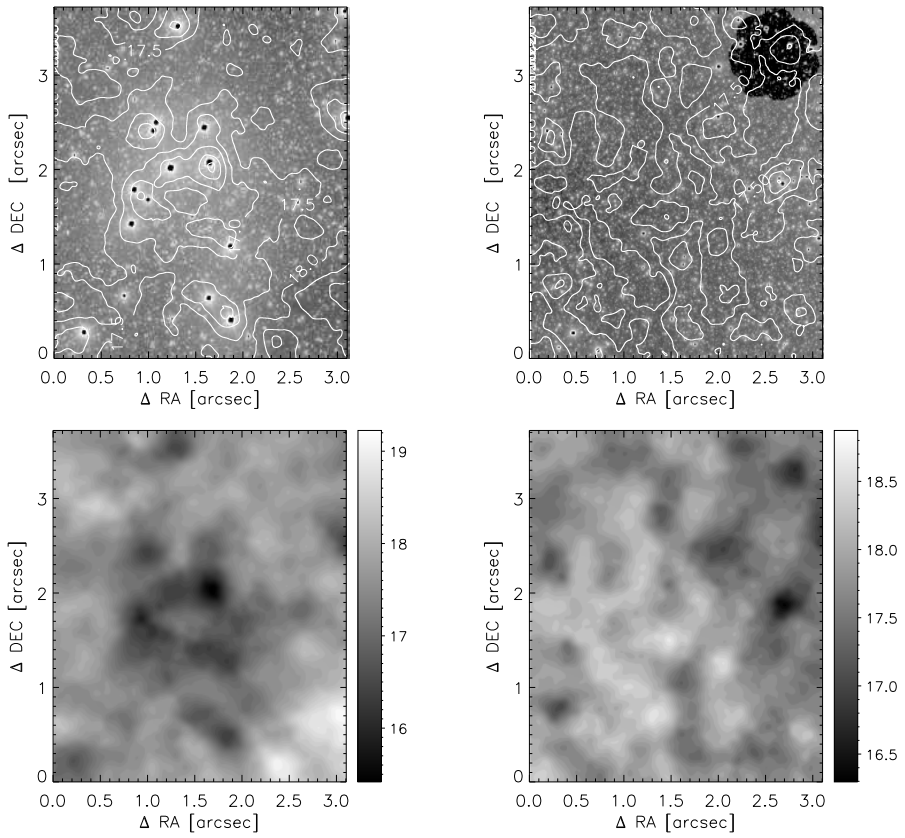

Figure 4.17: *Left Panel:* K_S-band image of RSGC 1 as observed with MOIRCS. The 50%-completeness limits are overplotted as white contours and cover a magnitude range between 16 mag< K_S <19 mag. *Right Panel:* K_S-band completeness map of the entire observed FoV. The grey shades correspond to the K-band magnitude at which a completeness of 50% is achieved.

4.6.1 Mass-luminosity relation

To ascribe masses to single stars we derived the MLR using the 10 Myr MS Geneva isochrone (Schaller et al., 1992; Meynet et al., 1994). Present mass and the absolute magnitude are given by the stellar models and considering the derived values for distance and extinction we obtain the MLR for RSGC 1. It is shown in Figure 4.18

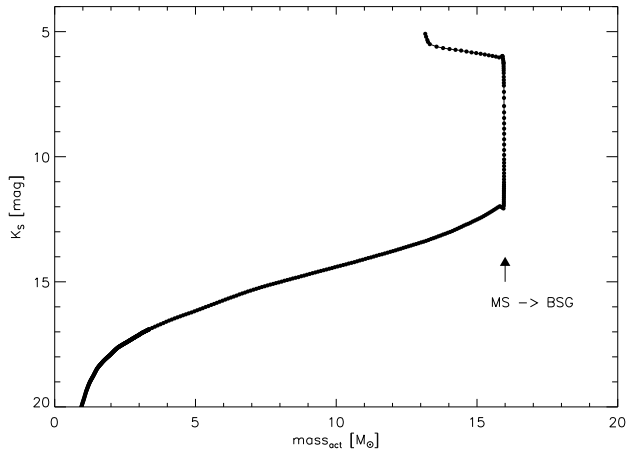

Figure 4.18: Mass luminosity relation of the applied 10 Myr Geneva isochrone. The steep increase as 15 $M_\odot$ describes the supergiant phase. For the derivation of the stellar masses, this region has not been considered. The arrow highlights the starting point of the BSG phase.

illustrating the apparent K_S magnitude as a function of stellar mass. The MLR has been used to derive stellar masses for each star.

For the MS we see an almost linear depence of the apparent magnitude from the mass for stars up to 15 $rmM_\odot$. As the core hydrogen burning ceases the star evolves of the MS. Towards substellar masses represented by the steep decline in stellar brightness with decreasing stellar mass (Figure 4.18). The bulk of the PMS, with masses between 2 $M_\odot$ and $\sim$ 15$M_\odot$, shows a almost linear relation between stellar brightness and mass.

4.6.2 Mass function

We used the MLR to derive stellar masses and, subsequently, the PDMF $N(\log \mathrm{m})$ of RSGC 1 with its power law slope $\gamma = \frac{d \log N(\log \mathrm{m})}{d \log \mathrm{m}}$, We followed again the method presented by Maíz Apellániz & Úbeda (2005) creating bins with just a single star. The completeness-corrected PDMF of RSGC 1 is presented in Figure 4.19 for masses between 5 and 15 $M_\odot$. The best-fitting power law is overplotted. The PDMF appears shallow when compared to a Salpeter-IMF. However, the derived power law slope of $\gamma = -0.86 \pm 0.12$ agrees well with the values we obtained from the mass functions of NYC and Tr 14.

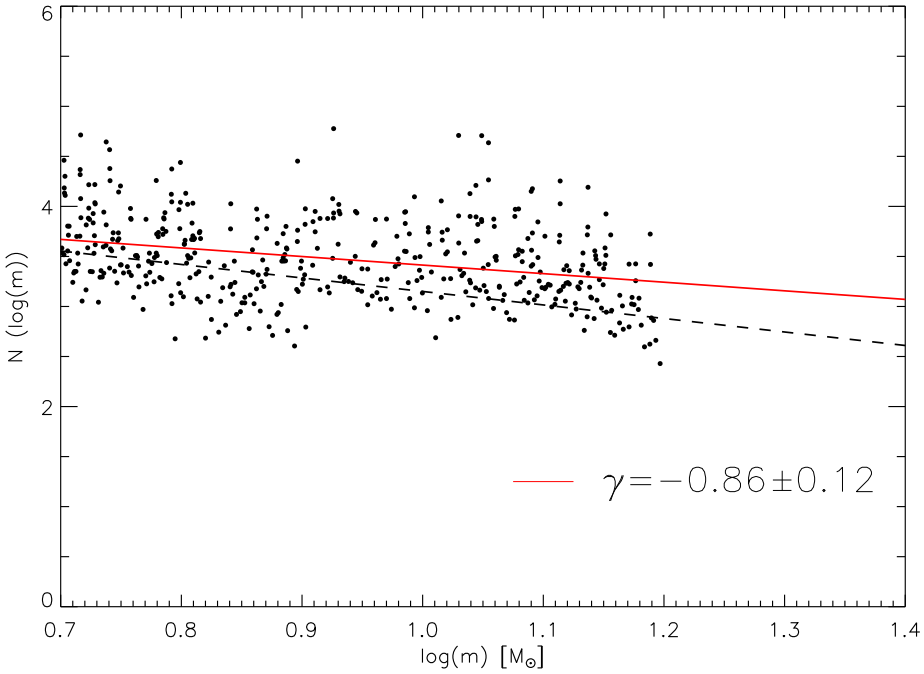

Figure 4.19: Mass function of RSGC 1 derived following the suggested method of Maíz Apellániz & Úbeda (2005). Each 'bin' contains a single star, which has been corrected for incompleteness and was divided by the width of the bin. We derived a reliable PDMF down to $0.5 M_{\odot}$ and up to $\lesssim 15 M_{\odot}$. The red supergiants have been excluded due to their similar masses during the red supergiant phase and the great uncertainties in the post-main sequence evolution and the subsequent mass loss events. The best fit to the PDMFs is overplotted as a straight red line and has a power law slope of $\gamma = -0.86 \pm 0.12$. This agrees within the errors with the power law slopes, that we have measured in NYC and Tr 14 and slightly shallower than the Salpeter-IMF (dashed line).

4.7 Summary

We have analysed JHK$_S$ photometry of the recently detected massive red supergiant cluster RSGC 1. The data has been obtained from 2MASS, Omega2000 and Subaru-MOIRCS. The covered FoV allowed the construction of the surface density profile. Fitting an EFF profile to the stellar surface density resulted in a measurement of the core radius of RSGC 1, which was found to be 1.3 ± 0.4 pc. We further identified elongation of the cluster with an eccentricity of $\epsilon = 0.685$. The major axis is inclined by $\sim 20.6^\circ$ with respect to the Galactic plane. The nature of such elongation is still uncertain. We constructed the CMD of the cluster and applied isochrones to the observed MS population. We could estimate the age to be 10 ± 1 Myr and the extinction to $A_V = 20\,mag$. The cluster is located at a distance of 6 kpc. Within the core radius we have derived the core MF. Its slope of the MF was found to $\gamma = -0.86 \pm 0.12$ which is shallower than the Salpeter-IMF and agrees well with the derived slopes for NYC and Tr 14.

Chapter 5

Summary and conclusion

This thesis illustrates the importance of young massive clusters as probes for stellar and dynamical evolution. Comprising stars over the entire mass range, they offer ideal laboratories to investigate the evolution of PMS and MS stars and massive post-main sequence stars.

Stellar evolution: The astrometric study of the cluster NYC in the Carina spiral arm revealed new insights into the dynamics of this young and massive spiral arm cluster. The accurate proper motion measurements of 829 stars, based on two epochs of *HST*-WFPC2 observations separated by 10.15 yr, represent a powerful tool to discriminate cluster stars from the contaminating Galactic field. Derived membership probabilities and the subsequent selection of candidate cluster members ($P_{\rm mem} > 0.9$) result in a clean cluster CMD. The best-fitting isochrone to the CMD yields an age of 1 Myr, a distance of 6.6–6.9 kpc, and $A_{\rm V}$=4.6-4.7 mag for the PMS and intermediate-mass MS cluster members. Furthermore, the richness of NYC and its underlying stellar population allowed me to identify stars at the location of the short-lived radiative convective gap, which occurs at 3.5–3.8 $M_\odot$ at the age of NYC. With accurate photometry of the proper motion selected cluster members, we find hints of a sparse young low-mass population with an age of ~ 4 Myr. These stars might constitute an earlier generation of star formation in NGC 3603 and likely represents the low-mass counterparts to several blue supergiants in the vicinity of NYC.

Multiple recent star forming events or even continuous star formation over the last 3 Myr are also identified in the young cluster Tr 14. Deep MCAO corrected H and K_S observations, obtained with the first VLT MCAO system MAD, offered the opportunity to derive accurate photometry over a $2' \times 2'$ FoV. Photometry was obtained of $\sim 1,700$ stars reaching $K \sim 18.85$ mag which corresponds to 0.1-0.2 $M_\odot$ on the PMS. The corresponding CMD and the subsequent comparison with stellar evolutionary

models displays a major star forming event that occured 1 Myr ago. However, hints for ongoing star formation as well as for an older population are found supporting a scenario of continuous star formation over the last 3 Myr would. This agrees with earlier studies detecting a slightly older halo population with respect the the core of the cluster (Ascenso et al., 2007b).

Key information for post-main sequence evolution could be derived from seeing limited observations of RSGC 1. Estimating the age to be 10 ± 1 Myr and the extinction to be $A_V = 20$ mag together with a derived distance of 6 kpc allowed me to identify the starting point of the BSG phase. This provides an estimate for the number of BSG in the cluster of 36 ± 5 and a subsequent assessment of the B-R ratio. This was measured to be $B/R = 2.6 \pm 0.4$, consistent with the B-R ratio–metalicity relation and relation of the B-R ratio to the distance from the Galactic center as shown in Eggenberger et al. (2002). For an accurate census of the BSG population, spectroscopic confirmation is required. Due to the extend of the cluster and the tenth of BSG candidates in RSGC 1, it offers an ideal science case for multi-object spectroscopy with, e.g., LBT-Lucifer.

Cluster dynamics: Besides providing a clean sample of cluster stars, the proper motions contain important kinematic information to reveal the dynamic state of NYC. The measured stellar motions enabled me to derive the first internal velocity dispersion of a Galactic starburst cluster. I determine a one-dimensional proper motion dispersion of $141 \pm 27 \mu$as yr^{-1} which corresponds to a velocity dispersion of 4.5 ± 0.8 km s^{-1} at a distance of 6.75 kpc. I could further show that the velocity dispersion does not vary with stellar mass for stars with masses $1.7\,\mathrm{M}_\odot < \mathrm{M} < 9\,\mathrm{M}_\odot$. I deduce that NYC has not yet reached equipartition of energy. This is not entirely unexpected at the young age of the cluster, since its crossing time is estimated to be 1.4 Myr by Nürnberger & Petr-Gotzens (2002). The same might be true for many extragalactic starburst clusters, where mass estimates rely on the measurements of velocity dispersions. If these clusters are also not yet in virial equilibrium, their masses might be systematically overestimated. Thus, NYC provides an important benchmark for our understanding of the early dynamical evolution and the long-term survival of young, massive stellar clusters in the Milky Way and in other galaxies.

The measured velocity dispersion offers not only important insights into the internal dynamics of NYC but also into the formation process and the further evolution of NYC. Comparison of dynamical mass and photometric mass indicates that the cluster is, after the expulsion of its intracluster gas, out of – but not far from – dynamical equilibrium. Furthermore, it hints at a high SFE suggesting a survival of the cluster after the early mass loss event. The dissolution of the cluster through the gradual loss of stars will last $t_dis = 3.4$ Gyr

Mass function: The depth of the photometry allowed me to derive the PDMFs of the central region of each cluster. In the two young cluster, NYC and Tr 14, the PDMF was obtained down to the subsolar regime, in case of Tr 14 even into the range of the very low-mass stars ($0.1 - 0.2 M_{\odot}$). In case of NYC and RSGC 1 it is well represented by a single power law, while in Tr 14 the PDMF turns over at $0.5 M_{\odot}$ consistent with the characteristic mass of a Kroupa-IMF. Variations of the power law slopes, when comparing the innermost region with regions further out, revealed NYC as a mass segregated cluster. Tr 14, in contrast, shows no varying PDMF in the considered mass regime, thus, no mass segregation is observed. In general, all clusters have rather shallow slopes when compared to a Salpeter- or Kroupa-IMF illustrating the lack of low mass stars in the very centers of these young and compact objects. Although low mass stars can be expelled from the central regions via two-body encounters with the other members of the cluster, the associated timescales are too large to produce such a deficiency as observed in the PDMFs. Therefore, it is more likely, that the lack of low mass stars reflects the state of the formation of the cluster. Consequently, the low fraction of low mass stars is more likely caused by the influence of the massive stellar content of the regions dispersing the surrounding material, such as intracluster gas via gas expulsion and circumstellar disks, and subsequently quenching low mass star formation.

Outlook: Accurate proper motion measurements provide a powerful tool to assess important properties of the cluster. With upcoming new telescopes such as the *James Webb Space Telescope (JWST)* or the Extremely Large Telescopes (ELTs) proper motion studies will be conducted with unprecedented accuracy. Not only offering a 2.5 times better angular resolution, comparing *JWST* to *HST*, but also the larger time baselines that are provided will allow to measure kinematic properties even in the very dense cores of stellar clusters.

The next generation ELTs will offer ground-based high resolution observations over a large FoV using MCAO instruments. The data that has been obtained with VLT-MAD allows me to assess the capabilities of an MCAO system. The analysis revealed an impressive performance of the AO system over the large FoV of $2' \times 2'$ FoV. The shallow degradation of the Strehl ratios over the FoV shows a significant improvement of the spatial stability of the AO performance, when compared to SCAO systems. It demonstrates the superior performance of MCAO systems for wide-field AO corrected observations. This was supported by quality of the PSF photometry that has been obtained from the data. The stability of the correction for atmospheric turbulence in combination the correction over a few arcminutes provides an ideal combination for investigations that depend on high angular resolution instruments as well as a large FoV. Therefore, VLT-MAD gives a very promissing impression of the future prospects

of observations with upcoming new telescopes and instruments.

Chapter 6

Akronyme

2MASS 2 **M**icron **A**ll **S**ky **S**urvey
ADONIS **AD**aptive **O**ptics **N**ear-**I**nfrared **S**ystem
AO **A**daptive **O**ptics
BSG **B**lue **S**uper**G**iant
CAHA **C**entro **A**stronomico **H**ispano **A**leman
CMD **C**olor **M**agnitude **D**iagram
CTE **C**harge **T**ransfer **E**fficiency
DIT **D**etector **I**ntegration **T**ime
DM **D**eformable **M**irrors
ELT **E**xtremely **L**arge **T**elescope
E-ELT **E**uropean-**E**xtremely **L**arge **T**elescope
FoV **F**ield **o**f **V**iew
FWHM **F**ull **W**idth at **H**alf **M**aximum
GS **G**uide **S**tar
HRD **H**ertzsprung **R**ussel **D**iagram
HMS **H**igh **M**ain **S**equence
HST **H**ubble **S**pace **T**elescope
IMF **I**nitial **M**ass **F**unction
LF **L**uminosity **F**unction
LMS **L**ow **M**ain **S**equence
MAD **M**ulti-**C**onjugated **A**daptive Optics **D**emonstator
MCAO **M**ulti-**C**onjugated **A**daptive **O**ptics
MF **M**ass **F**unction
MLR **M**ass **L**uminosity **R**elation
MOIRCS **M**ulti-**O**bject **I**nfra**R**ed **C**amera **S**pectrograph
MS **M**ain **S**equence

MW **M**ilky **W**ay
NDIT **N**umber of **D**etector **I**n**T**egrations
NGS **N**atural **G**uide **S**tars
NTT **N**ew **T**echnology **T**elescope
NYC **N**GC 3603 **Y**oung **C**luster
PDMF **P**resent **D**ay **M**ass **F**unction
PMS **P**re **M**ain **S**equence
PSF **P**oint **S**pread **F**unction
RSG **R**ed **S**uper**G**iant
RSGC 1 **R**ed **S**uper**G**iant **C**luster **1**
SCAO **S**ingle-**C**onjugated **A**daptive **O**ptics
SofI **S**on **of** **I**saac
SFE **S**tar **F**ormation **E**fficiency
Tr 14 **Tr**umpler **14**
Tr 16 **Tr**umpler **16**
UKIDSS **UK**IRT **I**nfrared **D**eep **S**ky **S**urvey
VLT **V**ery **L**arge **T**elescope
WFS **W**ave**F**ront **S**ensors
WFPC2 **W**ide **F**ield **P**lanetary **C**amera 2
ZP **Z**ero **P**oint
ZAMS **Z**ero **A**ge **M**ain **S**equence

Bibliography

Adams, F. C. 2000, ApJ, 542, 964

Alexander, M. J., Kobulnicky, H. A., Clemens, D. P., et al. 2009, AJ, 137, 4824

Allard, F. & Freytag, B. 2010, Highlights of Astronomy, 15, 756

Amorim, A., Lima, J., Alves, J., et al. 2006, in Presented at the Society of Photo-Optical Instrumentation Engineers (SPIE) Conference, Vol. 6269, Society of Photo-Optical Instrumentation Engineers (SPIE) Conference Series

Anderson, J. & King, I. R. 1999, PASP, 111, 1095

Anderson, J. & King, I. R. 2000, PASP, 112, 1360

Anderson, J. & King, I. R. 2003a, AJ, 126, 772

Anderson, J. & King, I. R. 2003b, PASP, 115, 113

Ascenso, J., Alves, J., Beletsky, Y., & Lago, M. T. V. T. 2007a, A&A, 466, 137

Ascenso, J., Alves, J., Vicente, S., & Lago, M. T. V. T. 2007b, A&A, 476, 199

Athanassoula, E. 1992, MNRAS, 259, 328

Babcock, H. W. 1953, PASP, 65, 229

Bastian, N., Covey, K. R., & Meyer, M. R. 2010, ARA&A, 48, 339

Bastian, N., Gieles, M., Efremov, Y. N., & Lamers, H. J. G. L. M. 2005, A&A, 443, 79

Baumgardt, H. & Kroupa, P. 2007, MNRAS, 380, 1589

Baumgardt, H. & Makino, J. 2003, MNRAS, 340, 227

Bertin, E. & Arnouts, S. 1996, A&AS, 117, 393

Beuzit, J., Hubin, N., Gendron, E., et al. 1994, in Presented at the Society of Photo-Optical Instrumentation Engineers (SPIE) Conference, Vol. 2201, Society of Photo-Optical Instrumentation Engineers (SPIE) Conference Series, ed. M. A. Ealey & F. Merkle, 955–961

Bica, E., Dutra, C. M., Soares, J., & Barbuy, B. 2003, A&A, 404, 223

Binney, J. & Merrifield, M. 1998, Galactic astronomy (Galactic astronomy / James Binney and Michael Merrifield. Princeton, NJ : Princeton University Press, 1998. (Princeton series in astrophysics) QB857 .B522 1998 ($35.00))

Bonnell, I. A. & Bate, M. R. 2006, MNRAS, 370, 488

Brandl, B., Brandner, W., Eisenhauer, F., et al. 1999, A&A, 352, L69

Brandner, W., Clark, J. S., Stolte, A., et al. 2008, A&A, 478, 137

Cardelli, J. A., Clayton, G. C., & Mathis, J. S. 1989, ApJ, 345, 245

Carraro, G., Romaniello, M., Ventura, P., & Patat, F. 2004, A&A, 418, 525

Cassisi, S. & Salaris, M. 1997, MNRAS, 285, 593

Castelli, F. & Kurucz, R. L. 2003, in IAU Symposium, Vol. 210, Modelling of Stellar Atmospheres, ed. N. Piskunov, W. W. Weiss, & D. F. Gray, 20P p.

Clark, J. S., Negueruela, I., Davies, B., et al. 2009, A&A, 498, 109

Cox, C. & Gilliland, R. L. 2002, in The 2002 HST Calibration Workshop : Hubble after the Installation of the ACS and the NICMOS Cooling System, ed. S. Arribas, A. Koekemoer, & B. Whitmore, 58–+

Cresci, G., Davies, R. I., Baker, A. J., & Lehnert, M. D. 2005, A&A, 438, 757

Da Rio, N., Gouliermis, D. A., & Henning, T. 2009, ApJ, 696, 528

Da Rio, N., Robberto, M., Soderblom, D. R., et al. 2010, ApJ, 722, 1092

Davies, B., Figer, D. F., Kudritzki, R., et al. 2007, ApJ, 671, 781

de Grijs, R., Anders, P., Bastian, N., et al. 2003, MNRAS, 343, 1285

de Grijs, R., Gilmore, G. F., Johnson, R. A., & Mackey, A. D. 2002, MNRAS, 331, 245

Degl'Innocenti, S., Prada Moroni, P. G., Marconi, M., & Ruoppo, A. 2008, Ap&SS, 316, 25

Demailly, L., Gendron, E., Beuzit, J., Lacombe, F., & Hubin, N. 1994, in Presented at the Society of Photo-Optical Instrumentation Engineers (SPIE) Conference, Vol. 2201, Society of Photo-Optical Instrumentation Engineers (SPIE) Conference Series, ed. M. A. Ealey & F. Merkle, 867–878

Devillard, N. 2001, in Astronomical Society of the Pacific Conference Series, Vol. 238, Astronomical Data Analysis Software and Systems X, ed. F. R. Harnden Jr., F. A. Primini, & H. E. Payne, 525 p.

Dias, W. S., Alessi, B. S., Moitinho, A., & Lépine, J. R. D. 2002, A&A, 389, 871

Dolphin, A. E. 2000, PASP, 112, 1397

Eggenberger, P., Meynet, G., & Maeder, A. 2002, A&A, 386, 576

Elson, R. A. W., Fall, S. M., & Freeman, K. C. 1987, ApJ, 323, 54

Figer, D. F., Kim, S. S., Morris, M., et al. 1999, ApJ, 525, 750

Figer, D. F., MacKenty, J. W., Robberto, M., et al. 2006, ApJ, 643, 1166

Gennaro, M., Brandner, W., Stolte, A., & Henning, T. 2011, MNRAS, 162

Geyer, M. P. & Burkert, A. 2001, MNRAS, 323, 988

Giersz, M. & Heggie, D. C. 1994, MNRAS, 268, 257

Girard, T. M., Grundy, W. M., Lopez, C. E., & van Altena, W. F. 1989, AJ, 98, 227

Harayama, Y., Eisenhauer, F., & Martins, F. 2008, ApJ, 675, 1319

Hillenbrand, L. A. 1997, AJ, 113, 1733

Hills, J. G. 1980, ApJ, 235, 986

Holtzman, J. A., Hester, J. J., Casertano, S., et al. 1995, PASP, 107, 156

Iben, Jr., I. 1965, ApJ, 141, 993 p.

Jones, B. F. & Walker, M. F. 1988, AJ, 95, 1755

Kennicutt, Jr., R. C. 1984, ApJ, 287, 116

King, I. R. & Anderson, J. 2001, in Astronomical Society of the Pacific Conference Series, Vol. 228, Dynamics of Star Clusters and the Milky Way, ed. S. Deiters, B. Fuchs, A. Just, R. Spurzem, & R. Wielen, 19 p.

King, I. R. & Anderson, J. 2002, in Astronomical Society of the Pacific Conference Series, Vol. 273, The Dynamics, Structure & History of Galaxies: A Workshop in Honour of Professor Ken Freeman, ed. G. S. Da Costa & H. Jerjen, 167 p.

King, I. R., Bedin, L. R., Piotto, G., Cassisi, S., & Anderson, J. 2005, AJ, 130, 626

Koekemoer, A. M., Fruchter, A. S., Hook, R. N., & Hack, W. 2002, in The 2002 HST Calibration Workshop : Hubble after the Installation of the ACS and the NICMOS Cooling System, ed. S. Arribas, A. Koekemoer, & B. Whitmore, 337 p.

Kozhurina-Platais, V., Goudfrooij, & Puzia, T. H. 2007, ACS/WFC: Differential CTE Corrections for Photometry and Astronomy from Non-Drizzled Images, Tech. rep., STSCI

Krist, J. 1995, in Astronomical Society of the Pacific Conference Series, Vol. 77, Astronomical Data Analysis Software and Systems IV, ed. R. A. Shaw, H. E. Payne, & J. J. E. Hayes, 349 p.

Kroupa, P. 2001, MNRAS, 322, 231

Kroupa, P. 2002, Science, 295, 82

Krumholz, M. R., McKee, C. F., & Klein, R. I. 2005, Nature, 438, 332

Lada, C. J. & Lada, E. A. 2003, ARA&A, 41, 57

Lada, C. J., Margulis, M., & Dearborn, D. 1984, ApJ, 285, 141

Lamers, H. J. G. L. M., Anders, P., & de Grijs, R. 2006, A&A, 452, 131

Larsen, S. S. 2009, A&A, 503, 467

Maíz Apellániz, J. & Úbeda, L. 2005, ApJ, 629, 873

Marchetti, E., Brast, R., Delabre, B., et al. 2007, The Messenger, 129, 8

Marchetti, E., Brast, R., Delabre, B., et al. 2004, in Presented at the Society of Photo-Optical Instrumentation Engineers (SPIE) Conference, Vol. 5490, Society of Photo-Optical Instrumentation Engineers (SPIE) Conference Series, ed. D. Bonaccini Calia, B. L. Ellerbroek, & R. Ragazzoni, 236–247

Marchetti, E., Ragazzoni, R., & Diolaiti, E. 2003, in Presented at the Society of Photo-Optical Instrumentation Engineers (SPIE) Conference, Vol. 4839, Society of Photo-Optical Instrumentation Engineers (SPIE) Conference Series, ed. P. L. Wizinowich & D. Bonaccini, 566–577

Marigo, P., Girardi, L., Bressan, A., et al. 2008, A&A, 482, 883

Massey, P. & Johnson, J. 1993, AJ, 105, 980

Mayne, N. J., Naylor, T., Littlefair, S. P., Saunders, E. S., & Jeffries, R. D. 2007, MNRAS, 375, 1220

McCrady, N. & Graham, J. R. 2007, ApJ, 663, 844

Melena, N. W., Massey, P., Morrell, N. I., & Zangari, A. M. 2008, AJ, 135, 878

Mengel, S., Lehnert, M. D., Thatte, N. A., et al. 2008, A&A, 489, 1091

Mengel, S. & Tacconi-Garman, L. E. 2007, A&A, 466, 151

Merkle, F., Gehring, G., Rigaut, F., et al. 1990, The Messenger, 60, 9

Merkle, F., Kern, P., Léna, P., et al. 1989, The Messenger, 58, 1

Messineo, M., Davies, B., Ivanov, V. D., et al. 2009, ApJ, 697, 701

Meynet, G., Georgy, C., Hirschi, R., et al. 2011, Bulletin de la Societe Royale des Sciences de Liege, 80, 266

Meynet, G., Maeder, A., Schaller, G., Schaerer, D., & Charbonnel, C. 1994, A&AS, 103, 97

Moffat, A. F. J., Poitras, V., Marchenko, S. V., et al. 2004, AJ, 128, 2854

Navarrete, J. 2011, ArXiv e-prints

Negueruela, I., Gonzalez-Fernandez, C., Marco, A., & Clark, J. S. 2011, ArXiv e-prints

Nelan, E. P., Walborn, N. R., Wallace, D. J., et al. 2004, AJ, 128, 323

Nürnberger, D. E. A. & Petr-Gotzens, M. G. 2002, A&A, 382, 537

Portegies Zwart, S. F., McMillan, S. L. W., & Gieles, M. 2010, ARA&A, 48, 431

Rathborne, J. M., Burton, M. G., Brooks, K. J., et al. 2002, MNRAS, 331, 85

Robin, A. C., Reylé, C., Derrière, S., & Picaud, S. 2003, A&A, 409, 523

Rochau, B., Brandner, W., Stolte, A., et al. 2010, ApJ, 716, L90

Rochau, B., Gouliermis, D. A., Brandner, W., Dolphin, A. E., & Henning, T. 2007, ApJ, 664, 322

Sagar, R. & Richtler, T. 1991, A&A, 250, 324

Salaris, M. & Cassisi, S. 2005, Evolution of Stars and Stellar Populations (Evolution of Stars and Stellar Populations, by Maurizio Salaris, Santi Cassisi, pp. 400. ISBN 0-470-09220-3. Wiley-VCH , December 2005.)

Salpeter, E. E. 1955, ApJ, 121, 161

Sana, H., Momany, Y., Gieles, M., et al. 2010, A&A, 515, A26+

Sandstrom, K., Krause, O., Linz, H., et al. 2010, A&A, 518, L59+

Scalo, J. M. 1986, Fundamentals of Cosmic Physics, 11, 1

Schaller, G., Schaerer, D., Meynet, G., & Maeder, A. 1992, A&AS, 96, 269

Schlegel, D. J., Finkbeiner, D. P., & Davis, M. 1998, ApJ, 500, 525

Shaklan, S., Sharman, M. C., & Pravdo, S. H. 1995, Applied Optics, 34, 6672

Siess, L., Dufour, E., & Forestini, M. 2000, A&A, 358, 593

Siess, L., Forestini, M., & Bertout, C. 1997, A&A, 326, 1001

Smith, N. 2006, MNRAS, 367, 763

Spitzer, L. 1987, Dynamical evolution of globular clusters (Princeton, NJ, Princeton University Press, 1987, 191 p.)

Stahler, S. W. 1983, ApJ, 274, 822

Stahler, S. W. & Palla, F. 2005, The Formation of Stars (The Formation of Stars, by Steven W. Stahler, Francesco Palla, pp. 865. ISBN 3-527-40559-3. Wiley-VCH , January 2005.)

Stetson, P. B. 1990, PASP, 102, 932

Stolte, A. 2003, PhD thesis, PhD Thesis, Combined Faculties for the Natural Sciences and for Mathematics of the Ruperto-Carola University of Heidelberg, Germany for the degree of Doctor of Natural Sciences. III + 156 pp. (2003)

Stolte, A., Brandner, W., Brandl, B., & Zinnecker, H. 2006, AJ, 132, 253

Stolte, A., Brandner, W., Brandl, B., Zinnecker, H., & Grebel, E. K. 2004, AJ, 128, 765

Stolte, A., Brandner, W., Grebel, E. K., Lenzen, R., & Lagrange, A. 2005, ApJ, 628, L113

Strehl, K. 1895, Zeitschrift fi¿$\frac{1}{2}$r Instrumentenkunde, 15, 362

Sung, H. & Bessell, M. S. 2004, AJ, 127, 1014

Tapia, M., Roth, M., Vázquez, R. A., & Feinstein, A. 2003, MNRAS, 339, 44

Vazquez, R. A., Baume, G., Feinstein, A., & Prado, P. 1996, A&AS, 116, 75

Vesperini, E. & Heggie, D. C. 1997, MNRAS, 289, 898

Whitmore, B., Heyer, I., & Casertano, S. 1999, PASP, 111, 1559

Whitmore, B. C. & Schweizer, F. 1995, AJ, 109, 960

Zhang, Q. & Fall, S. M. 1999, ApJ, 527, L81

Zinnecker, H. & McCaughrean, M. 1991, MmSAI, 62, 761

Zinnecker, H. & Yorke, H. W. 2007, ARA&A, 45, 481

Acknowledgements

First I would like to thank Prof. Dr. Thomas Henning for allowing me to conduct this thesis and for the support and supervision during the past years.
My deep thanks are going to Dr. Wolfgang Brandner for his great support, his supervision and the patience during the development of this work.
Further deep thanks to Dr. Andrea Stolte for many useful discussions, suggestions, corrections and all the conversations aside the work.
I would like to thank Prof. Dr. Ralf Klessen for evaluating this thesis and for being part of the defense committee.
Thanks to apl. Prof. Dr. Mario Trieloff and Priv. Doz. Dr. Andreas Just for spending their time to complete the defense committee.
Thanks also to the rest of the MPIA cluster crew: Arjan, Dimitris, Mario, Natalia and Nicola. Always a pleasure meeting and discussing with you.
I further would like to thank the people of the MPIA for creating such an enjoyable atmosphere making the past years to a time full of nice memories.
A special thanks to the sky lounge coffee group.
Thanks to the Poker round for 'stealing' my money...
Many thanks to the Squash players who led me win from time to time and 'thanks' to the others for beating me up.
Further thanks to the PhD students community for a great time during and after work.
A special deep Thank you to Helen, Bubu, Carina, Arne, Kathrin, Christian, Kitty for being such great friends.
Thanks to Frithjof for being an exceptional person. Missing you.
Thanks to Arne, Kolja, Hannes and Sascha for being patient friends during my 'part-time' absence.
Many, many thanks to everyone that I accidently forgot to thank explicitly.
My final and deepest thanks are going to my family for the permanent support they are offering no matter what time or issue. Thank you so much.